8-2010

Nonlinear Control and Estimation Techniques with Applications to Vision-based and Biomedical Systems

Nitendra Nath
Clemson University, nnath@clemson.edu

NONLINEAR CONTROL AND ESTIMATION TECHNIQUES WITH APPLICATIONS TO VISION-BASED AND BIOMEDICAL SYSTEMS

A Dissertation
Presented to
the Graduate School of
Clemson University

In Partial Fulfillment
of the Requirements for the Degree
Doctor of Philosophy
Electrical and Computer Engineering

---

by
Nitendra Nath
August 2010

Accepted by:
Dr. Darren M. Dawson, Committee Chair
Dr. Timothy C. Burg
Dr. Ian D. Walker
Dr. John R. Wagner
Dr. Enver Tatlicioglu

ABSTRACT

This dissertation is divided into four self-contained chapters. In Chapter 1, a new estimator using a single calibrated camera mounted on a moving platform is developed to asymptotically recover the range and the three-dimensional (3D) Euclidean position of a static object feature. The estimator also recovers the constant 3D Euclidean coordinates of the feature relative to the world frame as a byproduct. The position and orientation of the camera is assumed to be measurable unlike existing observers where velocity measurements are assumed to be known. To estimate the unknown range variable, an adaptive least squares estimation strategy is employed based on a novel prediction error formulation. A Lyapunov stability analysis is used to prove the convergence properties of the estimator. The developed estimator has a simple mathematical structure and can be used to identify range and 3D Euclidean coordinates of multiple features. These properties of the estimator make it suitable for use with robot navigation algorithms where position measurements are readily available. Numerical simulation results along with experimental results are presented to illustrate the effectiveness of the proposed algorithm.

In Chapter 2, a novel Euclidean position estimation technique using a single uncalibrated camera mounted on a moving platform is developed to asymptotically recover the three-dimensional (3D) Euclidean position of static object features. The position of the moving platform is assumed to be measurable, and a second object with known 3D Euclidean coordinates relative to the world frame is considered to be available *a priori*. To account for the unknown camera calibration parameters and to estimate the unknown 3D Euclidean coordinates, an adaptive least squares estimation strategy is employed based on prediction error formulations and a Lyapunov-type stability analysis. The developed estimator is shown to recover the 3D Euclidean position of the unknown object features despite the lack of knowledge of the camera calibration parameters. Numerical simulation results along with experimental results are

presented to illustrate the effectiveness of the proposed algorithm.

In Chapter 3, a new range identification technique for a calibrated paracatadioptric system mounted on a moving platform is developed to recover the range information and the three-dimensional (3D) Euclidean coordinates of a static object feature. The position of the moving platform is assumed to be measurable. To identify the unknown range, first, a function of the projected pixel coordinates is related to the unknown 3D Euclidean coordinates of an object feature. This function is nonlinearly parameterized (*i.e.*, the unknown parameters appear nonlinearly in the parameterized model). An adaptive estimator based on a min-max algorithm is then designed to estimate the unknown 3D Euclidean coordinates of an object feature relative to a fixed reference frame which facilitates the identification of range. A Lyapunov-type stability analysis is used to show that the developed estimator provides an estimation of the unknown parameters within a desired precision. Numerical simulation results are presented to illustrate the effectiveness of the proposed range estimation technique.

In Chapter 4, optimization of antiangiogenic therapy for tumor management is considered as a nonlinear control problem. A new technique is developed to optimize antiangiogenic therapy which minimizes the volume of a tumor and prevents it from growing using an optimum drug dose. To this end, an optimum desired trajectory is designed to minimize a performance index. Two controllers are then presented that drive the tumor volume to its optimum value. The first controller is proven to yield exponential results given exact model knowledge. The second controller is developed under the assumption of parameteric uncertainties in the system model. A least-squares estimation strategy based on a prediction error formulation and a Lyapunov-type stability analysis is developed to estimate the unknown parameters of the performance index. An adaptive controller is then designed to track the desired optimum trajectory. The proposed tumor minimization scheme is shown to minimize the tumor volume with an optimum drug dose despite the lack of knowledge of system parameters. Numerical simulation results are presented to illustrate the

effectiveness of the proposed technique. An extension of the developed technique for a mathematical model which accounts for pharmacodynamics and pharmacokinetics is also presented. Futhermore, a technique for the estimation of the carrying capacity of endothelial cells is also presented.

DEDICATION

This work is dedicated to my parents whose love and encouragement has made it possible.

ACKNOWLEDGMENTS

I would like to take this opportunity to thank all those who helped me in my pursuit of a Doctorate of Philosophy degree. I express deep gratitude to my advisor, Dr. Darren M. Dawson for his support, guidance and for motivating me to strive for higher levels of excellence in my work. I would also like to thank my committee members, Dr. Timothy C. Burg, Dr. Enver Tatlicioglu, Dr. Ian D. Walker, and Dr. John R. Wagner for all their technical guidance.

I would also like to thank my colleagues and friends, Apoorva Kapadia and Erhun Iyasere for their support and encouragement during the course of my work. Special thanks go to the people at the Controls and Robotics group, especially Dr. Enver Tatlicioglu for his invaluable help and assistance. His support in time of need was greatly appreciated. Dr. David Braganza deserves special credit for guiding me when I was starting my doctoral work. His patience and exemplary working habits have motivated me throughout my research work at Clemson.

Thanks also go to my friends Gauri Phadke, Judhajit Roy, Shyam Panyam, Parth Bhavsar, and all my friends at Clemson whose support helped me concentrate on my work. Finally, this acknowledgment would be incomplete without thanking my parents, my sister, and my brother-in-law whose motivation and support at all times, has made me what I am.

TABLE OF CONTENTS

Table of Contents (Continued)

Page

LIST OF FIGURES

List of Figures (Continued)

Figure Page

List of Figures (Continued)

Figure Page

CHAPTER 1
RANGE IDENTIFICATION FOR PERSPECTIVE VISION SYSTEMS: A POSITION BASED APPROACH

Introduction

Range identification, where the time-varying distance from the camera to the object along the focal length is recovered, has been a mainstream research problem for many years. The range and thus, the three-dimensional (3D) Euclidean coordinates of a feature on a moving or a static object can be recovered from its two-dimensional (2D) projection on the image-plane of the camera. The estimation of the unmeasurable range signal is usually done by mounting a camera on a moving vehicle such as an unmanned aerial vehicle (UAV) or a mobile robot that travels through the environment and takes images of static objects or features. Range identification has significant impact on several applications including autonomous vehicle navigation, aerial tracking, path planning, surveillance of ground based, stationary or moving objects [3, 4, 5, 6] and terrain mapping systems [7, 8, 9].

Although, the problem of range identification is inherently nonlinear, linearization based techniques, typically extended Kalman filter (EKF), have been frequently used [10, 11, 12, 13, 14]. The use of linearized motion models can cause significant inconsistencies in solutions [15]. Also, it is well known that the EKF may fail in some real applications [1] and the convergence conditions for the continuous time EKF can only be checked by actually running the filter [16]. Another drawback of EKF is an *a priori* assumption of the noise model [1]. To overcome these shortcomings, an identifier based nonlinear observer was proposed in [17], and was followed by several researchers who focused on utilizing nonlinear system analysis and estimation tools to develop nonlinear state observers for the problem [1, 18, 19, 20, 21, 22, 23, 2]. All of these observers were based on known motion dynamics and known motion parameters of the object (or the camera). The known motion dynamics can model either a static

point's 3D position as seen from a moving camera (assuming camera's velocities to be measurable [17]) or a moving point's 3D position as seen from a stationary camera [24]. In practice, it is easier to measure the velocity of the moving camera than to have knowledge of the motion parameters of a moving object. In [25], Gupta *et al.* developed a nonlinear state estimator that can be applied to the nonaffine perspective dynamic system assuming known motion parameters. More recently, in [26], Dahl *et al.* designed a nonlinear observer to estimate 3D position assuming knowledge of linear and angular velocities. In [27], again the velocity of the moving camera was assumed to be known and a nonlinear integral observer was utilized to estimate the velocity of each feature point in the image plane which facilitated the design of an estimator for the unknown range parameter. Furthermore, in [2], De Luca *et al.* employed nonlinear observer theory to develop a depth-estimator utilizing velocity measurements of the camera.

All the aforementioned papers detailing nonlinear state observers for range identification are based on known motion parameters, that is, they utilize velocity measurements. However, only [2] reports experimental results where it can be seen that the estimated depth signals are quite noisy because a numerical differentiation step is utilized to obtain actual robot velocities. The numerical differentiation results in noisy velocity measurements. Further in [28], a low-pass filter was utilized to smooth the measured velocity signals; still, satisfactory results for Euclidean distance estimation errors were not obtained. Recently, we have made several attempts to implement the estimator in [27], using an industrial charge-coupled device (CCD) camera on a robotic manipulator. However, we failed to obtain an estimation of the range variable because of very noisy velocity measurements. For many applications, position measurements are considerably less noisy and easy to obtain than velocity measurements; hence, we are motivated to develop a new estimator where measured position of a moving mechanical system can be directly utilized to identify the range of a static object feature. To the best of our knowledge, the current work presents the first

results in range identification where robot position measurements are utilized instead of velocity measurements.

In this paper, our goal is to develop an estimator to identify the range of a feature on a static object by mounting a calibrated camera on a mobile platform whose position is measurable. There are applications such as video surveillance and mapping using a UAV or a mobile robot where the position of the camera is readily measurable assuming that the intrinsic and extrinsic camera parameters are known. The estimator is designed by first developing a geometric model to relate the fixed feature point on the object with the moving camera. The novelty of this work lies in the parameterization of a nonlinear model which relates the projected pixel coordinates with the Euclidean coordinates of the object feature. A prediction error formulation is then presented which allows us to utilize nonlinear estimation theory to design an adaptive least squares estimator. We show that the developed estimator asymptotically identifies the range along with the Euclidean coordinates of the feature on the object subject to a persistency of excitation condition similar to that of [2]. An important byproduct of the proposed estimation technique is the estimation of the constant 3D Euclidean coordinates of the feature on an object relative to the world frame. The estimation technique that is presented has shown good robustness to noise, quick convergence, and provides accurate results which is demonstrated by simulation and experimental results.

Geometric Model

To develop a geometrical relationship between a moving camera and a stationary object, an orthogonal coordinate frame, denoted by $\mathcal{C}$, whose origin coincides with the optical center of the moving camera, an inertial coordinate frame, denoted by $\mathcal{W}$, and an orthogonal coordinate frame, denoted by $\mathcal{B}$, are used (see Fig. 1.1). To make the following discussion more tractable, a feature point located on the static object, denoted by $\mathcal{F}$, is considered. Let the 3D coordinates of the feature on the object

be denoted as the constant $x_f \in \mathbb{R}^3$ relative to the world frame $\mathcal{W}$ and $\bar{m}(t) \in \mathbb{R}^3$ relative to the camera frame $\mathcal{C}$ which is defined as follows

$$\bar{m} \triangleq [x \quad y \quad z]^T. \tag{1.1}$$

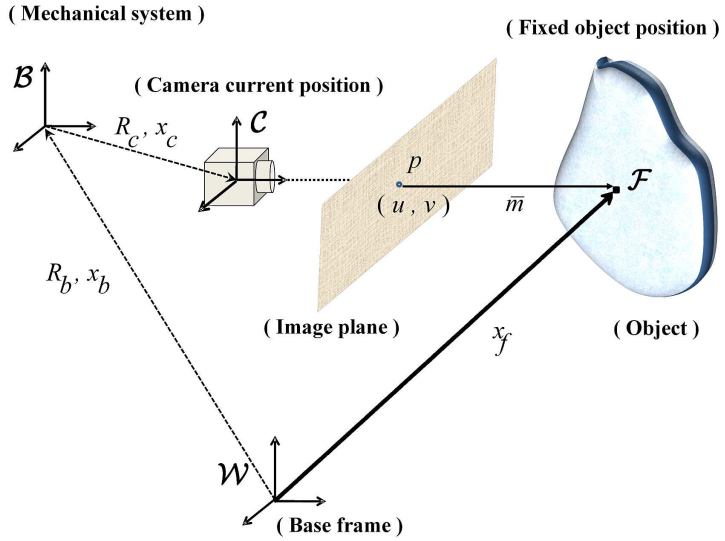

Figure 1.1 Geometric relationships between the fixed object, mechanical system, and the camera.

In the subsequent development, it is assumed that the feature point is always in the field of view of the camera; hence, the distance from the origin of $\mathcal{C}$ to the feature is always positive and bounded. To relate the coordinate systems, let $R_b(t) \in SO(3)$ and $x_b(t) \in \mathbb{R}^3$ denote the rotation matrix and the translation vector, respectively, from $\mathcal{B}$ to $\mathcal{W}$, expressed in $\mathcal{W}$. Let $R_c \in SO(3)$ and $x_c \in \mathbb{R}^3$ denote the rotation matrix and the translation vector, respectively, from $\mathcal{C}$ to $\mathcal{B}$, expressed in $\mathcal{B}$. Let $m(t) \in \mathbb{R}^3$ denote the normalized Euclidean coordinates for the feature point relative to $\mathcal{C}$, which is defined as follows

$$m \triangleq \frac{1}{z}\bar{m} = [x/z \quad y/z \quad 1]^T. \tag{1.2}$$

In the image captured by the camera the feature point has corresponding projected pixel coordinates, denoted by $p(t) \in \mathbb{R}^2$, defined as follows

$$p \triangleq \begin{bmatrix} u & v \end{bmatrix}^T \tag{1.3}$$

in which $u(t),\ v(t) \in \mathbb{R}$. The projected pixel coordinates of the feature point is related to the normalized Euclidean coordinates by the pin-hole model [29] such that

$$p = Am \tag{1.4}$$

where $A \in \mathbb{R}^{2\times 3}$ is a known constant intrinsic camera calibration matrix defined as follows [30]

$$A \triangleq \begin{bmatrix} fk_u & fk_u \cot\phi & u_0 \\ 0 & \frac{fk_v}{\sin\phi} & v_0 \end{bmatrix} \tag{1.5}$$

where $k_u,\ k_v \in \mathbb{R}$ denote camera scaling factors, $u_0,\ v_0 \in \mathbb{R}$ represent the pixel coordinates of the principal point, $\phi \in \mathbb{R}$ is the angle between the camera axes, and $f \in \mathbb{R}$ is the camera focal length. From (1.2) and (1.4), $p(t)$ can be written as follows

$$p = \frac{1}{z} A\bar{m}. \tag{1.6}$$

The Euclidean coordinates of the feature point $\bar{m}(t)$ relative to the camera, including the corresponding range $z(t)$, are unknown and unmeasurable signals. The corresponding projected pixel coordinates $p(t)$ along with $R_b(t)$ and $x_b(t)$ are measurable signals, and R_c and x_c are known constant parameters. The objective of this work is to accurately identify the unknown constant Euclidean coordinates of the feature x_f relative to the world frame in order to recover the range $z(t)$ along with the 3D Euclidean coordinates $\bar{m}(t)$ of the feature on the object relative to the camera frame.

Range Estimation

In this section, a prediction error formulation for the unknown parameters will be used to parameterize $A\bar{m}$, and the unknown range variable $z(t)$. An estimator for the unknown 3D Euclidean coordinates x_f is then presented which facilitates the identification of the range variable. A stability analysis will be provided which ensures the estimation error signals go to zero.

Prediction Error Formulation

From the geometric model shown in Fig. 1.1, $\bar{m}(t)$ can be found to be of the following form

$$\bar{m} = R_c^T \left[R_b^T \left(x_f - x_b \right) - x_c \right]. \tag{1.7}$$

After utilizing (1.6) and (1.7), the pixel coordinates for the object feature can be written as follows

$$p = \frac{1}{z} A R_c^T \left[R_b^T (x_f - x_b) - x_c \right]. \tag{1.8}$$

The corresponding range $z\left(t\right)$ can be written from the last row of (1.7) as follows

$$z = R_{c3}^T \left[R_b^T (x_f - x_b) - x_c \right] \tag{1.9}$$

where $R_{c3}^T \in \mathbb{R}^{1\times 3}$ is the last row of R_c^T. It should be noted that, in (1.8) and (1.9), A, R_c, x_c are known constant parameters, $R_b\left(t\right)$, $x_b\left(t\right)$ are measurable signals, and x_f is an unknown constant parameter. Based on these facts, $p\left(t\right)$ can be parameterized as follows

$$p = \frac{1}{\Pi\theta} W\theta \tag{1.10}$$

where

$$\Pi\theta = z = R_{c3}^T \left[R_b^T (x_f - x_b) - x_c \right] \tag{1.11}$$

$$W\theta = A R_c^T \left[R_b^T (x_f - x_b) - x_c \right]. \tag{1.12}$$

We note that $z\left(t\right)$ is assumed to satisfy the following inequalities

$$\rho\left(\cdot\right) \geq z(t) = \Pi\theta \geq \varepsilon \tag{1.13}$$

where $\rho(\cdot) \in \mathbb{R}$ is a known positive function and $\varepsilon \in \mathbb{R}$ is a known positive constant. In (1.11) and (1.12), $\Pi(t) \in \mathbb{R}^{1\times 4}$ and $W(t) \in \mathbb{R}^{2\times 4}$ are measurable regression matrices, and $\theta \in \mathbb{R}^4$ is a partially unknown constant parameter vector which is defined as

$$\theta \triangleq \begin{bmatrix} x_{f1} & x_{f2} & x_{f3} & 1 \end{bmatrix}^T \tag{1.14}$$

where $x_{fi} \in \mathbb{R} \; \forall \; i = 1, 2, 3$ is the unknown Euclidean coordinate of the object feature relative to the world frame. It should be noted that in (1.11) and (1.12), x_f is the only unknown; we can use an estimate of this signal, $\hat{x}_f(t) \in \mathbb{R}^3$ in (1.7) to obtain an estimation of $\bar{m}(t)$ as follows

$$\hat{\bar{m}} = R_c^T \left[R_b^T \left(\hat{x}_f - x_b \right) - x_c \right] \tag{1.15}$$

and the corresponding range estimate from (1.11), as follows

$$\hat{z} = R_{c3}^T \left[R_b^T (\hat{x}_f - x_b) - x_c \right] \tag{1.16}$$

where $\hat{\bar{m}}(t) \in \mathbb{R}^3$ and $\hat{z}(t) \in \mathbb{R}$ are the estimates of $\bar{m}(t)$ and $z(t)$, respectively. To facilitate the prediction error development, both sides of (1.10) are multiplied with the term $\Pi\theta$ which results in the following expression

$$p\Pi\theta = W\theta. \tag{1.17}$$

The estimate of (1.17) can be defined as follows

$$\hat{p}\Pi\hat{\theta} = W\hat{\theta} \tag{1.18}$$

where $\hat{\theta}(t) \in \mathbb{R}^4$ is the estimate for θ. After subtracting (1.18) from (1.17), the following expression is obtained

$$p\Pi\theta - \hat{p}\Pi\hat{\theta} = W\theta - W\hat{\theta}. \tag{1.19}$$

After adding and subtracting the term $\hat{p}\Pi\theta$ to the left-hand-side of (1.19) and simplifying, the following expression can be obtained

$$\tilde{p} = \frac{1}{\Pi\theta}(W - \hat{p}\Pi)\tilde{\theta} \tag{1.20}$$

where $\tilde{\theta}(t) \in \mathbb{R}^4$ is the estimation error defined as follows

$$\tilde{\theta} \triangleq \theta - \hat{\theta} \tag{1.21}$$

and the prediction error for the object feature, $\tilde{p}(t) \in \mathbb{R}^2$, is defined as follows

$$\tilde{p} \triangleq \ p - \hat{p}. \tag{1.22}$$

The prediction error $\tilde{p}(t)$, given in (1.20), can be rewritten in a compact form as follows

$$\tilde{p} = B\bar{W}_p\tilde{\theta} \tag{1.23}$$

where $\bar{W}_p \in \mathbb{R}^{2\times 4}$ is a measurable signal and $B(t) \in \mathbb{R}$ is an auxiliary signal defined as follows

$$\bar{W}_p \triangleq W - \hat{p}\Pi\,, \qquad\qquad B \triangleq 1/(\Pi\theta). \tag{1.24}$$

Estimator

As mentioned earlier, an estimate of the 3D Euclidean coordinates $\hat{\bar{m}}(t)$ along with an estimate of the corresponding range $\hat{z}(t)$ can be obtained from (1.15) and (1.16), respectively, given the estimate of x_f. Thus, based on the subsequent stability analysis, the following adaptive update law $\dot{\hat{\theta}}\ (t) \in \mathbb{R}^4$ is designed to estimate x_f which facilitates the range identification

$$\dot{\hat{\theta}} \triangleq \text{Proj}\left\{\alpha\Gamma\bar{W}_p^T\tilde{p}\right\} \tag{1.25}$$

where $\text{Proj}\{\cdot\}$ ensures that the term $\Pi(t)\,\hat{\theta}(t)$ is positive (see Appendix B) and $\alpha(t) \in \mathbb{R}$ is a positive scalar function defined as follows

$$\alpha \triangleq 1 + \frac{1}{\varepsilon}\rho(\cdot) \tag{1.26}$$

In (1.25), $\Gamma(t) \in \mathbb{R}^{4\times 4}$ is the least-squares estimation gain matrix, designed as follows

$$\frac{d}{dt}\left\{\Gamma^{-1}(t)\right\} = 2\bar{W}_p^T\bar{W}_p. \tag{1.27}$$

Remark 1 *It should be noted that if* $\Gamma^{-1}(t_0)$ *is selected to be positive definite and symmetric, then* $\Gamma(t_0)$ *is also positive definite and symmetric. Therefore, it follows that both* $\Gamma^{-1}(t)$ *and* $\Gamma(t)$ *are positive definite and symmetric. From (1.27), the following expression can be obtained*

$$\dot{\Gamma} = -2\Gamma \bar{W}_p^T \bar{W}_p \Gamma. \tag{1.28}$$

From (1.28), it is easy to conclude that $\dot{\Gamma}(t)$ *is negative semidefinite; it follows that* $\Gamma(t)$ *is bounded (the reader is referred to [31] and [32] for more detailed descriptions).*

Remark 2 *It should be noted that the parameterization of the numerator and denominator of the expression given in (1.10) may include a constant scaling factor. Since both the numerator and the denominator contain the unknown parameter vector* θ*, a constant scaling factor may exist. To account for this constant scaling factor, we include 1 as the* 4^{th} *component of the unknown vector which complicates the problem but provides us with a unique solution to find the constant scaling factor.*

Remark 3 *The projection strategy given in (1.25) ensures that the term is positive. A second projection may be used to ensure that the* 4^{th} *component of the estimate vector is always non-zero. As seen by subsequently presented simulations and experimental results, the* 4^{th} *component of the estimate vector was always non-zero; thus, for the sake of simplicity the second projection is not included in this manuscript.*

Stability Analysis

Theorem 1 *The update law defined in (1.25) ensures that* $\left\|\tilde{\theta}(t)\right\| \to 0$ *as* $t \to \infty$ *provided that the following persistent excitation condition [33] holds*

$$\gamma_1 I_4 \leq \int_{t_0}^{t_0+t'} \bar{W}_p^T(\tau) \bar{W}_p(\tau) d\tau \leq \gamma_2 I_4 \tag{1.29}$$

where γ_1,γ_2 *are positive constants,* $I_4 \in \mathbb{R}^{4\times 4}$ *is an identity matrix*[1]*, and* $t' \in \mathbb{R}$ *is a positive constant.*

[1]Through out the paper, I_n denotes a standard $n \times n$ identity matrix.

Proof. See Appendix A.

Remark 4 *The parameter vector $\hat{\theta}(t)$ provides a scaled estimate of the Euclidean coordinates of the object features relative to the world frame. Since the last element in the unknown constant parameter vector is equal to 1 (see (1.14)), the scale factor can be computed as*

$$\lambda = \hat{\theta}_4 \tag{1.30}$$

where $\lambda(t) \in \mathbb{R}$ is the scale factor for the object feature and $\hat{\theta}_4(t) \in \mathbb{R}$ is the last entry of $\hat{\theta}(t)$. It should be noted that $\hat{\theta}_4(t)$ is always nonzero which is guaranteed by the projection algorithm introduced in (1.25). The estimates of the Euclidean coordinates of the object feature can now be recovered as follows

$$\hat{x}_{fi} = \frac{1}{\lambda}\hat{\theta}_i$$

where $\hat{x}_{fi}(t)$ and $\hat{\theta}_i(t)$ $\forall\ i = 1, 2, 3$ are the i^{th} element of the corresponding vector.

Simulation Results

A detailed simulation study was conducted to evaluate the performance of the proposed estimation technique using the Mathworks Simulink program. First, an independent simulation study was performed which was followed by comparative simulation studies with some of the existing velocity measurement based range observers.

Independent Simulation Study

The 3D Euclidean coordinates of an object feature relative to the world frame, x_f, was selected as follows

$$x_f = [1 \quad 1.5 \quad 2.5]^T \text{ m}. \tag{1.31}$$

The following translation vector $x_b(t)$ and the angular rotation $q_b(t) \in \mathbb{R}^3$ (yaw-pitch-roll about x-y-z axes) were given to the mechanical system

$$x_b = [0 \quad 0 \quad \sin(2\pi t)]^T \text{ m}\,, \qquad\qquad q_b = [0 \quad 0 \quad 2\pi t]^T \text{ rad}. \tag{1.32}$$

The measurable rotation matrix $R_b(t)$ was generated using $q_b(t)$. In addition, the intrinsic calibration matrix for a typical 640×480 camera, and the extrinsic parameters were specified as follows

$$A = \begin{bmatrix} 810 & 0 & 320 \\ 0 & 820 & 240 \end{bmatrix} , \qquad R_c = I_3 , \qquad x_c = [0.5 \quad 0 \quad 0.1]^T \text{ m}. \quad (1.33)$$

The initial condition for the estimator was set as $\hat{\theta}_i(t_0) = 180 \, \forall i = 1, .., 4$. The following estimator gains were selected based on trial-and-error

$$\Gamma^{-1}(t_0) = 8000 I_4 , \qquad \alpha = 300. \quad (1.34)$$

Two different sub-cases were considered in the simulation study without changing any of the above mentioned parameters: Case 1 was without any additive noise and Case 2 was with additive-white-Gaussian noise (AWGN) injected into the measured pixel coordinates $u(t)$ and $v(t)$ using the awgn() function of Matlab. A constant signal-to-noise ratio (SNR) of 20 was maintained. Although the measurable position signals are rarely noisy, still to test the efficiency of the proposed estimator, $x_b(t)$ and $q_b(t)$ were corrupted by AWGN of SNR 40. Additonally, in Case 2, the camera calibration parameters were disturbed by 2% of their actual values in order to account for inaccurate camera calibration. In other words, A, R_c, and x_c in the regression matrices were taken as 0.98 times their respective values given in (1.33).

Fig. 1.2 shows $\hat{x}_{fi}(t) \ \forall i = 1, 2, 3$, the estimates of the constant 3D Euclidean coordinates of the object feature relative to the world frame with and without additive noise. $\hat{x}_{fi}(t)$ without additive noise (*i.e.*, Case 1) are shown in Figs. 1.2(a)-(c), and $\hat{x}_{fi}(t)$ with additive noise and inaccurate camera calibration parameters (*i.e.*, Case 2) are shown in Figs. 1.2(d)-(f) $\forall i = 1, 2, 3$. Range estimation errors (*i.e.*, $z(t) - \hat{z}(t)$) for Case 1 and Case 2 are shown in Fig. 1.3(a) and Fig. 1.3(b), respectively. It can be seen from these figures that the estimation errors converge quickly and an accurate estimation of the range along with 3D coordinates relative to the world frame are obtained. It can also be inferred from the figures that the developed range

estimation technique is robust to noisy measurements and provides good estimates of the 3D coordinates of the object feature relative to the world frame along with an estimate of the range even in presence of noise in all the measurable signals as well as inaccurate information of the camera calibration parameters. It should be noted that $\hat{x}_f(t)$ can be utilized to obtain other 3D coordinates of the object feature relative to the moving camera from (1.15).

Comparative Simulation Study

Although, the proposed range estimator is based on a different approach than the existing range observers (*i.e.*, it utilizes position measurements instead of velocity measurements) two comparative simulation studies were conducted to obtain a better understanding of its performance. The two comparisons were done with the results reported by Chen *et al.* in [1], and by De Luca *et al.* in [2], respectively.

Comparison with the work by Chen *et al.* in [1]

For the comparison, the same periodic movement of a single object feature as described by [1] was considered as follows

$$\frac{d}{dt}\begin{bmatrix} x_1(t) \\ x_2(t) \\ x_3(t) \end{bmatrix} = \begin{bmatrix} 0 & -2\pi & 0 \\ 2\pi & 0 & 0 \\ 0 & 0 & 0 \end{bmatrix}\begin{bmatrix} x_1(t) \\ x_2(t) \\ x_3(t) \end{bmatrix} + \begin{bmatrix} 0 \\ 0 \\ 2\pi\cos(2\pi t) \end{bmatrix} \tag{1.35}$$

$$[x_1(0) \quad x_2(0) \quad x_3(0)]^T = [1 \quad 1 \quad 2]^T \tag{1.36}$$

which was decomposed [24] giving the angular and linear velocities assuming no linear deformation. The time integral of these velocities were used to compute the angular and linear positions of the camera. In the simulations presented earlier in this section the camera's calibration parameters were picked to represent a real-world system. However, the camera's intrinsic and extrinsic calibration parameters for the simulations in the comparison study were chosen to match the parameters given in [1] and were defined as follows

$$A = \begin{bmatrix} 1 & 0 & 0 \\ 0 & 1 & 0 \end{bmatrix}, \qquad R_c = I_3, \qquad x_c = [0 \quad 0 \quad 0]^T \text{ m}. \tag{1.37}$$

An image space feature trajectory was generated based on the camera motion described by (1.35) and (1.36) and then corrupted by 1% random noise as in [1]. The initial condition for the estimate vector was taken as 0.01 for all its entries and the same estimator gains given in (1.34) were used. Fig. 1.4 shows the estimation error between $y_3(t)$ and its estimate $\hat{y}_3(t)$ obtained by our proposed estimator where $y_3(t) = \frac{1}{z(t)}$ with $z(t)$ equal to the range of the object feature. The result in Fig. 1.4 shows that the proposed estimator is superior to the estimator presented by [1][2] in terms of transient response, convergence time, and error value. Also, as pointed out by [1], the method proposed by [17] can not be applied to this motion.

Comparison with the work by De Luca *et al.* in [2]

For this comparison, the camera was translated and rotated about the x and z axes as described in [2]. As mentioned in [2], this kind of complex motion could not be addressed with the methods of Matthies *et al.* in [10] or Smith *et al.* in [34]. The following translation vector $x_b(t)$ and the angular rotation $q_b(t)$ were given to the mechanical system

$$x_b = [(0.1/2\pi)\sin(2\pi t) \quad 0 \quad (0.5/\pi)\sin(\pi t)]^T \text{ m} \tag{1.38}$$

$$q_b = [(1.2/\pi)\sin(0.5\pi t) \quad 0 \quad t]^T \text{ rad.} \tag{1.39}$$

Similar to the previous simulation section, the measurable rotation matrix $R_b(t)$ was generated using $q_b(t)$. The following camera parameters were taken so as to match the parameters given in [2]

$$A = \begin{bmatrix} 128 & 0 & 0 \\ 0 & 128 & 0 \end{bmatrix}, \qquad R_c = I_3, \qquad x_c = [0 \quad 0 \quad 0]^T \text{ m.} \tag{1.40}$$

The 3D Euclidean coordinates of an object feature relative to the world frame, x_f, was selected as follows

$$x_f = [0.08 \quad -0.08 \quad 0.5]^T \text{ m.} \tag{1.41}$$

[2]The reader is referred to Fig. 3 in [1] for the comparison.

The initial condition for the estimator was set as $\hat{\theta}_i(t_0) = 10 \, \forall i = 1, .., 4$, and the same estimator gains given in (1.34) were used.

Fig. 1.5 shows the estimates $\hat{x}_{fi}(t) \ \forall i = 1, 2, 3$ and Fig. 1.6 shows the range estimation error by using the proposed estimator. It can be seen from these figures that the proposed estimation technique provides accurate results even for a complex camera motion, and the results are comparable with the work presented by De Luca *et al.* in [2][3] where noise-free velocity measurements were utilized. As mentioned earlier, in practice, velocity measurements could be a lot noisier than position measurements; hence, direct utilization of position measurements could be preferred.

Experimental Results

In this section, experimental results of the estimator presented in this paper are shown for two different stationary objects: a checker-board and a doll-house. A practical implementation of the estimator involves (a) hardware for image acquisition, (b) implementation of an algorithm for feature-tracking, and (c) software implementation of the range estimator itself.

A calibrated 640×480 monochrome CCD camera (Sony XC-ST50) equipped with a Navitar CCTV lens (focal length = 8 mm) was mounted on the end-effector of a Puma 560 robotic manipulator, as shown in Fig. 1.7. The end-effector of the PUMA robot having an initial distance of approximately 1.5 m from the object was moved along a smooth sinusoidal trajectory along x, y, and z axes commanded by a PC running the QNX 6.2 operating system as shown in Fig. 1.8. Fig. 1.9(a) and Fig. 1.9(b) show the linear and angular velocity measurements respectively for the same trajectory. It can be seen from these figures that velocity measurements are very noisy; hence, very difficult to utilize for range estimation using a velocity based range observer. A second PC, dedicated to image processing and equipped with an Imagenation PXC200AF frame-grabber board capable of acquiring images in real time

[3]The reader is referred to Fig. 2 in [2] for the comparison.

(30 fps) over the PCI bus was interfaced with the camera. The robot manipulator is equipped with position sensors for all the 6 joints. In order to measure $R_b(t)$ and $x_b(t)$, the joint positions were measured and forward kinematics was utilized to obtain a 4x4 homogenous transformation matrix which contained the 3x3 rotation matrix, $R_b(t)$, and the 3x1 translation vector, $x_b(t)$. In this experiment, the robot control and vision system have been separated, this requires synchronization between the two systems. Therefore, a 15 Hz digital signal was sent out to the image processing PC from the robot control PC to trigger the frame-grabber to acquire images. The same trigger signal was used to record the end-effector position of the robot relative to the world frame, in a file to be processed off-line later.

For each object multiple feature points were selected, and an implementation of the Kanade-Lucas-Tomasi feature tracking algorithm [35] available online [36] was used to track these feature points from one frame to another. The implementation, written in C++, allowed the user to select feature points manually and track all the selected feature points in the sequence of images. The output of the program was a data file that contained pixel coordinates of all the object features for all the frames that were successfully tracked in the sequence of images. It is worthwhile to mention that feature tracking plays an essential role as it is desired that none of the selected features should be lost during tracking. See [37] for a discussion on issues related to selection and tracking of feature points. The intrinsic calibration matrix of the camera was found using MATLAB camera calibration toolbox [38] to be the following

$$A = \begin{bmatrix} 825 & 0 & 320 \\ 0 & 835 & 243 \end{bmatrix}. \tag{1.42}$$

The camera's coordinate frame was aligned with the robot end-effector coordinate frame in order to produce the following rotation matrix from the camera to the end-effector

$$R_c = \begin{bmatrix} -1 & 0 & 0 \\ 0 & -1 & 0 \\ 0 & 0 & 1 \end{bmatrix}. \tag{1.43}$$

The translation vector between the camera and the end-effector was obtained as follows

$$x_c = [0 \quad 0.0681 \quad 0.0311]^T \text{ m.} \tag{1.44}$$

The proposed estimation algorithm was implemented off-line using Mathworks Simulink program using the data obtained from the vision tracking system and the robot control PC. For each object, Euclidean distances between the object features were measured, and the estimated Euclidean distances were computed from the estimates of $x_f(t)$ obtained from the estimator. The estimator was tested on two different objects using the above parameters.

Object I: Checker-board

Nine feature points were selected and tracked on a static checker-board, and six Euclidean distances between the object features were measured as shown in Fig. 1.10. The initial condition for the estimate vector $\hat{\theta}(t_0)$ was taken as 10 for all the entries. The following estimator gains were selected based on trial-and-error

$$\alpha = 300, \qquad \Gamma_j^{-1}(t_0) = 1000 I_4 \tag{1.45}$$

where the subscript j denotes j^{th} object feature. The Euclidean distance estimation errors between the representative object features are shown in Fig. 1.11. The inset shows the Euclidean estimation errors zoomed in for the last 20 seconds. The evolution of range estimate for a single object feature is shown in Fig. 1.12. For clarity of the figure, and to emphasize the fact that the estimated range is noise-free, we show the range estimation for only one object feature.

Object II: Doll-house

A stationary doll-house was taken as the second object. Nine feature points were selected and tracked on it, and six Euclidean distances between the object features were measured as shown in Fig. 1.13. Similar to the checker-board experiment, the initial condition for the estimate vector $\hat{\theta}(t_0)$ was taken as 10 for all the entries, and

same estimator gains given in (1.45) were used. The Euclidean distance estimation errors are shown in Fig. 1.14. The inset shows the Euclidean estimation errors zoomed in for the last 20 seconds.

Discussion

The experimental results clearly show good and robust performance of the estimator. The distance estimation errors are less than 1 cm for all the lengths in both the experiments; therefore, it can be easily inferred that the 3D Euclidean coordinates of the object features relative to the world frame are identified with good precision. It can also be inferred from Fig. 1.12 that the evolution of range variable is noise-free as opposed to [2] where evolution of range is quite noisy. Fig. 1.9 clearly shows that velocity measurements are very noisy as compared to the position measurements in Fig. 1.8; thus, a need of position based range estimator is evident. These velocity measurements are obtained by differentiation of the position signal and then filtered using a second order low pass filter. As mentioned previously, $\hat{x}_f(t)$ can be utilized to obtain other 3D coordinates of the object feature relative to the moving camera from (1.15).

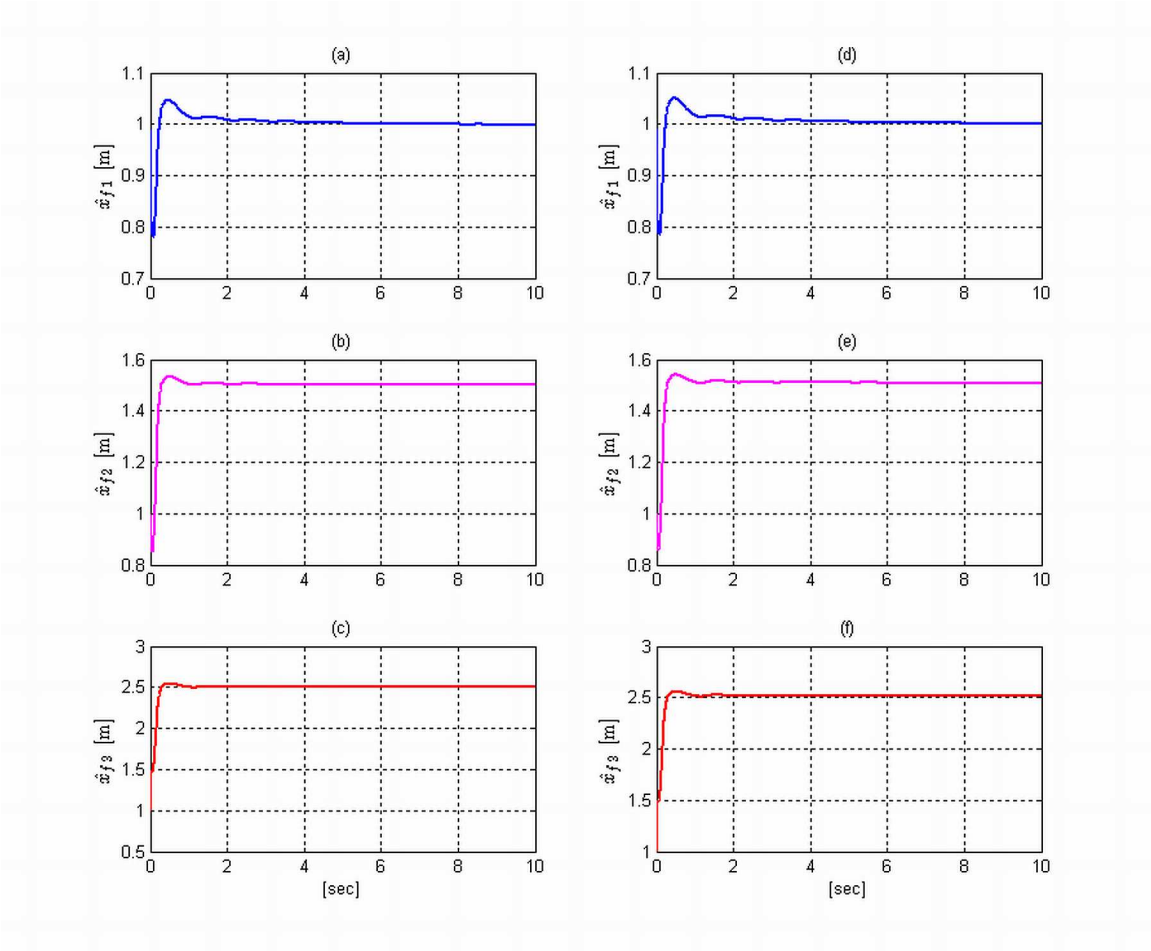

Figure 1.2 Independent simulation study: Estimates $\hat{x}_f(t)$ (a)-(c) without additive noise (Case 1), and (d)-(f) in presence of additive noise and inaccurate information of camera calibration parameters (Case 2).

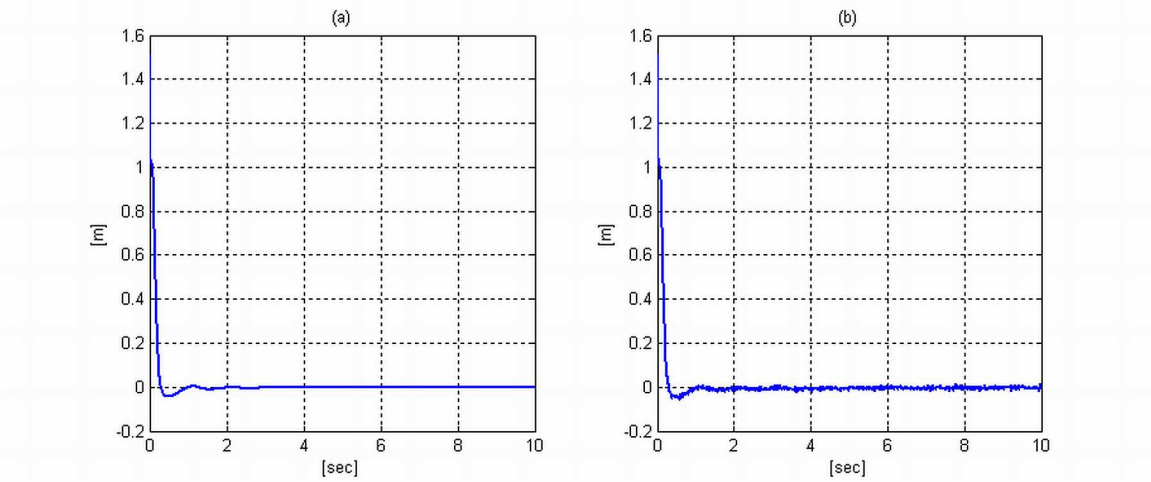

Figure 1.3 Independent simulation study: Range estimation error $z(t) - \hat{z}(t)$ (a) without additive noise (Case 1), and (b) in presence of additive noise and inaccurate information of camera calibration parameters (Case 2).

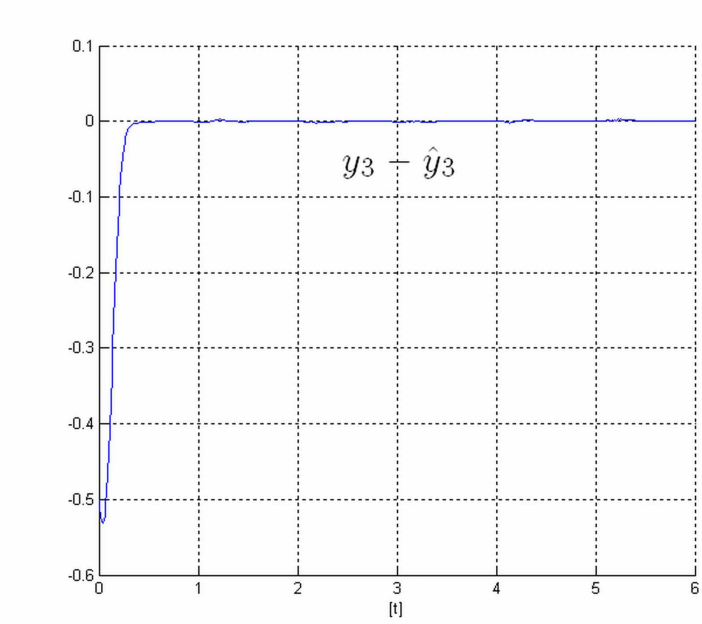

Figure 1.4 Comparative simulation study with [1]: Error between $y_3(t)$ and its estimate $\hat{y}_3(t)$ by using the proposed estimator.

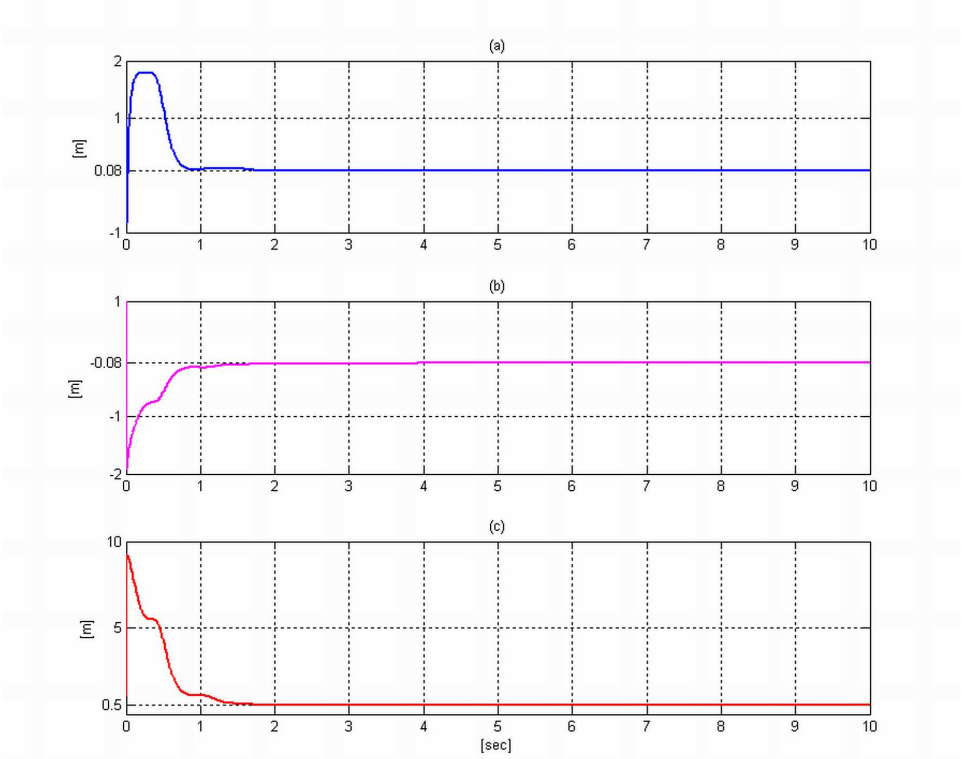

Figure 1.5 Comparative simulation study with [2]: Estimates of (a) $\hat{x}_{f1}(t)$, (b) $\hat{x}_{f2}(t)$, and (c) $\hat{x}_{f3}(t)$ by using the proposed estimator.

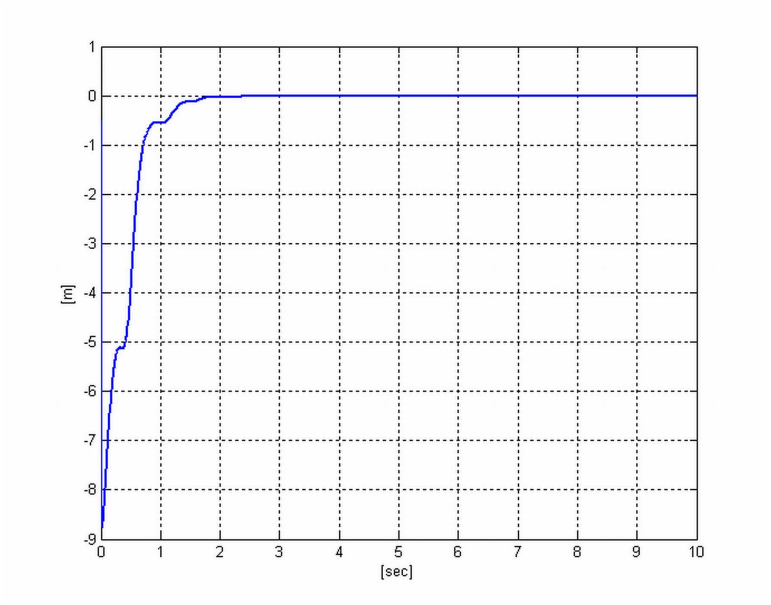

Figure 1.6 Comparative simulation study with [2]: Range estimation error $z(t) - \hat{z}(t)$ by using the proposed estimator.

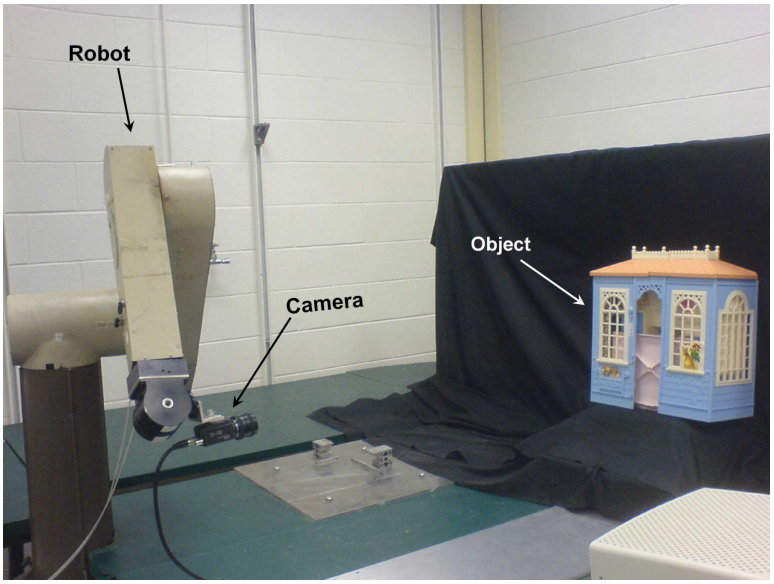

Figure 1.7 Experimental testbed with camera, robot and object

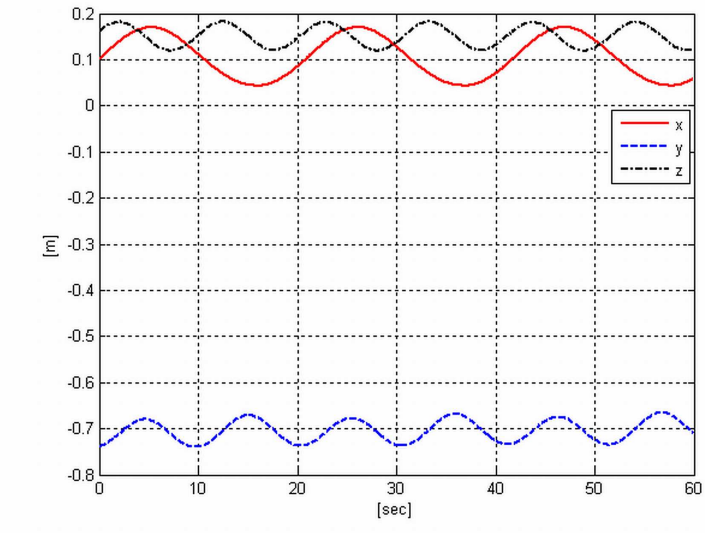

Figure 1.8 Experiment: Robot position measurements $x_b(t)$.

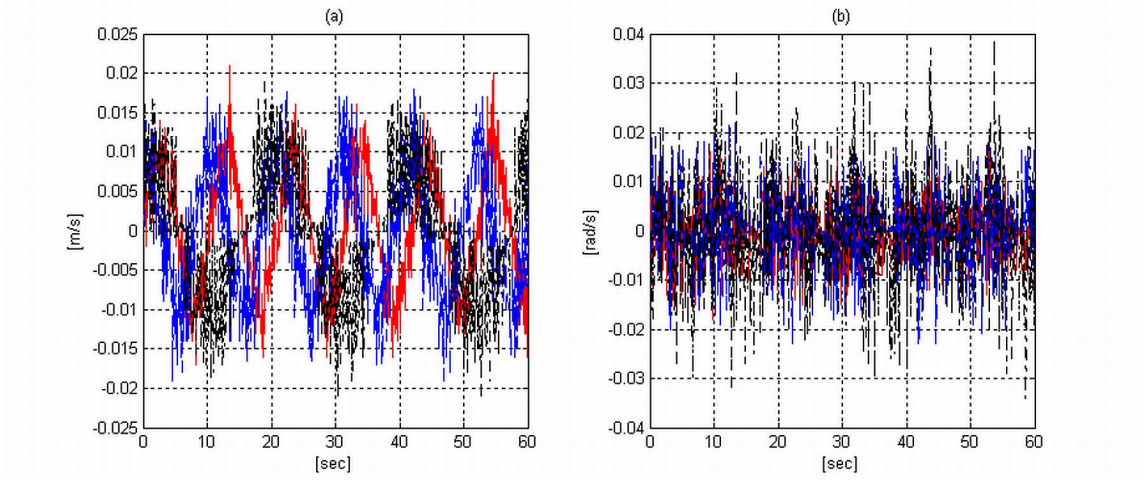

Figure 1.9 Experiment: Robot velocity measurements (a) linear velocity and (b) angular velocity.

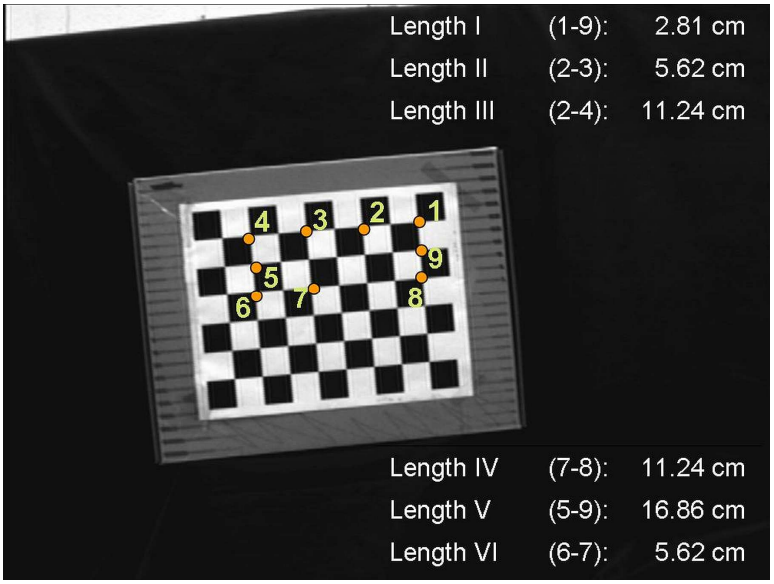

Figure 1.10 A frame from the checker-board image sequence with the tracked feature points along with true Euclidean distances between the object features.

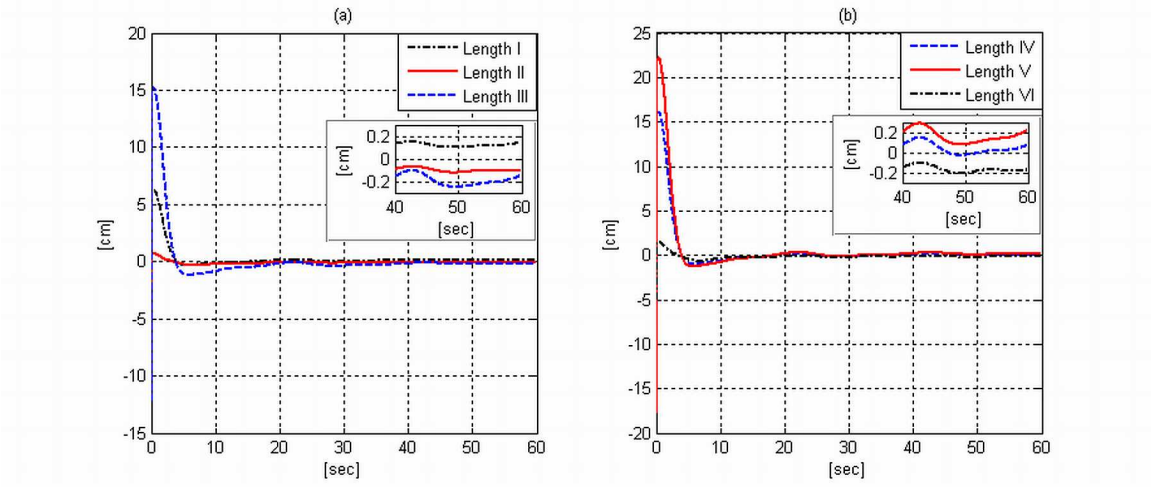

Figure 1.11 Experiment: Euclidean distance estimation error (checker-board).

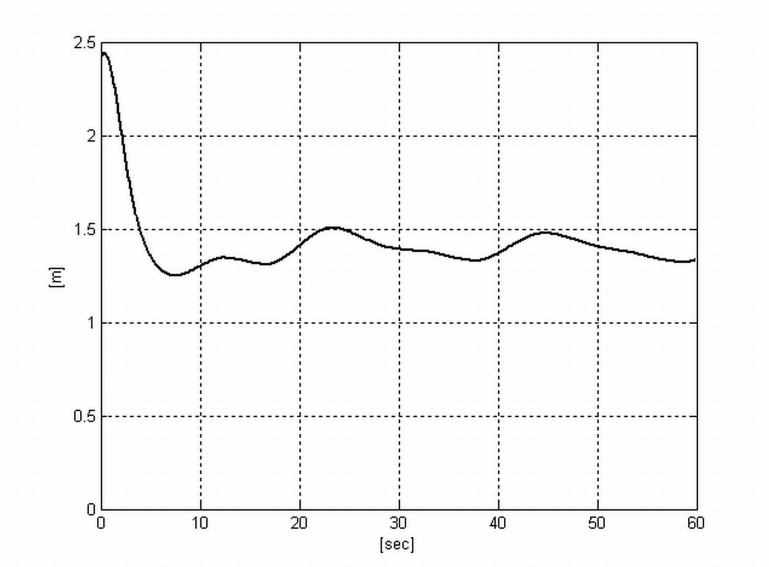

Figure 1.12 Experiment: Range estimate $\hat{z}(t)$ for a single object feature (checker-board).

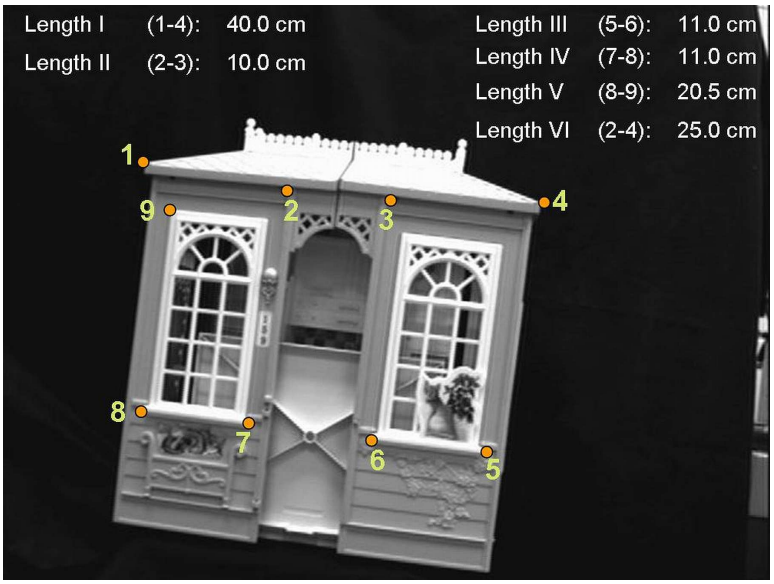

Figure 1.13 A frame from the doll-house image sequence with the tracked feature points along with true Euclidean distances between the object features.

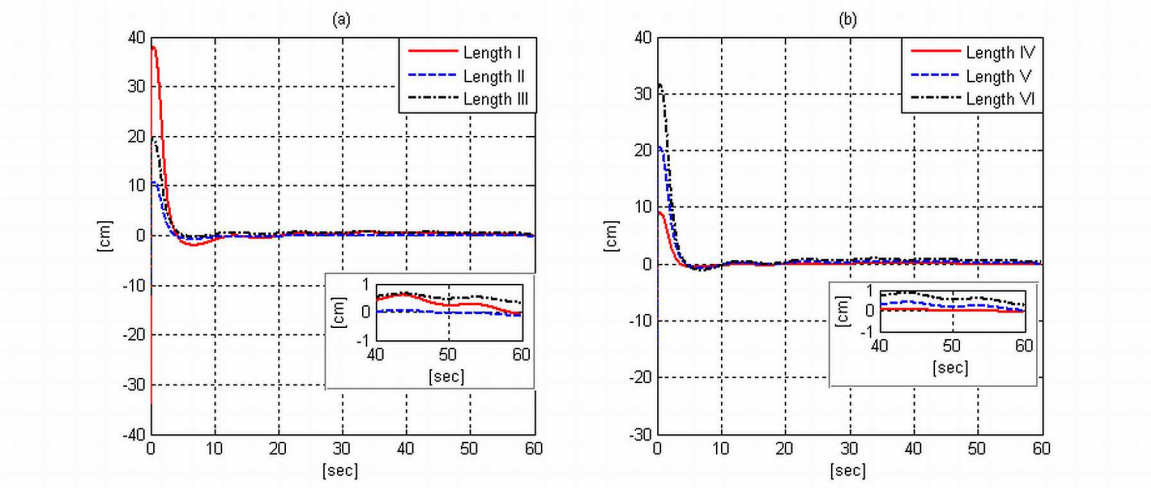

Figure 1.14 Experiment: Euclidean distance estimation error (doll-house).

CHAPTER 2
EUCLIDEAN POSITION ESTIMATION OF STATIC FEATURES USING A MOVING UNCALIBRATED CAMERA

Introduction

3D reconstruction of an object, where the Euclidean coordinates of the features on a moving or fixed object are recovered from a sequence of two-dimensional (2D) images, has received noteworthy attention over the last several years. The recovery of the 3D Euclidean coordinates is usually done by mounting a camera on a moving vehicle such as an unmanned aerial vehicle (UAV) or a mobile robot which travels through the environment and captures images of static objects or features. 3D reconstruction or 3D Euclidean position estimation has significance in several applications such as autonomous vehicle navigation, aerial tracking, path planning, surveillance, etc.

Although, the problem of Euclidean reconstruction is inherently nonlinear, linearization based techniques, such as the extended Kalman filter (EKF) [10], [12], have been used quite frequently. However, linearized motion models can cause significant incosistencies in solutions, as noted in [15]. Moreover, EKF involves *a priori* knowledge of noise distribution. To overcome the shortcomings of the linear model several researchers focused on utilizing nonlinear system analysis and estimation tools to develop nonlinear state observers for depth estimation or 3D reconstruction [1], [18], [19], [20], [21], [22], [25], [26], [39], [40]. All these works utilized velocity measurement of the camera or the object in order to estimate the depth where the camera's extrinsic calibration parameters (rotational matrix and translation vector of the camera relative to its mounting frame) were not considered, and the intrinsic calibration parameters (a matrix consisting functions of the camera's internal parameters; namely, focal length, scaling factors, pixel coordinates of the principal point, and camera axes angles) were set to unity to simplify the problem. In practice, these calibration parameters are often required to estimate the depth or the structure of an object. In

other words, the aforementioned works require the camera to be calibrated. In [27], a valid intrinsic calibration matrix of the camera was assumed to recover the depth of an object. Our recent work [41] utilized position measurements of the camera to recover the structure of an object. However, this work assumed a calibrated camera, *i.e.*, the intrinsic and the extrinsic camera calibration parameters were assumed to be known. The work in [41] was extended and evaluated experimentally in [42] where it was realized that calibrating a camera is tedious and complicated, especially calibration of the camera's extrinsic parameters.

Hartley and Zisserman in [43] discussed techniques where the essential matrix (when intrinsic calibration parameters are known) can be decomposed to obtain camera's extrinsic calibration parameters. This technique usually results in multiple solutions for the rotation matrix, and the translation vector is found up to an ambiguous scale factor; thus, making it difficult to select the correct solution. If the intrinsic parameters are also unknown along with extrinsic parameters, the fundamental matrix can be obtained. However, the knowledge of just the fundamental matrix is not sufficient to estimate the depth information. It is also noted that recovering the 3D Euclidean coordinates of an object from a sequence of its 2D images with a single uncalibrated camera is a very difficult task. In [44], Hartley proposed a multiple-step algorithm for Euclidean reconstruction from uncalibrated camera views. It was noted in [45] that a true 3D Euclidean scene of an object using a single camera with unconstrained motion and unknown parameters can not be reconstructed. These issues motivated us to develop a simple and an easily implementable estimator for 3D Euclidean position estimation using a single uncalibrated camera where both, the intrinsic and the extrinsic camera calibration parameters are unknown.

In this paper, our goal is to develop an estimator to identify the 3D Euclidean coordinates of features on a stationary object by mounting an uncalibrated camera on a mobile platform whose position is measurable. To achieve this goal, first a geometric model is developed to relate the fixed features on the object with the moving camera

where the 3D Euclidean coordinates of the other object is considered to be available *a priori*. The model is then parameterized for known and unknown object features. A prediction error formulation is then presented along with an auxiliary prediction error that allow us to utilize nonlinear estimation theory to design two adaptive least-squares estimators to compensate for the unknown camera calibration parameters and to estimate the structure. We show that the developed structure estimator identifies the Euclidean coordinates of the object features upon satisfaction of a persistency of excitation (PE) condition, and is not dependent on an accurate estimation of the unknown camera calibration parameters. The proposed estimation technique can be useful in places where a known object exists, and the 3D Euclidean coordinates of another object has to be estimated. Also, when a camera on a mechanical system is replaced or orientation of the camera is changed, it is not required to recalibrate the camera if a known object is present. The developed estimator provides good results and is robust to noise as demonstrated by the simulation results. The validity of the proposed estimation technique is also demonstrated by experimental results.

Geometric Model

To develop a geometric relationship between a perspective moving camera and features on known, and unknown static objects, we define an orthogonal coordinate frame, denoted by $\mathcal{C}$, whose origin coincides with the optical center of the camera, an inertial coordinate frame, denoted by $\mathcal{W}$, and an orthogonal coordinate frame, denoted by $\mathcal{B}$ (see Fig. 2.1). In Fig. 2.1, $\mathcal{F}_{si}$ $\forall i = 1, .., n$ denotes the i$^{\text{th}}$ object feature whose unknown 3D Euclidean coordinates relative to the world frame $\mathcal{W}$ are denoted as the constant $\omega_{si} \in \mathbb{R}^3$, and $\mathcal{F}_{cj}$ $\forall j = 1, .., m$ represents the j$^{\text{th}}$ object feature[4] whose corresponding 3D Euclidean coordinates relative to the world frame $\mathcal{W}$ are known *a priori* and denoted by the constant $\omega_{cj} \in \mathbb{R}^3$. The 3D coordinates

[4]Through out the paper the subscript si denotes the i$^{\text{th}}$ feature whose 3D coordinates relative to the frame $\mathcal{W}$ is unknown, and cj denotes the j$^{\text{th}}$ feature whose 3D coordinates relative to the frame $\mathcal{W}$ is known.

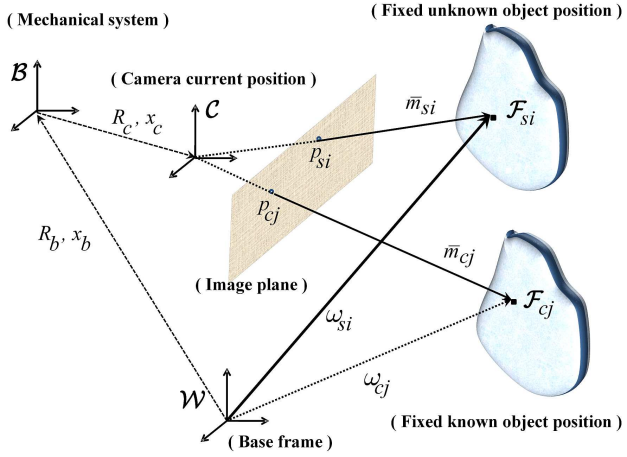

Figure 2.1 Geometric relationships between the fixed objects, mechanical system, and the camera.

of the object features relative to the camera frame $\mathcal{C}$, denoted by $\bar{m}_{si/cj}(t) \in \mathbb{R}^3$, is defined as follows[5]

$$\bar{m}_{si/cj} \triangleq \begin{bmatrix} x_{si/cj} & y_{si/cj} & z_{si/cj} \end{bmatrix}^T. \tag{2.1}$$

In the subsequent development, it is assumed that both the objects are always in the field of view of the camera; hence, the distances from the origin of $\mathcal{C}$ to all the features are always positive and bounded. To relate the coordinate systems, let $R_b(t) \in SO(3)$ and $x_b(t) \in \mathbb{R}^3$ denote the measurable rotation matrix and the measurable translation vector, respectively, from $\mathcal{B}$ to $\mathcal{W}$, expressed in $\mathcal{W}$. Let $R_c \in SO(3)$ and $x_c \in \mathbb{R}^3$ denote the unknown rotation matrix and the unknown translation vector, respectively, from $\mathcal{C}$ to $\mathcal{B}$, expressed in $\mathcal{B}$. The pixel coordinates of the object features projected on the image plane, denoted by $p_{si/cj}(t) \in \mathbb{R}^3$, is defined as follows

$$p_{si/cj} \triangleq \begin{bmatrix} u_{si/cj} & v_{si/cj} & 1 \end{bmatrix}^T \tag{2.2}$$

where $u_{si/cj}(t)$, $v_{si/cj}(t) \in \mathbb{R}$. The projected pixel coordinates of the features are

[5]The notation $Y_{si/cj}$ implies Y_{si} or Y_{cj} through out the paper. If the left-hand side of any expression is considered with the subscript si then the right-hand side of the expression is with si, and similarly for cj.

related to the Euclidean coordinates by the pin-hole camera model [29] such that

$$p_{si/cj} = \frac{1}{z_{si/cj}} A \bar{m}_{si/cj} \tag{2.3}$$

where $A \in \mathbb{R}^{3\times3}$ is the unknown constant intrinsic camera calibration matrix of the following form [30]

$$A \triangleq \begin{bmatrix} fk_u & fk_u \cot\phi & u_0 \\ 0 & \frac{fk_v}{\sin\phi} & v_0 \\ 0 & 0 & 1 \end{bmatrix} \tag{2.4}$$

where k_u, $k_v \in \mathbb{R}$ denote camera scaling factors, u_0, $v_0 \in \mathbb{R}$ represent the pixel coordinates of the principal point, $\phi \in \mathbb{R}$ is the angle between the camera axes, and $f \in \mathbb{R}$ is the camera focal length.

Parameterization of the Model

In this section, the parameterization of $A\bar{m}_{si/cj}(t)$ and the depth variable $z_{si/cj}(t)$ are presented. The nonlinear static model given in (2.3) is parameterized for two cases: case 1, where the 3D coordinates of the features relative to $\mathcal{W}$ are unknown (*i.e.*, for *si*), and case 2, where the 3D coordinates of the features relative to $\mathcal{W}$ are known *a priori* (*i.e.*, for *cj*).

From Fig. 2.1, $\bar{m}_{si/cj}(t)$ can be written as follows [41]

$$\bar{m}_{si/cj} = R_c^T \left[R_b^T \left(\omega_{si/cj} - x_b \right) - x_c \right]. \tag{2.5}$$

After substituting (2.5) into (2.3), the pixel coordinates for the object features can be written as follows

$$p_{si/cj} = \frac{1}{z_{si/cj}} A R_c^T \left[R_b^T (\omega_{si/cj} - x_b) - x_c \right] \tag{2.6}$$

and the corresponding depth $z_{si/cj}(t)$ can be written as follows

$$z_{si/cj} = R_{c3}^T \left[R_b^T (\omega_{si/cj} - x_b) - x_c \right] \tag{2.7}$$

where $R_{c3}^T \in \mathbb{R}^{1\times3}$ is the last row of R_c^T.

Case 1: For the object features that have unknown 3D coordinates relative to $\mathcal{W}$,

$p_{si}(t)$ is parameterized as follows

$$p_{si} = \frac{1}{\Pi(X, \theta_{c2})\theta_{si}} W(X, \theta_{c1})\theta_{si} \quad \forall i = 1, .., n \tag{2.8}$$

where

$$\Pi(\cdot)\theta_{si} = z_{si} = R_{c3}^T \left[R_b^T (\omega_{si} - x_b) - x_c \right] \tag{2.9}$$

$$W(\cdot)\theta_{si} = A R_c^T \left[R_b^T (\omega_{si} - x_b) - x_c \right]. \tag{2.10}$$

In (2.8)-(2.10), $\theta_{c1} \in \mathbb{R}^{12}$ and $\theta_{c2} \in \mathbb{R}^4$ are the constant vectors containing all the camera parameters [46], the variable $X(t) \in \mathbb{R}^{q \times r}$ contains the combinations of the elements of the measurable signals $R_b(t)$ and $x_b(t)$, $\Pi(\cdot) \in \mathbb{R}^{1 \times 4}$, $W(\cdot) \in \mathbb{R}^{3 \times 4}$ are regression matrices, and $\theta_{si} \in \mathbb{R}^4$ is an unknown constant parameter vector, which is defined as

$$\theta_{si} \triangleq \begin{bmatrix} \omega_{si1} & \omega_{si2} & \omega_{si3} & 1 \end{bmatrix}^T \tag{2.11}$$

where $\omega_{sir} \in \mathbb{R}$ $\forall r = 1, 2, 3$, is the unknown Euclidean coordinate of the i$^{\text{th}}$ feature for the unknown object relative to $\mathcal{W}$.

Case 2: For known 3D coordinates of the features relative to $\mathcal{W}$, $p_{cj}(t)$ is parameterized as follows [46]

$$p_{cj} = \frac{1}{\Pi_{xj}(\bar{X})\theta_{c2}} W_{xj}(\bar{X})\theta_{c1} \quad \forall j = 1, .., m \tag{2.12}$$

where $W_{xj}(\cdot) \in \mathbb{R}^{3 \times 12}$, $\Pi_{xj}(\cdot) \in \mathbb{R}^{1 \times 4}$ are known regression matrices ($\bar{X}(t) \in \mathbb{R}^{s \times t}$ contains combinations of the measurable signals and structure information of the known object).

It should be noted that $z_{si/cj}(t)$ is assumed to satisfy the following inequalities

$$\rho_{si/cj}(\cdot) \geq z_{si/cj}(t) = \text{denum}(p_{si/cj}) \geq \varepsilon_{si/cj} > 0 \tag{2.13}$$

where denum$(\cdot)$ denotes the denominator of $(\cdot)$, $\rho_{si/cj}(\bar{m}_{si/cj}) \in \mathbb{R}$ is a positive function and $\varepsilon_{si/cj} \in \mathbb{R}$ is a positive constant $\forall i, j$. The objective of this work is to identify the 3D Euclidean coordinates of the features on an unknown object θ_{si} in the presence

of unknown camera parameters θ_{c1}, θ_{c2}[6]. It is to be noted that our novel structure estimation technique guarantees the estimation of the 3D Euclidean coordinates upon the satisfaction of a PE condition, and it does not require an accurate estimation of the camera parameters. Estimating the camera parameters accurately is beyond the scope of this paper.

Euclidean Structure Estimation

In this section, a prediction error formulation for the parameterized model given in (2.8) is presented along with an auxiliary prediction error formulation which accounts for the unknown camera parameters. A structure estimator is then presented along with the stability analysis.

Prediction Error Formulation

To proceed with the error development, the term $\Pi(\cdot)\theta_{si}$ is multiplied to the both sides of (2.8) that results in the following expression

$$p_{si}\Pi\theta_{si} = W\theta_{si}. \tag{2.14}$$

The estimate of (2.14) can be written as follows

$$\hat{p}_{si}\hat{\Pi}\hat{\theta}_{si} = \hat{W}\hat{\theta}_{si} \tag{2.15}$$

where $\hat{p}_{si}(t) \in \mathbb{R}^3$ and $\hat{\theta}_{si}(t) \in \mathbb{R}^4$ are the estimates of $p_{si}(t)$ and θ_{si}, respectively, $\hat{\Pi}$ and $\hat{W}$ denote $\Pi(X, \hat{\theta}_{c2})$ and $W(X, \hat{\theta}_{c1})$, respectively where $\hat{\theta}_{c1}(t) \in \mathbb{R}^{12}, \hat{\theta}_{c2}(t) \in \mathbb{R}^4$ are the estimates of θ_{c1} and θ_{c2}, respectively. To facilitate the development, the terms $\hat{W}\theta_{si}$ and $\hat{p}_{si}\Pi\theta_{si}$ are added and subtracted from the right-hand-side and the left-hand-side of (2.14), respectively that yields the following expression

$$[p_{si} - \hat{p}_{si}]\,\Pi\theta_{si} + \hat{p}_{si}\Pi\theta_{si} = \hat{W}\theta_{si} + [W - \hat{W}]\theta_{si}. \tag{2.16}$$

[6]The estimates of A, R_c, and x_c can be obtained from the estimates of θ_{c1}, θ_{c2} (see [46] for a detailed explanation).

After subtracting (2.15) from (2.16), the following expression is obtained

$$\tilde{p}_{si}\Pi\theta_{si} + \hat{p}_{si}\Pi\theta_{si} - \hat{p}_{si}\hat{\Pi}\hat{\theta}_{si} = \hat{W}\tilde{\theta}_{si} + \tilde{W}\theta_{si} \tag{2.17}$$

where $\tilde{p}_{si}(t) \triangleq p_{si} - \hat{p}_{si} \in \mathbb{R}^3$ is the prediction error for the i$^{\text{th}}$ feature point $\forall i = 1, .., n$, $\tilde{\theta}_{si}(t) \triangleq \theta_{si} - \hat{\theta}_{si} \in \mathbb{R}^4$ is the structure estimation error, and $\tilde{W}$ denotes $W(X, \tilde{\theta}_{c1})$ where $\tilde{\theta}_{c1}(t) \triangleq \theta_{c1} - \hat{\theta}_{c1} \in \mathbb{R}^{12}$. After adding and subtracting the term $\hat{p}_{si}\hat{\Pi}\theta_{si}$ to the left-hand-side of (2.17) and simplifying, the following expression can be obtained

$$\tilde{p}_{si} = \frac{1}{\Pi\theta_{si}} \left\{ \left[\hat{W} - \hat{p}_{si}\hat{\Pi}\right] \tilde{\theta}_{si} + \left[\tilde{W} - \hat{p}_{si}\tilde{\Pi}\right] \theta_{si} \right\} \tag{2.18}$$

where $\tilde{\Pi}$ denotes $\Pi(X, \tilde{\theta}_{c2})$ and $\tilde{\theta}_{c2}(t) \triangleq \theta_{c2} - \hat{\theta}_{c2} \in \mathbb{R}^4$. To ease the subsequent analysis, we combine these individual vectors $\forall i$ to obtain their respective compact forms. The combined form of the pixel coordinates and their estimates for all the feature points on the unknown object, denoted by $p_s(t), \hat{p}_s(t) \in \mathbb{R}^{3n}$, respectively, are defined as follows

$$p_s \triangleq \begin{bmatrix} p_{s1}^T & p_{s2}^T & \dots & p_{sn}^T \end{bmatrix}^T ; \hat{p}_s \triangleq \begin{bmatrix} \hat{p}_{s1}^T & \hat{p}_{s2}^T & \dots & \hat{p}_{sn}^T \end{bmatrix}^T \tag{2.19}$$

and the prediction error $\tilde{p}_s(t) \in \mathbb{R}^{3n}$ is defined as follows

$$\tilde{p}_s \triangleq p_s - \hat{p}_s = \begin{bmatrix} \tilde{p}_{s1}^T & \tilde{p}_{s2}^T & \dots & \tilde{p}_{sn}^T \end{bmatrix}^T. \tag{2.20}$$

Based on (2.18), the prediction error $\tilde{p}_s(t)$ can be written as

$$\tilde{p}_s = B\bar{W}_s\tilde{\theta}_s + BW_s\theta_s \tag{2.21}$$

where $\bar{W}_s(t) \in \mathbb{R}^{3n \times 4n}$ is a measurable signal defined as follows

$$\bar{W}_s \triangleq \begin{bmatrix} \hat{W} - \hat{p}_{s1}\hat{\Pi} & 0_{3\times4} & \dots & 0_{3\times4} \\ 0_{3\times4} & \hat{W} - \hat{p}_{s2}\hat{\Pi} & \dots & 0_{3\times4} \\ . & . & . & . \\ . & . & . & . \\ 0_{3\times4} & 0_{3\times4} & \dots & \hat{W} - \hat{p}_{sn}\hat{\Pi} \end{bmatrix} \tag{2.22}$$

and $W_s(t) \in \mathbb{R}^{3n\times 4n}$ is an auxiliary matrix defined as

$$W_s \triangleq \begin{bmatrix} \tilde{W} - \hat{p}_{si}\tilde{\Pi} & 0_{3\times 4} & ... & 0_{3\times 4} \\ 0_{3\times 4} & \tilde{W} - \hat{p}_{si}\tilde{\Pi} & ... & 0_{3\times 4} \\ . & . & . & . \\ . & . & . & . \\ 0_{3\times 4} & 0_{3\times 4} & ... & \tilde{W} - \hat{p}_{si}\tilde{\Pi} \end{bmatrix} \tag{2.23}$$

where $0_{3\times 4} \in \mathbb{R}^{3\times 4}$ is a zero matrix. In (2.21), $\theta_s \triangleq \begin{bmatrix} \theta_{s1}^T & \theta_{s2}^T & ... & \theta_{sn}^T \end{bmatrix}^T \in \mathbb{R}^{4n}$, and $B(t) \in \mathbb{R}^{3n\times 3n}$ is an auxiliary matrix defined as

$$B \triangleq \text{diag}\left\{\varphi_1, \varphi_1, \varphi_1, ..., \varphi_n, \varphi_n, \varphi_n\right\} \tag{2.24}$$

where $\varphi_i \triangleq \frac{1}{\Pi\theta_{si}} \quad \forall i = 1, .., n$. The combined form of the structure estimation errors of the features, denoted by $\tilde{\theta}_s(t) \in \mathbb{R}^{4n}$, is defined as follows

$$\tilde{\theta}_s \triangleq \theta_s - \hat{\theta}_s = \begin{bmatrix} \tilde{\theta}_{s1}^T & \tilde{\theta}_{s2}^T & ... & \tilde{\theta}_{sn}^T \end{bmatrix}^T. \tag{2.25}$$

The expression given in (2.21), can be rewritten as follows

$$\tilde{p}_s = B\bar{W}_s\tilde{\theta}_s + BS \tag{2.26}$$

where $S(t) \triangleq W_s\theta_s \in \mathbb{R}^{3n}$. After utilizing (2.18), $S_i(t) \in \mathbb{R}^3$ for the i$^{\text{th}}$ object feature can be written as follows

$$S_i = [W(X, \tilde{\theta}_{c1}) - \hat{p}_{si}\Pi(X, \tilde{\theta}_{c2})]\theta_{si} \tag{2.27}$$

which can be further written as follows[7]

$$S_i = [W_{xi}(X, \theta_{si}) \quad - \hat{p}_{si}\Pi_{xi}(X, \theta_{si})]\tilde{\theta}_c \quad \forall i = 1, .., n \tag{2.28}$$

where $W_{xi}(\cdot) \in \mathbb{R}^{3\times 12}$, $\Pi_{xi}(\cdot) \in \mathbb{R}^{1\times 4}$, and $\tilde{\theta}_c \triangleq \begin{bmatrix} \theta_{c1}^T & \theta_{c2}^T \end{bmatrix}^T \in \mathbb{R}^{16}$.

In order to make the structure estimation error $\tilde{\theta}_s(t)$ go to zero, we seek to make the prediction error $\tilde{p}_s(t)$ given in (2.26) go to zero.

Auxiliary Prediction Error Formulation

[7]The reader is referred to [47] for the matrix property.

To further facilitate the development and to account for the unknown intrinsic and extrinsic camera parameters, both sides of (2.12) is multiplied with the term $\Pi_{xj}(\cdot)\theta_{c2}$ to obtain the following expression

$$p_{cj}\Pi_{xj}(\cdot)\theta_{c2} = W_{xj}(\cdot)\theta_{c1} \quad \forall j = 1, .., m. \tag{2.29}$$

The estimate form of (2.29) is written as follows

$$\hat{p}_{cj}\Pi_{xj}(\cdot)\hat{\theta}_{c2} = W_{xj}(\cdot)\hat{\theta}_{c1} \tag{2.30}$$

where $\hat{p}_{cj}(t) \in \mathbb{R}^3$ is the pixel estimate of the j$^{\text{th}}$ feature. After subtracting (2.30) from (2.29), and then adding and subtracting the term $\hat{p}_{cj}\Pi_{xj}\theta_{c2}$ to the left-hand-side results in the following expression

$$\tilde{p}_{cj} = \frac{1}{\Pi_{xj}(\cdot)\theta_{c2}}\left[W_{xj}(\cdot)\tilde{\theta}_{c1} - \hat{p}_{cj}\Pi_{xj}(\cdot)\tilde{\theta}_{c2}\right] \tag{2.31}$$

where $\tilde{p}_{cj}(t) \triangleq p_{cj} - \hat{p}_{cj} \in \mathbb{R}^3$ is the prediction error for the j$^{\text{th}}$ feature point $\forall j = 1, .., m$. Based on (2.31), the combined form of the prediction errors, denoted by $\tilde{p}_c \triangleq \begin{bmatrix}\tilde{p}_{c1}^T & \tilde{p}_{c2}^T & ... & \tilde{p}_{cm}^T\end{bmatrix}^T \in \mathbb{R}^{3m}$, can be written as follows

$$\tilde{p}_c = F\begin{bmatrix}W_x & \Pi_x\end{bmatrix}\begin{bmatrix}\tilde{\theta}_{c1}^T & \tilde{\theta}_{c2}^T\end{bmatrix}^T. \tag{2.32}$$

In (2.32), $\Pi_x(t) \in \mathbb{R}^{3m\times 4}$, and $W_x(\bar{X}) \in \mathbb{R}^{3m\times 12}$ are defined as follows

$$\begin{aligned}\Pi_x &\triangleq -\left[(\hat{p}_{c1}\Pi_{x1})^T (\hat{p}_{c2}\Pi_{x2})^T ... (\hat{p}_{cm}\Pi_{xm})^T\right]^T \\ W_x &\triangleq \left[W_{x1}(\bar{X})^T W_{x2}(\bar{X})^T ... W_{xm}(\bar{X})^T\right]^T\end{aligned} \tag{2.33}$$

and $F(t) \in \mathbb{R}^{3m\times 3m}$ is an auxiliary matrix defined as follows

$$F \triangleq \text{diag}\left\{\bar{\varphi}_1, \bar{\varphi}_1, \bar{\varphi}_1, ..., \bar{\varphi}_n, \bar{\varphi}_n, \bar{\varphi}_n\right\} \tag{2.34}$$

where $\bar{\varphi}_j \triangleq \frac{1}{\Pi_{xj}\theta_{c2}} \quad \forall j = 1, ..., m$. The expression given in (2.32) can be further simplied as follows

$$\tilde{p}_c = FW_c\tilde{\theta}_c \tag{2.35}$$

where $W_c(t) \in \mathbb{R}^{3m\times 16}$ is defined as follows

$$W_c \triangleq [W_x \;\; \Pi_x]. \tag{2.36}$$

To account for the unknown camera parameters, the following update law is designed [46]

$$\dot{\hat{\theta}}_c \triangleq \text{Proj}\left\{\alpha_c \Gamma_c W_c^T \tilde{p}_c\right\} \tag{2.37}$$

where $\text{Proj}\{\cdot\}$ ensures the positiveness of the term $\Pi_{xj}(\cdot)\hat{\theta}_{c2}(t)$ (see [48] for a detailed description) and $\alpha_c(t) \in \mathbb{R}$ is a positive function defined as follows

$$\alpha_c \triangleq 1 + \frac{1}{\bar{\varepsilon}_c}\bar{\rho}_c(\cdot) \tag{2.38}$$

where $\bar{\rho}_c(\cdot) \triangleq \max_j\left\{\rho_{cj}^2(\cdot)\right\} \in \mathbb{R}$ is a positive function and $\bar{\varepsilon}_c \triangleq \min_j\{\varepsilon_{cj}\} \in \mathbb{R}$ is a positive constant. In (2.37), $\Gamma_c(t) \in \mathbb{R}^{16\times 16}$ is the covariance matrix, designed as follows[8]

$$\frac{d}{dt}\left\{\Gamma_c^{-1}(t)\right\} = 2W_c^T W_c, \quad \Gamma_c(t_m^+) = \Gamma_c(t_0) = \eta_0 I_{16} \tag{2.39}$$

where $t_m \in \mathbb{R}^+$ is the time instant at which the minimum eigenvalue of $\Gamma_c(t)$ is less than or equal to η_1 (*i.e.*, the covariance matrix is reset each time when its minimum eigenvalue becomes less than η_1) and $\eta_0, \eta_1 \in \mathbb{R}$ are positive constants satisfying the inequality $\eta_0 > \eta_1$.

Remark 1 *It is to be noted that due to resetting, $\Gamma_c(t)$ is guaranteed to be positive definite for all $t \geq 0$. At the resetting time t_m, $\Gamma_c(t_m^+) = \Gamma_c(t_0) = \eta_0 I_{16}$; therefore, $\Gamma_c^{-1}(t_0) = \eta_0^{-1} I_{16}$ and between the discontinuities $\frac{d}{dt}\Gamma_c^{-1}(t) \geq 0$ (*i.e.*, $\Gamma_c^{-1}(t_2) - \Gamma_c^{-1}(t_1) \geq 0, \quad \forall t_2 \geq t_1 \geq 0$). Thus, it can be easily inferred that $\Gamma_c^{-1} \geq \eta_0^{-1} I_{16}$, $\forall t \geq 0$. Because of the resetting, $\Gamma_c(t)$ is always lower bounded by $\eta_1 I_{16}$, $\forall t \geq 0$; therefore, the following inequalities are always guaranteed [49]*

$$\eta_0 I_{16} \geq \Gamma_c(t) \geq \eta_1 I_{16}, \;\; \eta_1^{-1} I_{16} \geq \Gamma_c^{-1}(t) \geq \eta_0^{-1} I_{16}. \tag{2.40}$$

[8]Throughout the paper, I_q will be used to denote a $q \times q$ standard identity matrix.

Euclidean Structure Estimator

Based on the subsequent stability analysis, the following update law is designed to estimate the Euclidean coordinates of the unknown object features relative to $\mathcal{W}$

$$\dot{\hat{\theta}}_s \triangleq \text{Proj}\left\{\alpha \Gamma \bar{W}_s^T \tilde{p}_s\right\} \tag{2.41}$$

where $\text{Proj}\{\cdot\}$ ensures the positiveness of the term $\hat{\Pi}(\cdot)\hat{\theta}_{si}(t)$ (see [48] for a detailed description), and $\alpha(t) \in \mathbb{R}$ is a positive scalar function defined as follows

$$\alpha \triangleq 1 + \frac{1}{\bar{\varepsilon}_s} \bar{\rho}_s(\cdot) \tag{2.42}$$

where $\bar{\rho}_s(\cdot) \in \mathbb{R}$ is a positive function defined as

$$\bar{\rho}_s(\cdot) \triangleq \max_i \left\{\rho_{si}^2(\cdot)\right\} \tag{2.43}$$

and $\bar{\varepsilon}_s \in \mathbb{R}$ is a positive constant defined as follows

$$\bar{\varepsilon}_s \triangleq \min_i \{\varepsilon_{si}\}. \tag{2.44}$$

In (2.41), $\Gamma(t) \in \mathbb{R}^{4n \times 4n}$ is the least-squares estimation gain matrix, designed as follows

$$\frac{d}{dt}\left\{\Gamma^{-1}(t)\right\} = 2\bar{W}_s^T \bar{W}_s. \tag{2.45}$$

The Euclidean structure estimator given in (2.41) is run simultaneously with the adaptive update law given in (2.37). The latter updates the camera parameters for $\bar{W}_s(t)$ which is used in the structure estimator. See Fig. 2.2 for an illustration of the estimation technique.

Remark 2 *It should be noted that if* $\Gamma^{-1}(t_0)$ *is selected to be positive definite and symmetric then* $\Gamma(t_0)$ *is also positive definite and symmetric. Therefore, it follows that both* $\Gamma^{-1}(t)$ *and* $\Gamma(t)$ *are positive definite and symmetric. The following expression can be obtained from (2.45)*

$$\dot{\Gamma} = -2\Gamma \bar{W}_s^T \bar{W}_s \Gamma. \tag{2.46}$$

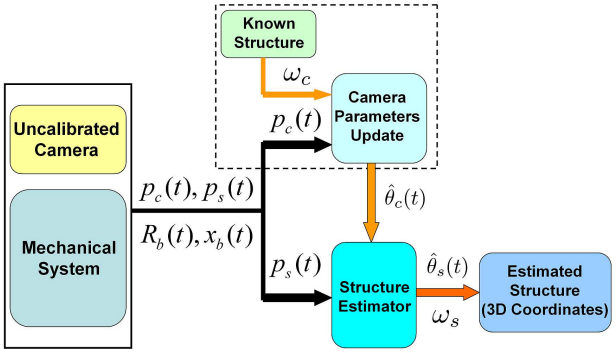

Figure 2.2 An illustration of the proposed 3D Euclidean coordinates estimation technique.

It can be easily seen from (2.46) that $\dot{\Gamma}(t)$ *is negative semidefinite; therefore,* $\Gamma(t)$ *is always constant or decreasing; hence, it follows that* $\Gamma(t)$ *is bounded (for more details, the reader is referred to [31]).*

Remark 3 *The projection algorithm utilized in (2.37), and (2.41) ensures that* $\hat{p}_{si}(t)$ *is bounded* $\forall i = 1, .., n$. *Furthermore, it satisfies the following inequalities (see [42] for a detailed description)*

$$-\tilde{\theta}_s \Gamma^{-1} Proj\{\tau_s\} \leq -\tilde{\theta}_s \Gamma^{-1} \tau_s \tag{2.47}$$

$$-\tilde{\theta}_c \Gamma_c^{-1} Proj\{\tau_c\} \leq -\tilde{\theta}_c \Gamma_c^{-1} \tau_c \tag{2.48}$$

where $\tau_s = \alpha \Gamma \bar{W}_s^T \tilde{p}_s$ *and* $\tau_c = \alpha_c \Gamma_c W_c^T \tilde{p}_c$.

Stability Analysis

Theorem 2 *The update law defined in (2.41) ensures that* $\left\|\tilde{\theta}_s(t)\right\| \to 0$ *as* $t \to +\infty$ *provided that the following PE condition [49] holds*

$$\gamma_1 I_{4n} \leq \int_{t_0}^{t_0+T} \bar{W}_s^T(\tau) \bar{W}_s(\tau) d\tau \leq \gamma_2 I_{4n}. \tag{2.49}$$

where γ_1, γ_2, $T \in \mathbb{R}$ *are positive constants.*

Proof. See Appendix D.

Remark 4 *The parameter vector $\hat{\theta}_{si}(t)$ provides a scaled estimate of the Euclidean coordinates of the object features relative to the world frame. Since the last element in the unknown constant parameter vector is equal to 1 as defined in (2.11), the scale factor can be computed as*

$$\lambda_i = \hat{\theta}_{si4} \tag{2.50}$$

where, $\lambda_i(t) \in \mathbb{R}$ is the scale factor for the i^{th} feature and $\hat{\theta}_{si4}(t) \in \mathbb{R}$ is the last entry of $\hat{\theta}_{si}(t)$. It should be noted that $\hat{\theta}_{si4}(t)$ is always nonzero which is guaranteed by the projection algorithm introduced in (2.37). The estimates of the Euclidean coordinates of the i^{th} feature can now be recovered as follows

$$\hat{\omega}_{sih} = \frac{1}{\lambda_i}\hat{\theta}_{sih} \tag{2.51}$$

where $\hat{\theta}_{sih}(t)\ \forall\ h = 1, 2, 3$, is the h^{th} element of the estimated parameter vector for i^{th} feature.

Simulation Results

A numerical simulation study was conducted to evaluate the performance of the proposed estimation algorithm using the Mathworks Simulink program. Six object features on the known object whose Euclidean coordinates relative to the world frame considered to be known *a priori*, were selected as follows

$$\begin{aligned} \omega_{c1} &= [0 \quad 1 \quad 1]^T \text{ m} & \omega_{c2} &= [0 \quad 0.5 \quad 1]^T \text{ m} \\ \omega_{c3} &= [0 \quad 0 \quad 1]^T \text{ m} & \omega_{c4} &= [1 \quad 1 \quad 1]^T \text{ m} \\ \omega_{c5} &= [1 \quad 0.5 \quad 1]^T \text{ m} & \omega_{c6} &= [1 \quad 0 \quad 1]^T \text{ m}. \end{aligned}$$

Eight non-planar object features on the unknown object, were selected to have the following 3D Euclidean coordinates relative to the world frame

$$\begin{aligned} \omega_{s1} &= [0.5 \quad 1 \quad 1]^T \text{ m} & \omega_{s2} &= [0.8 \quad 1 \quad 1.2]^T \text{ m} \\ \omega_{s3} &= [0.5 \quad 0.5 \quad 1.4]^T \text{ m} & \omega_{s4} &= [1.5 \quad 1 \quad 1.5]^T \text{ m} \\ \omega_{s5} &= [1.5 \quad 1.5 \quad 1.6]^T \text{ m} & \omega_{s6} &= [1 \quad 2 \quad 1.8]^T \text{ m} \\ \omega_{s7} &= [2 \quad 1 \quad 2]^T \text{ m} & \omega_{s8} &= [1 \quad 1 \quad 2.5]^T \text{ m}. \end{aligned}$$

The intrinsic calibration matrix and extrinsic parameters for a 640×480 camera were selected as follows

$$\begin{aligned} A &= \begin{bmatrix} 825 & 0 & 320 \\ 0 & 835 & 240 \\ 0 & 0 & 1 \end{bmatrix} \\ R_c &= I_3 \qquad x_c = [0.5 \quad 0 \quad 0.1]^T \text{ m}. \end{aligned}$$

The mechanical system was given the following translation vector $x_b(t)$, and angular rotation $q_b(t) \in \mathbb{R}^3$(yaw-pitch-roll about x-y-z axes)

$$\begin{aligned} x_b &= [0.1\cos(t) \quad 0.1\sin(t) \quad 0.1\sin(0.5t)]^T \quad \text{m} \\ q_b &= [0 \quad 0 \quad 0.1\sin(0.1t)]^T \quad \text{rad}. \end{aligned}$$

The measurable $R_b(t)$ was generated using $q_b(t)$. The initial condition for the vector $\hat{\theta}_s(t_0)$ was set to 250 for all its entries, and $\hat{\theta}_c(t_0)$ was set to 100 for all its entries. The estimator gains were selected based on trial-and-error as follows

$$\begin{aligned} \alpha_c &= 50, \qquad \Gamma_c^{-1}(t_0) = I_{16}\,; \quad \eta_0 = 1\,, \eta_1 = 0.002 \\ \alpha &= 300, \qquad \Gamma^{-1}(t_0) = 4000 I_{32}. \end{aligned}$$

Two different cases were examined using the above parameters. For case A, pixel measurements had no noise in them while in case B, the pixel coordinates were corrupted by 2% random noise (pixel errors not exceeding 5 pixels at any time). The estimates for the 3D Euclidean coordinates $\hat{\omega}_{si}(t)\, \forall i = 1, .., 8$ for the two cases are shown in Fig. 2.3 and Fig. 2.4, respectively. It can be seen from these figures that the proposed estimation technique provides good estimations for the structure, and the added noise has insignificant effect on the estimator. To further validate the estimation technique, seven lengths (Euclidean distances) were measured on the object. For instance "Length 1" is the distance from ω_{s1} to ω_{s2} on the object. The lengths

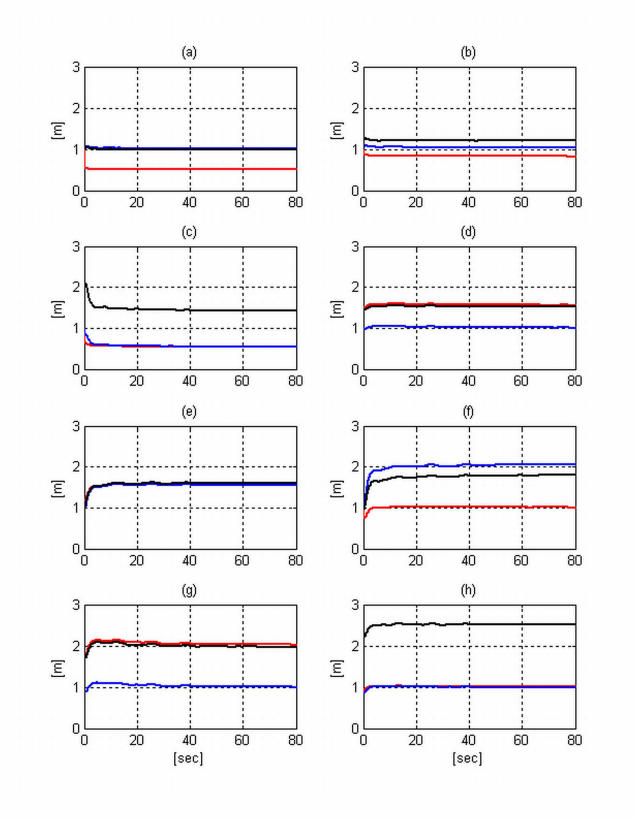

Figure 2.3 Simulation case A (without noise): Estimates of the 3D Euclidean coordinates $\hat{\omega}_{si}(t) \quad \forall i = 1, .., 8$ shown in (a)-(h)., respectively.

(in [cm]) were found to be

$$\text{Length } 1 = 36.06 \quad \text{Length } 2 = 61.64 \quad \text{Length } 3 = 112.20$$

$$\text{Length } 4 = 50.99 \quad \text{Length } 5 = 73.48 \quad \text{Length } 6 = 142.80$$

$$\text{Length } 7 = 111.80.$$

The results for the Euclidean distance estimation error for both the cases are shown in Fig. 2.5. The insets show the errors zoomed in for the last 20 seconds of the simulation. Again, it can be seen that the added noise plays an insignificant role, and the Euclidean distance estimation errors for all the lengths are well within 1 cm for the last 20 seconds. The simulation results in figures 2.3, 2.4, and 2.5 show that the proposed estimation technique can be used to recover the 3D Euclidean

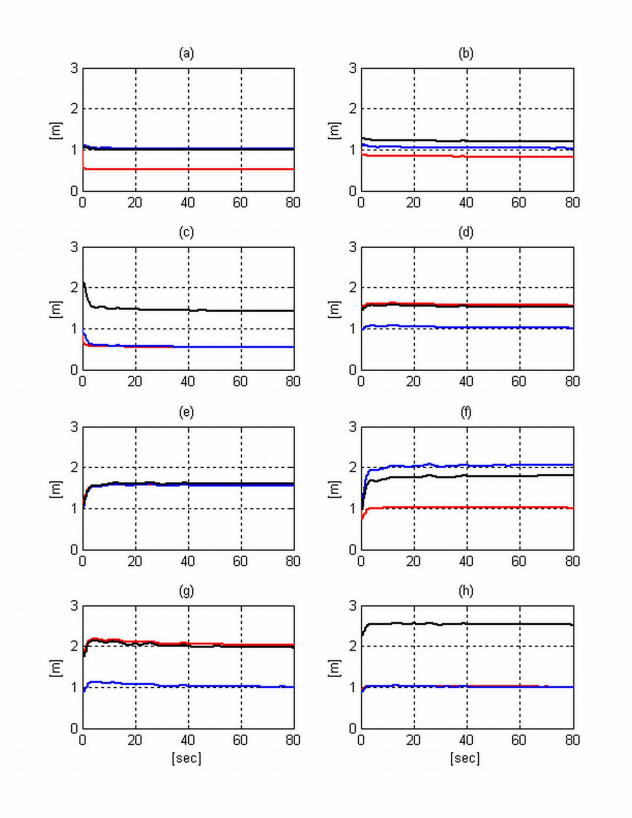

Figure 2.4 Simulation case B (with noise): Estimates of the 3D Euclidean coordinates $\hat{\omega}_{si}(t) \forall i = 1, .., 8$ shown in (a)-(h)., respectively.

coordinates of an object without having the knowledge of the camera's intrinsic or extrinsic calibration parameters.

Experimental Results

In this section, experimental results of the proposed estimation technique are discussed. In the experiment, a single object was considered with known 3D coordinates of six features and unknown 3D coordinates of another four features relative to the world frame. An uncalibrated monochrome CCD camera (Sony XC-ST50) was mounted on the end-effector of a Puma 560 robot manipulator (see Fig. 2.6). The end-effector of the robot was given a smooth closed trajectory along x, y, and z axes commanded by a PC running the QNX 6.2 operating system. A second PC, used for image processing and equipped with an Imagenation PXC200AF frame-grabber

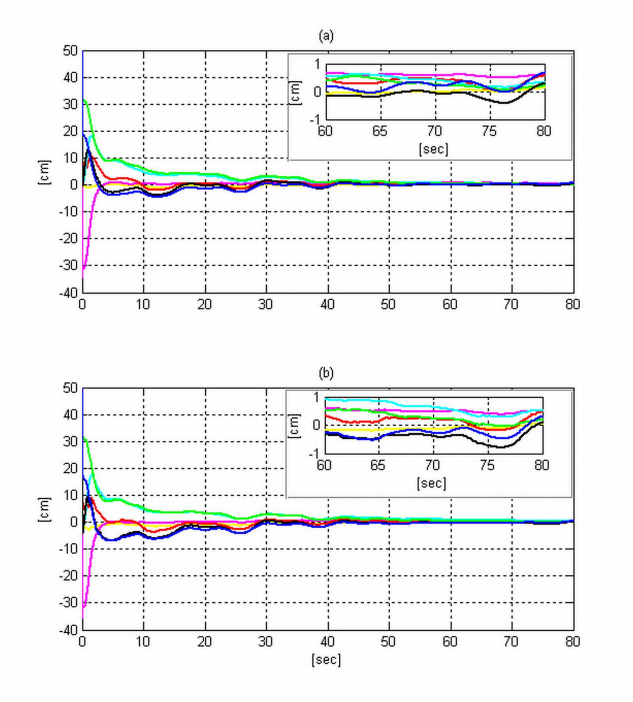

Figure 2.5 Euclidean distance estimation error: (a) without noise (b) in the presence of noise.

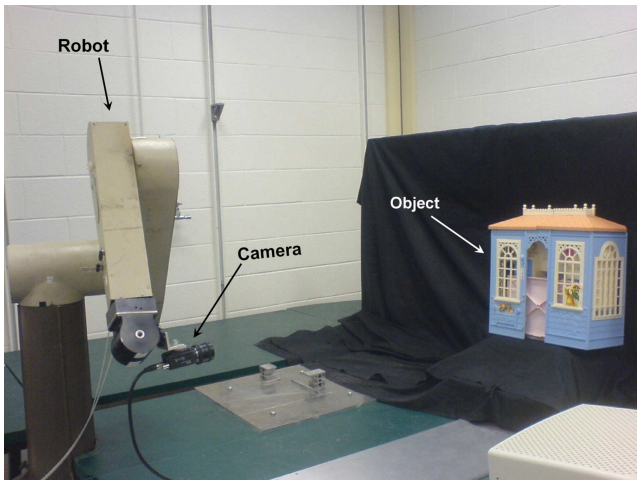

Figure 2.6 Experimental testbed with camera, robot and object.

board capable of acquiring images in real time (30 fps) over the PCI bus was interfaced with the camera. The robot control and vision systems were separated that required a synchronization between the two systems. Therefore, a 15 Hz digital signal was sent out to the image processing PC from the robot control PC to trigger the frame-grabber to acquire images. The same trigger signal was used to record the end-effector position of the robot relative to the world frame, in a file to be processed off-line later.

An implementation of the Kanade-Lucas-Tomasi feature tracking algorithm [35] available at [36] was used for tracking object features from one frame to another. The C++ implementation of the algorithm enabled the user to select object features manually and track them in the image sequence.

The proposed estimation algorithm was implemented off-line using Mathworks Simulink program using the data obtained from the vision tracking system and the robot control PC. Ten features were tracked on a stationary doll-house. A sample frame with the tracked features is shown in Fig. 2.7 where circle-markers represent four object features whose Euclidean coordinates are unknown and star-markers denote the other six object features with known Euclidean coordinates relative to the world frame. The true Euclidean distances between the object features with unknown

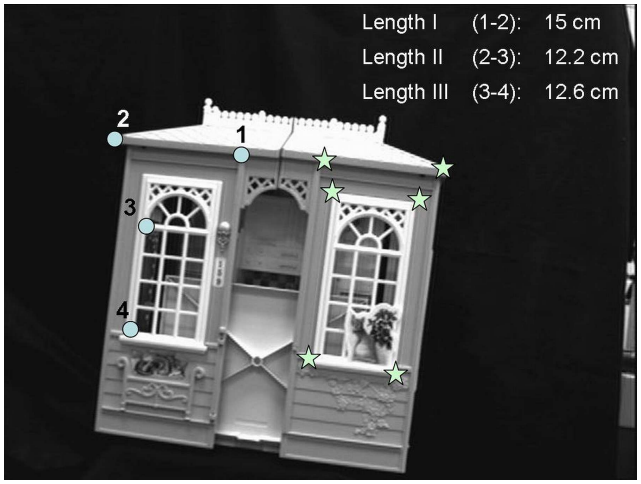

Figure 2.7 A frame from the doll-house image sequence with the tracked object features, and the true Euclidean distances between them.

3D coordinates relative to the world frame are shown in Fig. 1.13. The initial condition for the vector $\hat{\theta}_s(t_0)$ was set to 100 for all its entries, and $\hat{\theta}_c(t_0)$ was set to 20 for all its entries. The following estimator gains provided good performance

$$\begin{aligned} \alpha_c &= 50, \qquad \Gamma_c^{-1}(t_0) = I_{16}\,; \quad \eta_0 = 1\,, \eta_1 = 0.002 \\ \alpha &= 1000, \qquad \Gamma^{-1}(t_0) = 1000 I_{16}. \end{aligned}$$

Similar to the simulation section, the proposed estimation technique was verified by estimating the Euclidean distances between the object features whose 3D coordinates were unknown. The Euclidean distance estimation errors between representative features are shown in Fig. 2.8. The inset shows Euclidean distance estimation error zoomed in for the last 60 seconds. It can be seen that the proposed estimation technique gives good estimation of the Euclidean distances between the object features. One can conclude that a precise estimation of the 3D Euclidean coordinates is obtained of the object features without any knowledge of the camera's intrinsic and extrinsic calibration parameters.

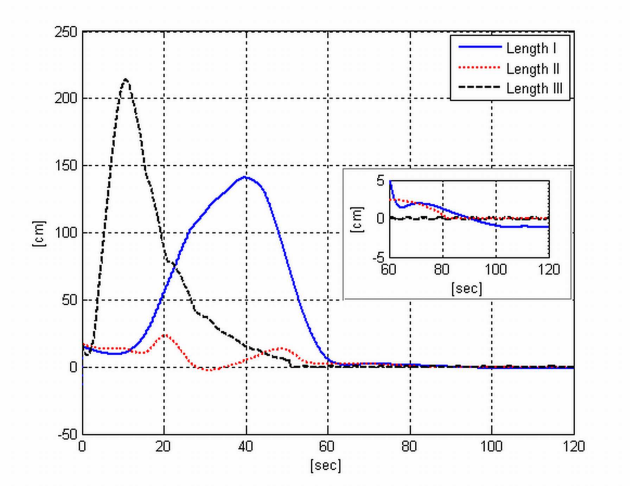

Figure 2.8 Experiment: Euclidean distance estimation error.

CHAPTER 3
RANGE IDENTIFICATION FOR NONLINEAR PARAMETERIZABLE PARACATADIOPTRIC SYSTEMS

Introduction

The problem of range identification, where the estimation of the unknown time-varying distance of the object from the camera along its optical axis, has received noteworthy attention over the last several years due to its significance in several applications such as autonomous vehicle navigation, aerial tracking, path planning, surveillance, etc. These applications require either the range or the 3D Euclidean coordinates of features of a moving or a static object to be recovered from their two-dimensional (2D) image sequence. The range estimation is usually done by mounting a camera on a moving vehicle such as a mobile robot or an unmanned aerial vehicle (UAV) which captures images of the static objects or features. However, the use of conventional (perspective) cameras pose restrictions for some applications because of their limited field-of-view (FOV).

One efficient way to enhance the FOV is to use mirrors (spherical, elliptical, hyperboloid, or paraboloid) in conjunction with conventional cameras, commonly known as catadioptric systems [50]. However, the use of curved mirrors reduce the resolution and distort the images to a large extent. As stated in [51], the distorted image mapping can be dealt with by using computer vision techniques, but the nonlinearity which is introduced in the transformation makes it difficult to recover 3D coordinates of the object features. Catadioptric systems that have a single effective viewpoint are known as central catadioptric systems, and are desirable because they allow for distortion-free reconstruction of panoramic images [52]. A paracatadioptric system is a special case of central catadioptric systems which employs a paraboloid mirror along with an orthographic lens. These systems are advantageous due to the fact

that the paraboloid constant of the mirror along with its physical size do not need to be determined during the calibration. Furthermore, mirror alignment requirements are relaxed which means that the mirror can be arbitrarily translated enabling the camera to zoom in on a part of the paraboloid mirror for higher resolution; however, with a reduced FOV [50].

In the past, many researchers have proposed various range identification techniques for perspective vision systems. Some of which have utilized the extended Kalman filter (EKF) [10], [12], [53]. However, EKF involves linearization of the nonlinear vision model and requires *a priori* knowledge of the noise distribution. To overcome the shortcomings of the linear model, many researchers focused on utilizing nonlinear system analysis and estimation tools to develop nonlinear observers to identify the range when the motion parameters were known [1], [17], [18], [19], [20], [39]. More recently, in [41], measurement of camera position was utilized to develop an adaptive estimator to recover the structure which was extended in [42] to recover the range.

Although, there have been several reports on range identification for perspective vision systems, very few results have been shown for range identification for catadioptric systems. In [54], Ma *et al.* proposed a range identification technique for paracatadioptric system based on a sequence of linear approximation-based observers. In [25], Gupta *et al.* designed a nonlinear observer to asymptotically identify the range for a paracatadioptric system. However, both of these reports assumed the focal point of the paraboloid mirror to be at its vertex. This assumption was recently relaxed in [51]. In the current work, we also base our development on a more practical approach that the focus of the paraboloid mirror is not at its vertex. In [52], an omnidirectional light projector was embedded in a paracatadioptric system, and the range was calculated by triangulation. In [51], Hu *et al.* developed a nonlinear estimator similar to [19] to identify the range for paracatadioptric systems where the motion parameters were assumed to be known, and it assumed that the object must

translate in at least one direction.

In this paper, we present a method to identify the range of a static object using a moving paracatadioptric system whose position is measurable. For many applications, position measurements are considerably less noisy than velocity measurements; hence, we are motivated to develop an estimator based on position measurements. The estimator is designed by first developing a geometric model along with a paracatadioptric projection model that relates an object feature with the paracatadioptric system mounted on a moving mechanical system. The novelty of this work lies in the compensation for nonlinear parameterization of the model which relates the projected pixel coordinates to the Euclidean coordinates of the object feature. It should be noted that contrary to [41], where the unknown terms appear linearly in the parameterized model for a perspective vision system, in the current work, the unknown parameters appear nonlinearly in the model for a paracatadioptric system. This fact makes it difficult to use a standard adaptive estimator or a gradient based estimator [55]. The estimator presented in this paper which facilitates range identification to the desired precision is based on a min-max optimization algorithm. We show that the developed estimator identifies the range and the 3D coordinates of the object feature upon the satisfaction of a Nonlinear Persistent Excitation (NLPE) condition and is robust to noise as demonstrated by the simulation results. The contributions of this paper are that: i) the developed estimator utilizes position measurements instead of velocity measurements, ii) is continuous, and iii) provides estimation of unknown parameters within a desired precision.

Model Development

Geometric Model

For the development of a geometric relationship between a moving paracatadioptric system and a stationary object, an orthogonal coordinate frame, denoted by $\mathcal{M}$, which is centered at the focal point of the moving paraboloid mirror whose Z-axis is

aligned with the optical axis of the camera, is defined (see Fig. 3.1). As shown in Fig. 3.1, an inertial coordinate frame, denoted by $\mathcal{W}$, and an orthogonal coordinate frame, denoted by $\mathcal{B}$, are defined. $\mathcal{F}$ denotes a static feature on a stationary object. Let the unknown 3D Euclidean coordinates of the object feature be denoted as the constant $\theta \in \mathbb{R}^3$ relative to the world frame $\mathcal{W}$ and $m(t) \in \mathbb{R}^3$ relative to $\mathcal{M}$ be defined as follows

$$m \triangleq [x \;\; y \;\; z]^T . \tag{3.1}$$

To relate the coordinate systems, let $R_b(t) \in SO(3)$ and $x_b(t) \in \mathbb{R}^3$ denote the

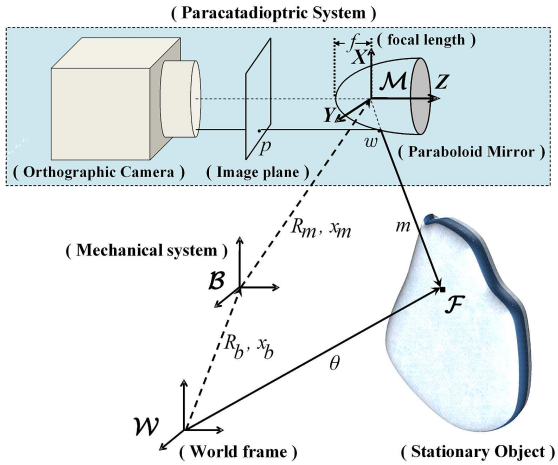

Figure 3.1 Geometric relationships between the stationary object, mechanical system, and the paracatadioptric system.

measurable rotation matrix and the translation vector, respectively, from $\mathcal{B}$ to $\mathcal{W}$ expressed in $\mathcal{W}$. Let $R_m \in SO(3)$ and $x_m \in \mathbb{R}^3$ be the known rotation matrix and the translation vector, respectively, from $\mathcal{M}$ to $\mathcal{B}$ expressed in $\mathcal{B}$.

Paracatadioptric System Projection Model

In a paracatadioptric system, a Euclidean point is projected onto a paraboloid mirror and is then reflected to an orthographic camera (see Fig. 3.1); thus, to facilitate the subsequent development, and to relate the geometric model to the vision system,

let the projection of the object feature on the surface of the paraboloid mirror with its focus at the origin be denoted by $w(t) \in \mathbb{R}^3$ relative to $\mathcal{M}$ and defined as follows

$$w \triangleq [u \ v \ q]^T . \tag{3.2}$$

The projection $w(t)$ can be expressed as follows [56]

$$w = \frac{2f}{\lambda} m = \frac{2f}{\lambda} [x \ y \ z]^T \tag{3.3}$$

where $f \in \mathbb{R}$ is the known focal length of the mirror and $\lambda(x, y, z) \in \mathbb{R}$ is the unknown nonlinear signal defined as follows

$$\lambda \triangleq -z + \sqrt{x^2 + y^2 + z^2}. \tag{3.4}$$

It is worthwhile to mention that the use of a paracatadioptric system results in an orthographic projection from the paraboloid mirror to the image plane. In other words, the reflected rays are parallel to the optical axis; thus, the distance from the mirror to the image plane is irrelevant. After utilizing (3.2) and (3.3), the projection can be expressed as follows

$$\begin{bmatrix} u \\ v \end{bmatrix} = \frac{2f}{\lambda} \begin{bmatrix} x \\ y \end{bmatrix}. \tag{3.5}$$

However, when measured from a CCD chip as in any practical case, $[u, v]^T$ is transformed as follows [57]

$$p \triangleq \begin{bmatrix} u' \\ v' \end{bmatrix} = K \begin{bmatrix} u \\ v \end{bmatrix} + C \tag{3.6}$$

where $p(t) \in \mathbb{R}^2$ are the measured pixel coordinates on the image plane, $K \in \mathbb{R}^{2\times 2}$ and $C \in \mathbb{R}^2$ are defined as follows

$$K \triangleq \begin{bmatrix} a_1 & a_2 \\ 0 & a_1^{-1} \end{bmatrix} \qquad C \triangleq \begin{bmatrix} c_x \\ c_y \end{bmatrix} \tag{3.7}$$

where $a_1^2, a_2 \in \mathbb{R}$ are the aspect ratio and the skew factor, respectively, and C is the image center. Since a central catadioptric camera can be calibrated using a single image of three lines [57], [58], we assume the camera to be calibrated. It is clear from

(3.6) that the coordinates in the mirror frame, $u(t)$ and $v(t)$, can be obtained from the measured pixel coordinates as follows

$$[u \;\; v]^T = K^{-1}(p - C). \tag{3.8}$$

Also, since the paraboloid mirror is rotationally symmetric, $q(\cdot) \in \mathbb{R}$ can be computed from $u(t)$ and $v(t)$ as follows [51]

$$q = \frac{u^2 + v^2}{4f} - f. \tag{3.9}$$

Assumption 1 *It is assumed that the object feature is not on the optical axis* i.e., $x(t), y(t) \neq 0$ *simultaneously and thus,* $\lambda(\cdot) \neq 0$.

Nonlinear Parameterization of the Model

In this section, the parameterization of the nonlinear function $q(\cdot)$ is presented after relating it to the unknown 3D Euclidean coordinates of the object feature. From Fig. 3.1, $m(t)$ can be written as follows [41]

$$m = R_m^T \left[R_b^T (\theta - x_b) - x_m \right]. \tag{3.10}$$

After utilizing (3.1), the 3D coordinates of the object feature relative to $\mathcal{M}$ can be expressed as follows

$$x = R_{m1}^T \left[R_b^T (\theta - x_b) - x_m \right] \tag{3.11}$$

$$y = R_{m2}^T \left[R_b^T (\theta - x_b) - x_m \right] \tag{3.12}$$

$$z = R_{m3}^T \left[R_b^T (\theta - x_b) - x_m \right] \tag{3.13}$$

where $R_{mi}^T \in \mathbb{R}^{1\times 3}$ is the i^{th} row of R_m^T, and $z(t)$ is the range of the object feature. After substituting (3.5) into the nonlinear model given in (3.9), $q(\cdot)$ is nonlinearly parameterized (NLP) as follows

$$q(\theta, R_m, x_m, R_b, x_b, f) = \frac{\left(\frac{2f}{\lambda}x\right)^2 + \left(\frac{2f}{\lambda}y\right)^2}{4f} - f. \tag{3.14}$$

In the subsequent analysis, $q\left(\theta, R_m, x_m, R_b, x_b, f\right)$ is replaced by $q(\theta, \Pi)$ where $\Pi(\cdot) \in \mathbb{R}^{n_1 \times n_2}$ with n_1 and n_2 being integers, contains the combinations of known and measurable quantities (*i.e.*, f, R_m, x_m, $R_b(t)$, and $x_b(t)$).

Remark 1 *It can be seen from (3.4), (3.9), and (3.11)- (3.13) that θ appears nonlinearly in $q(\cdot)$; thus, it is not possible to give an exact expression for the function $\Pi(\cdot)$. Specifically, $\Pi(\cdot)$ is a shorthand notation for $\Pi(f, R_m, x_m, R_b(t), x_b(t))$.*

Assumption 2 *The unknown parameter vector θ is assumed to belong to a known hypercube $\Theta \subset \mathbb{R}^3$. In other words, the 3D coordinates of the object feature relative to $\mathcal{W}$ are assumed to lie within their known minimum and maximum values.*

Assumption 3 *For any $\Pi(\cdot)$, the function $q(\cdot)$ is either concave or convex on a simplex*[9] *Θ_s in $\mathbb{R}^3$ such that $\Theta_s \supset \Theta$ (see Fig. 3.2).*

Assumption 4 *The function $\Pi(t)$ is bounded, continuous function of its arguments, and is Lipschitz in t such that*

$$\|\Pi(t_1) - \Pi(t_2)\| \leq L_1 |t_1 - t_2| \qquad \forall t_1, t_2 \in \mathbb{R}^+ \tag{3.15}$$

where $L_1 \in \mathbb{R}^+$ is the Lipschitz constant.

Assumption 5 *$q(\theta_0, \Pi)$ is Lipschitz with respect to its arguments such that*

$$|q(\theta_0 + \Delta\theta_0, \Pi + \Delta\Pi) - q(\theta_0, \Pi)| \leq L_2(\|\Delta\Pi\| + \|\Delta\theta_0\|) \tag{3.16}$$

where $L_2 \in \mathbb{R}^+$ is the Lipschitz constant, $\Delta\Pi = \Pi(t_1) - \Pi(t_2)$, and $\Delta\theta_0 = \theta_0(t_1) - \theta_0(t_2)$.

Definition 1 *A function $H(\varsigma)$ is said to be convex on Θ if it satisfies the following inequality*

$$\begin{aligned} H\left(\sigma\varsigma_1 + (1-\sigma)\,\varsigma_2\right) \;&\leq\; \sigma H\left(\varsigma_1\right) + (1-\sigma)\, H\left(\varsigma_2\right) \\ &\qquad \forall \varsigma_1, \varsigma_2 \in \Theta \end{aligned} \tag{3.17}$$

[9] A simplex in $\mathbb{R}^n$ is a convex polyhedron having exactly $n+1$ vertices.

and concave if it satisfies the following inequality

$$H\left(\sigma\varsigma_1 + (1-\sigma)\,\varsigma_2\right) \;\geq\; \sigma H\left(\varsigma_1\right) + (1-\sigma)\,H\left(\varsigma_2\right) \qquad \forall \varsigma_1, \varsigma_2 \in \Theta \tag{3.18}$$

where $0 \leq \sigma \leq 1$.

Remark 2 *It should be noted that the Assumptions 2 and 3 essentially characterize the nature of the nonlinear parameterization, and the convexity or concavity of the function* $q(\cdot)$ *is required in a region* Θ_s *which is larger than the hypercube* Θ. *Also, since an estimation problem for a practical moving paracatadioptric system is considered in this paper, we assume that the measurable position signals are bounded as well as its velocity is bounded. The boundedness of the position signals in other words mean that the function* $\Pi(\cdot)$ *is bounded.*

Remark 3 *In Appendix L, we show how Assumptions 4 and 5 can be replaced by a simpler condition on the differentiability of* $q(\cdot)$ *for the estimation problem.*

Remark 4 *Assumptions 4 and 5 are related to the boundedness of the motion of the mechatronic platform (*i.e., *a robot manipulator, UAV, or a mobile robot, etc.) to which the omnidirectional camera is attached. Also, The definition of convexity and concavity are provided in Definition 1. As noted in [59], for an affine function, we always have equality in (3.17) and (3.18), respectively. Therefore all affine (and therefore also linear) functions are both convex and concave. Conversely, any function that is convex and concave is affine. In Assumption 3, it is claimed that for any* $\Pi(\cdot)$, $q(\cdot)$ *is either convex or concave. Thus, Assumption 3 is utilized to exclude affine (and also linear) functions.*

Remark 5 *The hypercube* Θ *can be found using the minimum and the maximum values of* θ. *The vertices of the simplex* Θ_s, *denoted by* $\theta_{s1}, \theta_{s2}, \theta_{s3}, \theta_{s4} \in \mathbb{R}^3$, *can be found by first inscribing* Θ *in a 3-dimensional sphere and then inscribing this sphere inside a 4-dimensional polyhedron [55], [60].*

It should be noted that in (3.11)-(3.13), θ (*i.e*, the constant 3D coordinates of the object feature relative to $\mathcal{W}$) is the only unknown vector, and if we estimate this we can then obtain an estimation of the 3D coordinates of the object feature relative to $\mathcal{M}$ as follows

$$\hat{x} = R_{m1}^T[R_b^T(\hat{\theta} - x_b) - x_m] \tag{3.19}$$

$$\hat{y} = R_{m2}^T[R_b^T(\hat{\theta} - x_b) - x_m] \tag{3.20}$$

$$\hat{z} = R_{m3}^T[R_b^T(\hat{\theta} - x_b) - x_m] \tag{3.21}$$

where $\hat{x}(t), \hat{y}(t) \in \mathbb{R}$ are the estimates of $x(t)$ and $y(t)$, respectively, $\hat{z}(t) \in \mathbb{R}$ is the estimate of the corresponding range $z(t)$, and $\hat{\theta}(t) \in \mathbb{R}^3$ is the estimate of θ.

Remark 6 *It is worthwhile to mention that the range identification precision depends on the precision at which the constant unknown parameter vector θ is estimated. The estimated range, $\hat{z}(t)$, further depends upon the noise in the measurable position signals $R_b(t)$ and $x_b(t)$, and the error in the constant camera calibration parameters R_m and x_m. The effect of noise in these signals has been demonstrated later in the simulation section.*

Range Estimation

In this section, an estimator for the unknown constant parameter vector θ which appears nonlinearly in the model given in (3.14) is presented. There are very few researchers who have addressed adaptive control or estimation for NLP systems [55], [61], [62], [63]. Parameter convergence in NLP systems was addressed in [64]. As pointed out in [55], the gradient algorithm employed in [61], [62], [63] are not only inadequate but can also lead to instability for general NLP systems. In this work, we design an adaptive estimator that facilitates the identification of range within a desired precision based on the min-max algorithm developed in [55]. The maximization is that of a tuning function over all the possible values of the nonlinear parameters,

and the minimization is over all the possible sensitivity functions that can be used in the adaptive law. The sensitivity function which differs from the gradient depending upon the sign of a tuning error is incorporated in the adaptive law. The stability analysis ensures that the use of the tuning function along with the adaptive law has globally bounded error signals, and upon the satisfaction of an NLPE condition similar to [64], the parameter estimation follows; hence, the identification of range.

Estimator Design

To facilitate the estimator design, the estimate of (3.14) is defined as follows

$$\hat{q} \triangleq \frac{\left(\frac{2f}{\hat{\lambda}}\hat{x}\right)^2 + \left(\frac{2f}{\hat{\lambda}}\hat{y}\right)^2}{4f} - f \tag{3.22}$$

where $\hat{q}(\cdot) \in \mathbb{R}$ denotes $q(\hat{\theta})$, $\hat{\lambda}(\hat{x}, \hat{y}, \hat{z}) \in \mathbb{R}$ is the estimate of $\lambda(\cdot)$, and is defined as follows

$$\hat{\lambda} \triangleq -\hat{z} + \sqrt{\hat{x}^2 + \hat{y}^2 + \hat{z}^2}. \tag{3.23}$$

To further facilitate the development, we define a filter signal $q_f(t) \in \mathbb{R}$ as follows

$$\dot{q}_f \triangleq -\alpha q_f + q\,; \qquad q_f(0) \triangleq 0 \tag{3.24}$$

where $\alpha \in \mathbb{R}^+$. The estimate of (3.24) is designed as follows

$$\dot{\hat{q}}_f = -\alpha\left(\hat{q}_f - \varepsilon \text{sat}(r)\right) + \hat{q} - a^* \text{sat}(r) \tag{3.25}$$

where $\hat{q}_f(t)$, $\dot{\hat{q}}_f\ (t) \in \mathbb{R}$ are the estimates of $q_f(t)$, and $\dot{q}_f(t)$, respectively, $\varepsilon \in \mathbb{R}^+$ is the desired precision, $a^*(t)$ is the tuning function obtained from the subsequently presented min-max optimization problem, and $r(t) \in \mathbb{R}$ is defined as follows

$$r \triangleq \frac{\tilde{q}_f}{\varepsilon} \tag{3.26}$$

where the filter error $\tilde{q}_f(t) \in \mathbb{R}$ is defined as follows

$$\tilde{q}_f \triangleq \hat{q}_f - q_f. \tag{3.27}$$

Also, in (3.25), $\text{sat}(r)$ is a saturation function given as follows

$$\text{sat}(r) = \begin{cases} +1 & \text{if } r \geq 1 \\ r & \text{if } |r| < 1 \\ -1 & \text{if } r \leq -1. \end{cases} \tag{3.28}$$

To proceed with the development, we define a tuning error $\tilde{q}_{f\varepsilon}(t) \in \mathbb{R}$ as follows

$$\tilde{q}_{f\varepsilon} \triangleq \tilde{q}_f - \varepsilon \text{sat}(r). \tag{3.29}$$

After taking the time derivative of (3.27), the following expression can be written

$$\dot{\tilde{q}}_f = -\alpha \tilde{q}_{f\varepsilon} + \hat{q} - q - a^* \text{sat}(r) \tag{3.30}$$

where (3.24), (3.25), and (3.29) were utilized.

Remark 7 *It should be noted that the inclusion of the tuning error $\tilde{q}_{f\varepsilon}(t)$ provides the following expressions*

$$\begin{aligned} \tilde{q}_{f\varepsilon} &= 0 \qquad \textit{when } |\tilde{q}_f| \leq \varepsilon \\ \dot{\tilde{q}}_{f\varepsilon} &= \dot{\tilde{q}}_f \qquad \textit{when } |\tilde{q}_f| > \varepsilon. \end{aligned}$$

This remark is utilized later in the stability analysis.

Based on the stability analysis an estimator $\dot{\hat{\theta}}(t) \in \mathbb{R}^3$ is designed with a projection strategy which facilitates the estimation of θ as follows

$$\dot{\hat{\theta}} = \text{Proj}\{-\tilde{q}_{f\varepsilon} \phi^*\} \tag{3.31}$$

where $\phi^*(t) \in \mathbb{R}^3$ is the sensitivity function. The projection strategy $\text{Proj}\{\cdot\}$ in (3.31) ensures that $\hat{\theta}(t)$ always belongs to the hypercube Θ. The strategy is as follows

$$\hat{\theta}_j = \begin{cases} \hat{\theta}_j & \text{if } \hat{\theta}_j \in [\theta_{j,\min}, \theta_{j,\max}] \\ \theta_{j,\min} & \text{if } \hat{\theta}_j < \theta_{j,\min} \\ \theta_{j,\max} & \text{if } \hat{\theta}_j > \theta_{j,\max} \end{cases} \tag{3.32}$$

where the subscript j denotes the j^{th} element of the corresponding vector $\forall j = 1, 2, 3$, and $\theta_{j,\min}, \theta_{j,\max} \in \mathbb{R}$ are the minimum and maximum values of the j^{th} component of θ, respectively.

Similar to [55], the solutions for $\phi^*(t)$ and $a^*(t)$ are obtained from a min-max optimization problem of the following form

$$a^* = \min_{\phi \in \mathbb{R}^3} \max_{\theta \in \Theta_s} J(\phi, \theta) \tag{3.33}$$

$$\phi^* = \arg \min_{\phi \in \mathbb{R}^3} \max_{\theta \in \Theta_s} J(\phi, \theta) \tag{3.34}$$

where the performance index $J(\cdot) \in \mathbb{R}$ is given by the following expression

$$J(\cdot) = \text{sat}(r) \left[\hat{q} - q - \tilde{\theta}^T \phi \right] \tag{3.35}$$

where $\tilde{\theta}(t) \in \mathbb{R}^3$ is the parameter estimation error defined as follows

$$\tilde{\theta} \triangleq \hat{\theta} - \theta. \tag{3.36}$$

The solutions of (3.33) and (3.34) are given as follows[10]

a) when $\tilde{q}_f < 0$

$$a^* = \begin{cases} 0 & \text{if } q \text{ is concave on } \Theta_s \\ A_1 & \text{if } q \text{ is convex on } \Theta_s \end{cases} \tag{3.37}$$

$$\phi^* = \begin{cases} \nabla q(\hat{\theta}) & \text{if } q \text{ is concave on } \Theta_s \\ A_2 & \text{if } q \text{ is convex on } \Theta_s \end{cases} \tag{3.38}$$

b) when $\tilde{q}_f \geq 0$

$$a^* = \begin{cases} A_1 & \text{if } q \text{ is concave on } \Theta_s \\ 0 & \text{if } q \text{ is convex on } \Theta_s \end{cases} \tag{3.39}$$

$$\phi^* = \begin{cases} A_2 & \text{if } q \text{ is concave on } \Theta_s \\ \nabla q(\hat{\theta}) & \text{if } q \text{ is convex on } \Theta_s \end{cases} . \tag{3.40}$$

In (3.37)-(3.40), $A(t) \in \mathbb{R}^4$ is given as follows

$$A = [A_1 \; A_2]^T = G^{-1} b \tag{3.41}$$

[10]The reader is referred to [55] for the proof of the solutions.

where $A_1(t) \in \mathbb{R}$, and $A_2(t) \in \mathbb{R}^3$, $G(t) \in \mathbb{R}^{4\times 4}$ is given as follows

$$G = \begin{bmatrix} -1 & \beta(\hat{\theta} - \theta_{s1})^T \\ -1 & \beta(\hat{\theta} - \theta_{s2})^T \\ -1 & \beta(\hat{\theta} - \theta_{s3})^T \\ -1 & \beta(\hat{\theta} - \theta_{s4})^T \end{bmatrix} \tag{3.42}$$

and $b(t) \in \mathbb{R}^4$ is given as follows

$$b = \begin{bmatrix} \beta\left(\hat{q} - q_{s1}\right) \\ \beta\left(\hat{q} - q_{s2}\right) \\ \beta\left(\hat{q} - q_{s3}\right) \\ \beta\left(\hat{q} - q_{s4}\right) \end{bmatrix} \tag{3.43}$$

where $\beta(\Pi) \in \mathbb{R}$ is defined as follows

$$\beta \;=\; \begin{cases} 1 & \text{if } q \text{ is convex on } \Theta_s \\ -1 & \text{if } q \text{ is concave on } \Theta_s. \end{cases} \tag{3.44}$$

In (3.43), $g_{sh} \triangleq q(\theta_{sh}, \Pi)\, \forall h = 1, 2, 3, 4$. As mentioned earlier in Remark 5, θ_{sh} are the vertices of the simplex Θ_s. In (3.38) and (3.40), $\nabla q(\hat{\theta}) \in \mathbb{R}^3$ is the gradient function given as follows

$$\nabla q(\hat{\theta}) = \left(\partial q / \partial \theta\right)|_{\theta=\hat{\theta}}. \tag{3.45}$$

It is evident that the estimate of the constant 3D coordinates of the object feature relative to the world frame (*i.e.*, $\hat{\theta}(t)$) can be used to obtain the estimates of all its 3D coordinates relative to the vision system including the range (*i.e.*, $\hat{z}(t)$) from (3.19)-(3.21).

Remark 8 *It should be noted that the inclusion of the tuning error $\tilde{q}_{f\varepsilon}(t)$ with the saturation function sat(r) ensures that the estimator is continuous even if a discontinuous solution of the min-max algorithm is obtained (see [55] for more detailed description).*

Remark 9 *It should be noted that $\hat{\theta}(t)$ is bounded because of the projection strategy in (3.32); thus, $\phi^*(t)$ can be upper bounded as follows*

$$\|\phi^*(t)\| \leq L_\phi \qquad \forall t \geq t_0 \tag{3.46}$$

where $L_\phi \in \mathbb{R}^+$.

Remark 10 *We note that the tuning function $a(t)$, the sensitivity function, and the matrices $G(t)$ and $b(t)$ are similar to the corresponding functions defined in [55] and [64]. The novelty in the proposed work lies in the fact that we have applied a modified version of [55] and [64] for nonlinear parameter estimation application (*i.e.*, range identification using paracatadioptic systems). The work presented in [55] deals with the control of a nonlinearly parameterized system while parameter convergence of a nonlinearly parameterized system is presented in [64]. In the current paper, we modify the technique given in [64] for nonlinearly parameterized parameter estimation which facilitates the range identification for a paracatadioptric system. This modification is accomplished through the introduction of a filtering scheme which is given in (3.24).*

Stability Analysis

Theorem 3 *The adaptive update law given in (3.31) along with the solutions of $a^*(t)$ and $\phi^*(t)$ given in (3.37)-(3.40) ensures that $\tilde{q}_{f\varepsilon}(t) \in \mathcal{L}_2 \cap \mathcal{L}_\infty$; hence, the stability of the estimator, and the global boundedness of the overall adaptive system are ensured.*

Proof. See Appendix G.

Theorem 4 *The developed estimation technique ensures that $\|\tilde{\theta}(t)\| \leq \sqrt{\gamma}$ as $t \to \infty$ provided the following NLPE condition holds*

$$\beta(\Pi(t_2)) \left(q(\hat{\theta}(t_1), \Pi(t_2)) - q(\theta, \Pi(t_2)) \right) \geq \varepsilon_u \left\| \hat{\theta}(t_1) - \theta \right\| \tag{3.47}$$

where

$$\gamma = \frac{8\varepsilon c_1}{\varepsilon_u^2} \quad ; \qquad c_1 = 4L_1L_2 + 2L_2L_\phi + L_\phi^2, \tag{3.48}$$

$t_2 \in [t_1, t_1 + T_0]$, $t_1 > t_0$, *and* $T_0, \varepsilon_u \in \mathbb{R}^+$.

Proof. See Appendix H.

Remark 11 *From the definition of γ in (3.48), it follows that γ can be made smaller by choosing smaller ε. As the desired precision $\varepsilon \to 0$, then $\gamma \to 0$; thus, the parameter estimation error $\|\tilde{\theta}(t)\| \to 0$.*

Remark 12 *As pointed out in [64], it is difficult to check if the NLPE condition given in (3.47) can be satisfied in a general nonlinear system. To ensure parameter convergence,* $\Pi(\cdot)$ *must be such that one of the following occurs at least at one time instant* $t_2 \in [t_1, t_1 + T]$*: a) For the given* $\tilde{\theta}(t)$*,* $\Pi(\cdot)$ *must change in such a way that the sign of* $\hat{q}(\cdot) - q(\cdot)$ *is reversed, while keeping the convexity/concavity of* $q(\cdot)$ *the same or, b) for the given* $\tilde{\theta}(t)$*,* $\Pi(\cdot)$*, must reverse the convexity/concavity of* $q(\cdot)$*, while preserving the sign of* $\hat{q}(\cdot) - q(\cdot)$*. The reader is referred to [64] for a detailed analysis. It should be noted that the parameter convergence shown in the subsequently presented simulation results seems to indicate that the NLPE condition for the particular problem attacked in this paper was met.*

Simulation Results

A detailed simulation study was conducted to evaluate the performance of the proposed estimation technique using the Mathworks Simulink program. The translation vector $x_b(t)$, and angular rotation $q_b(t) \in \mathbb{R}^3$ (yaw-pitch-roll about x-y-z axes) to the mechanical system were given as follows

$$\begin{aligned} x_b &= [\sin(\pi t) \;\; 2\cos(\pi t) \;\; \sin(2\pi t)]^T \quad [\text{m}] \\ q_b &= [0 \;\; 0 \;\; 0.2\cos(\pi t)]^T \quad [\text{rad}]. \end{aligned} \tag{3.49}$$

The measurable signal $R_b(t)$ was generated using $q_b(t)$. The 3D Euclidean coordinates of an object feature relative to the world frame, θ, was taken as follows

$$\theta = [1 \;\; 2 \;\; 2]^T \quad [\text{m}] \tag{3.50}$$

along with the following maximum and minimum values

$$\theta_{max} = [4 \;\; 4 \;\; 4]^T \quad [\text{m}]\,; \quad \theta_{min} = [0 \;\; 0 \;\; 0]^T \quad [\text{m}]. \tag{3.51}$$

The calibration parameters were set as $a_1 = 1$, $a_2 = 0$, and $C = [0 \;\; 0]^T$. The rotation matrix R_m, and the translation vector x_m of the paracatadioptric system relative to

its mounting frame were selected as follows

$$R_m = I_3 \qquad x_m = [0 \;\; 0 \;\; 0.1]^T \quad [\text{m}]. \tag{3.52}$$

where $I_3 \in \mathbb{R}^{3\times 3}$ denotes a standard identity matrix. θ_{max}, and θ_{min} given in (3.51) were utilized to find the vertices of the hypercube Θ which is a cube in this case with its 8 vertices at $[0 \;\; 0 \;\; 0]^T$, $[0 \;\; 4 \;\; 0]^T$, $[0 \;\; 4 \;\; 4]^T$, $[0 \;\; 0 \;\; 4]^T$, $[4 \;\; 0 \;\; 0]^T$, $[4 \;\; 0 \;\; 4]^T$, $[4 \;\; 4 \;\; 4]^T$, and $[4 \;\; 4 \;\; 0]^T$. Hence, a tetrahedron simplex Θ_s, enclosing Θ was constructed as shown in Fig. 3.2 whose vertices were given as follows

$$\begin{aligned} \theta_{s1} &= [0 \;\; 0 \;\; 0]^T \qquad \theta_{s3} = [16 \;\; 0 \;\; 0]^T \\ \theta_{s2} &= [0 \;\; 0 \;\; 8]^T \qquad \theta_{s4} = [0 \;\; 16 \;\; 0]^T. \end{aligned}$$

Definition 1 was utilized to determine the concavity/convexity of the function $q(\cdot)$ on Θ_s. Initializing the estimator as $\hat{\theta}(t_0) = [0.5 \;\; 1 \;\; 1]^T$ (*i.e.*, 50% of the true values), and setting $f = 0.5$ along with the simulation parameters given in (3.49)-(3.50) and (3.52), gave the following initial values

$$z(t_0) = 1.9 \quad [\text{m}] \qquad \hat{z}(t_0) = 0.9 \quad [\text{m}].$$

The parameter α was set as $\alpha = 5$, and ε was selected as $\varepsilon = 0.001$ to make the tuning error $\tilde{q}_{f\varepsilon}(t)$ introduced in (3.29) very close to $\tilde{q}_f(t)$ so that a high precision for the estimation is obtained.

Two different cases were considered in the simulation study without changing any of the above mentioned parameters: case 1 was without any noise and case 2 was with additive-white-Gaussian-noise (AWGN) injected into the measured coordinates $u(t)$ and $v(t)$ using the awgn() function of Matlab. A constant signal-to-noise ratio (SNR) of 20 was maintained. It should be noted that injection of noise into $u(t)$ and $v(t)$ induces noise into $q(\theta, \Pi)$; hence, noise in any measurable signal contained in $\Pi(\cdot)$ is considered.

Fig. 3.3 shows $\hat{\theta}(t)$, the estimates of the 3D Euclidean coordinates of the object feature relative to the world frame, for case 1. Range estimation error ($i.e., z(t) - \hat{z}(t)$)

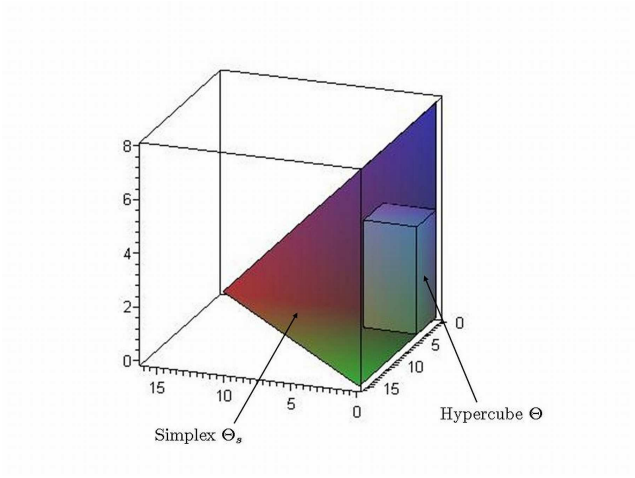

Figure 3.2 Simplex Θ_s, and hypercube Θ.

for case 1 is shown in Fig. 3.4. It can be seen from these Figs. that the developed estimation technique provides an accurate estimation of the range with an accurate estimate of the 3D coordinates of the object feature relative to the world frame. Figs. 3.5 and 3.6 show $\hat{\theta}(t)$ and the range estimation error, respectively in the presence of noise (*i.e.*, case 2). It can be inferred from these Figs. that the proposed range estimation technique is robust to noisy measurements and provides good estimates for the constant 3D coordinates of the object feature relative to the world frame along with an estimate of its range. It is worthwhile to note that $\hat{\theta}(t)$ can be used to obtain other 3D coordinates of the object feature relative to $\mathcal{M}$, $\hat{x}(t)$, $\hat{y}(t)$ from (3.19) and (3.20), respectively.

Remark 13 *The NLPE condition, given in (3.47), guarantees the parameter but it is not clear what role the NLPE condition plays in the rate of convergence. Furthermore, we note that the simulation results indicate that the constant parameter α, defined in (3.24), can also be tuned to affect the rate of convergence at the cost of estimation accuracy. In this paper, we primarily focus on the architecture and the technique to identify the range for a paracatadioptric system. This technique can be further applied to any moving mechanical platform as long as its position and velocity signals*

are continuous, bounded, and the required assumptions are satisfied.

Remark 14 *The initial range and the initial range estimate depend upon the actual values of the parameters and the initial estimate of the unknown parameter vector, respectively. If the initial error is high, the range estimation error will converge slower.*

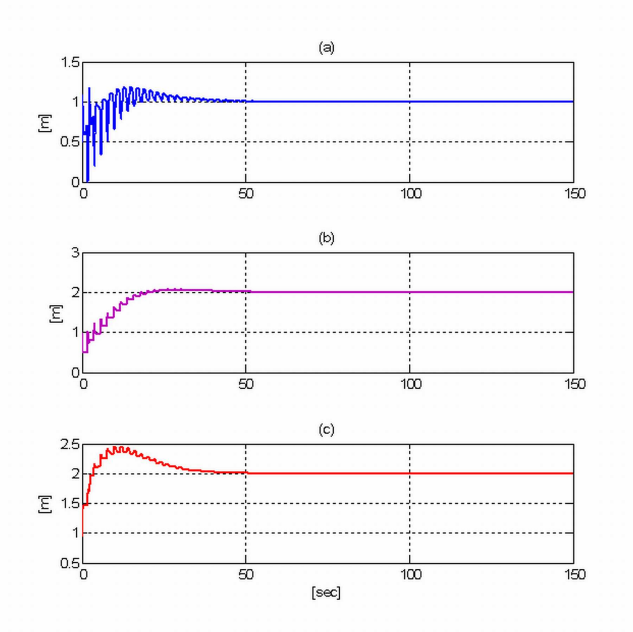

Figure 3.3 Simulation case 1: (a) $\hat{\theta}_1(t)$, (b) $\hat{\theta}_2(t)$, and (c) $\hat{\theta}_3(t)$.

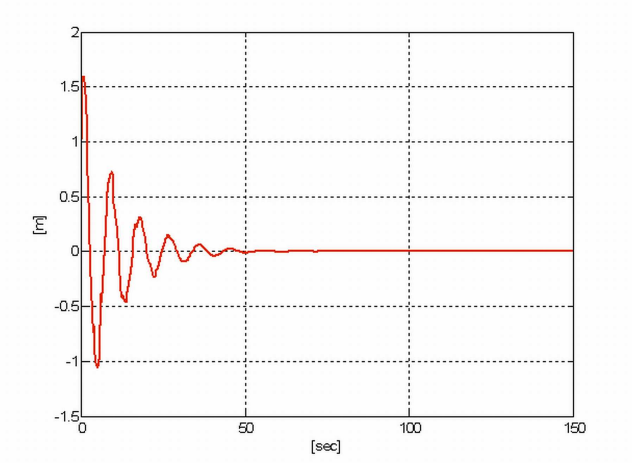

Figure 3.4 Simulation case 1: Range Estimation Error $z(t) - \hat{z}(t)$.

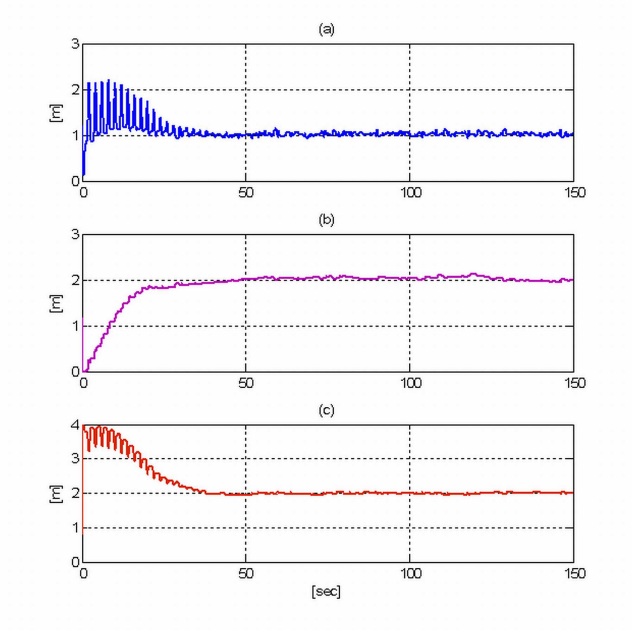

Figure 3.5 Simulation case 2: (a) $\hat{\theta}_1(t)$, (b) $\hat{\theta}_2(t)$, and (c) $\hat{\theta}_3(t)$.

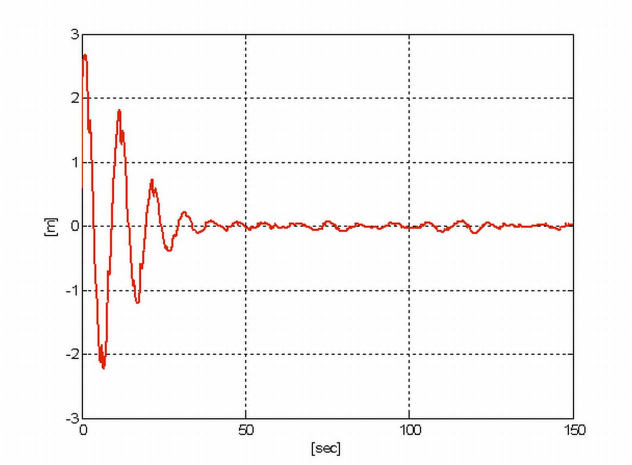

Figure 3.6 Simulation case 2: Range Estimation Error $z(t) - \hat{z}(t)$.

CHAPTER 4
OPTIMIZING ANTIANGIOGENIC THERAPY FOR TUMOR MINIMIZATION

Introduction

Tumor antiangiogenic therapy is an encouraging new form of cancer treatment which targets the vasculature of a growing tumor. A solid, avascular growing tumor reaches a size, a few millimeters in diameter, where it can no longer depend upon the blood vessels of the host to obtain its nutrition; thus, it starts the process of angiogenesis. This is a process where a tumor taps the surrounding mature host blood vessels to develop its own blood vessels [65]. The linings of these newly created blood vessels consist of endothelial cells. The tumor produces vascular endothelial growth factor to stimulate the endothelial cells growth along with inhibitors to suppress them [66], [67]. Antiangiogenic therapies were proposed in the early seventies by Folkman [68] to arrest this phase of tumor growth. As pointed out in [69], these treatments were enabled only after the discovery of the inhibitory mechanism of the tumor in the nineties [70]. Antiangiogenic therapies indirectly affect the tumor growth by providing external angiogenic inhibitors in the form of medication which targets the endothelial cells and block their growth; hence, a tumor is deprived of its necessary nutrition and ceases to grow. This therapy does not kill the fast replicating and mutating cancer cells, and instead targets the comparitively more stable endothelial cells. Hence, acquired drug resistance to the angiogenic inhibitors has not been observed [71]. Since the conventional chemotherapy treatments are often limited by the development of drug resistance by the tumor cells, antiangiogenic therapy has been considered as a promising treatment of tumors [72], [73].

There have been several mathematical models that describe the dynamics of angiogenesis. Some of these models attempt to fully describe the complexity of the biological processes [74], [75]. Ramanujan *et al.* [76] presented a model of tumor

growth based on the balance of pro-angiogenic and antiangiogenic signals. More complex PDE models are also presented in [77], [78], [79]. However, these models are not tractable for mathematical analysis [80]. Mathematical models that aim to describe a tumor growth in the vascular phase including the development of the vasculature are few. A simple mathematical model which emphasizes the concept that the development of vascular network controls the tumor growth process was developed and biologically validated by Hahnfeldt *et al.* [81]. This two-dimensional model uses ordinary differential equations to describe the interactions between the tumor volume and the carrying capacity of the endothelial cells. The model can easily represent the effect of antiangiogenic drugs and the predictions of the model have been successfully compared with the volume response of an experimental subcutaneous tumor implanted in mice treated with drugs [82]. The underlying spatial analysis carried out in the development of the model has spawned various modifications. A modification of this model has been presented by Ergun *et al.* [83]. More recently, a slight variant of the model by Hahnfeldt *et al.* was presented by d'Onofrio and Gandolfi [82]. This model assumes the potential doubling time of the vasculature to be constant. Also, it subdivides the endothelial cell pool, which is involved in angiogenesis, into resting and proliferating cells.

Since antiangiogenic therapy is a new cancer treatment, very few researchers have worked on controlling or administrating the drugs. Ledzewicz *et al.* [65], [69], [80], [84], [85], have proposed optimal control theory for administrating a given amount of drug dose to realize the minimum tumor size. Ergun *et al.* [83] and Swierniak *et al.* [86] also proposed optimal control theory to address the same problem. d'Onofrio and Gandolfi proposed open-loop periodic antiangiogenic therapy in [82] and constant infusion of antiangiogenic therapy [87] for tumor reduction. To obtain effective control on tumor growth, antiangiogenic therapy has been proposed by Kerbel and Folkman as an uninterrupted and a long-term therapy [88]. Futher, Cao [89], pointed out that a life-span delivery or injection of angiogenesis inhibitors to patients may be required

and research is going on to develop oral angiogenic drugs for therapy. It will be shown later in the paper that the tumor as well as the vasculature carrying capacity tend to grow if the medication is removed; thus, the regression of tumor volume is not guaranteed.

In this paper, we present an entirely different approach for tumor minimization from the aforementioned papers where optimal control theory was utilized and the drug dose was stopped after a certain time. As mentioned previously, tumor antiangiogenic therapy may require a long-term or a life-span delivery of drugs; hence, we are motivated to develop a tumor reduction technique which keeps the tumor size at a minimum and prevents it from growing using the least possible continuous drug dose. To this end, we first formulate a performance index which will be minimized. Then, we present a nonlinear, continuous control (*i.e.*, drug dose) to achieve the desired optimum value of the carrying capacity of the endothelial cells (and thus, the optimum size of the tumor) assuming exact model knowledge. However, it is a diffcult task to exactly measure or estimate the model parameters. Thus, we develop a prediction error based least-squares estimation technique to identify the unknown parameters used in the performance index. Further, an adaptive controller is designed to track the desired optimum trajectory for the carrying capacity of endothelial cells. The optimum trajectory is obtained through an optimization algorithm which seeks the minimum of the performance index. The developed tumor minimization technique successfully finds the optimum values of the tumor size and the carrying capacity of endothelial cells, and it prevents them from growing by maintaining an optimum drug dose as demonstrated by the simulation results. As an extension of this work, we show how the proposed technique can be extended to a model which describes pharmacokinetics and pharmacodynamics. Further, we also show how to estimate the carrying capacity of endothelial cells if required.

System Model

In our work, we consider the model proposed by d'Onofrio and Gandolfi [82]

to relate tumor growth, vascular growth, and the effect of an antiangiogenic therapy. This model allows for a detailed description of the drug effects, and is given as follows

$$\dot{p} = \alpha p\left(1 - \frac{p}{q}\right) \tag{4.1}$$

$$\dot{q} = bq - dp^{2/3}q - Guq \tag{4.2}$$

where $p(t) \in \mathbb{R}$ is the tumor volume in $[\text{mm}]^3$, $q(t) \in \mathbb{R}$ is the carrying capacity of the endothelial cells, also measured in $[\text{mm}]^3$, and $\alpha \in \mathbb{R}$ is a positive tumor growth parameter. In (4.2), the term bq accounts for the proliferation kinetics of the endothelial cells and the term $dp^{2/3}q$ models endogenous inhibition of the tumor. The exponent $2/3$ arises from the geometrical argument that the inhibitors generated within the tumor are transported out of the tumor through the tumor surface, modeled as a sphere. The parameters $b, d \in \mathbb{R}$ are positive growth constants. The positive constant $G \in \mathbb{R}$ denotes the antiangiogenic killing parameter, and $u(t) \in \mathbb{R}$ is the manipulated control input which corresponds to the drug dose, measured in [conc.]. A term which represents a spontaneous vasculature loss is often neglected in the literature as it is very small compared to other factors [65]; thus, it is omitted in the above model.

To investigate the steady-state properties of the system model given in (4.1) and (4.2), we calculate its equilibria corresponding to a constant drug dose $u = u_0$; $u_0 \in \mathbb{R}$ being the steady-state value of $u(t)$. To this end, we set the right-hand sides of (4.1) and (4.2) equal to zero. After some algebraic manipulations we obtain the following two equilibria

$$p_0 = q_0 = 0 \tag{4.3}$$

and

$$p_0 = q_0 = \left(\frac{b - Gu_0}{d}\right)^{3/2}. \tag{4.4}$$

It should be noted that $p_0 = q_0 = 0$ is not an admissible point [82]. It is evident from (4.4) that if the control input is zero, the tumor volume $p(t)$ along with $q(t)$ rise and go to their respective equilibria which is $p_0 = q_0 = 17320$ $[\text{mm}]^3$. This supports

the previously mentioned claim that an uninterrupted or a long-term antiangiogenic therapy is required to prevent growth of the tumor. All the parameter values are taken from [82], and are given as follows

$$\begin{aligned} \alpha &= 1.08\ [\text{day}]^{-1} \qquad d = 3.63 \times 10^{-4}\ [\text{day}]^{-1}[\text{mm}]^{-2} \\ b &= 0.243\ [\text{day}]^{-1} \qquad G = 1.3\ [\text{day}]^{-1}[\text{conc.}]^{-1}. \end{aligned} \tag{4.5}$$

Assumption 6 *In this work, we assume that the tumor volume $p(t)$ along with the carrying capacity of endothelial cells $q(t)$ are measurable. Furthermore, we restrict our analysis to a biologically realistic domain where $p(t) > 0$ and $q(t) > 0$ for all time instants.*

Control Problem

The goal of this work is to design a therapy regimen for $u(t)$ that minimizes the volume of the while minimizing the drug dose. We propose that these objectives will be met if the following performance index is minimized

$$J = p + \left(\frac{Gu}{d}\right)^{3/2}. \tag{4.6}$$

The performance index $J(t) \in \mathbb{R}$ captures the treatment goal using the summation of tumor size and drug dose. The drug dose $u(t)$ in the performance index is multiplied by a factor of G/d and then raised to $3/2$ to obtain the same unit as $p(t)$; thus, $J(t)$ is expressed in $[\text{mm}]^3$. The steady-state expression for the performance index can be written as

$$J_0 = p_0 + \left(\frac{Gu_0}{d}\right)^{3/2} \tag{4.7}$$

where J_0, p_0, and u_0 are the steady-state values of $J(t)$, $p(t)$, and $u(t)$, respectively. The minimum of this performance index gives the minimum tumor volume that can be obtained and kept at that value with the minimum amount of the drug dose $u(t)$. Figure 4.1 shows the plot for J_0 with respect to the steady-state values of $u(t)$, denoted

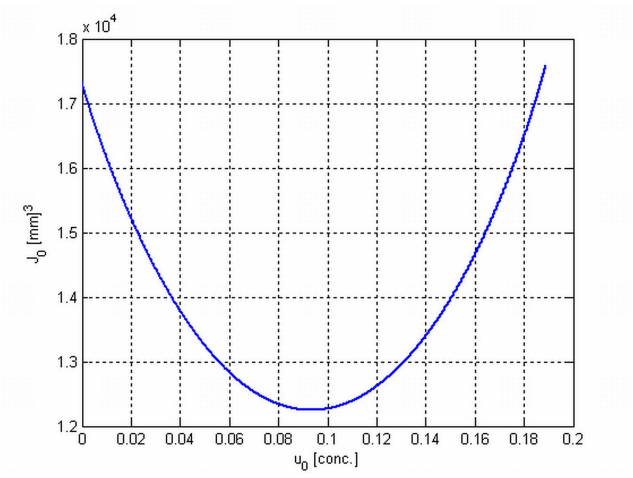

Figure 4.1 Steady-state performance index J_0 with respect to the steady-state values of the drug dose u_0.

by u_0. Figure 4.2 shows J_0 with respect to the steady-state values of $p(t)$ and $q(t)$. Thus, the control objective is to minimize the performance index given in (4.6) and drive the carrying capacity of the endothelial cells $q(t)$ to its optimum value $q^\star$. From (4.4) and from Figure 4.2, it can be seen that at steady-state, $q(t)$ is equal to $p(t)$; thus, driving $q(t)$ to its optimum value makes $p(t)$ to go to its optimum value. The minimum value of the performance index at steady-state J_0, and the optimum values of $u(t)$, $p(t)$, and $q(t)$ at their respective steady-states can be seen in Figures 4.1 and 4.2, and are given as follows

$$\begin{aligned} J^\star &= 12,247\ [\text{mm}]^3 \qquad u^\star = 0.0938\ [\text{conc.}] \\ p^\star &= q^\star = 6115\ [\text{mm}]^3. \end{aligned} \tag{4.8}$$

Controller Development with Exact Model Knowledge

In this section, a continuous nonlinear controller is presented to manipulate the drug dose $u(t)$ in order to minimize the tumor volume using the minimum drug dose. From (4.6), it is clear that if we have an exact knowledge of the model parameters, we can obtain the minimum value of the performance index, and the optimum values

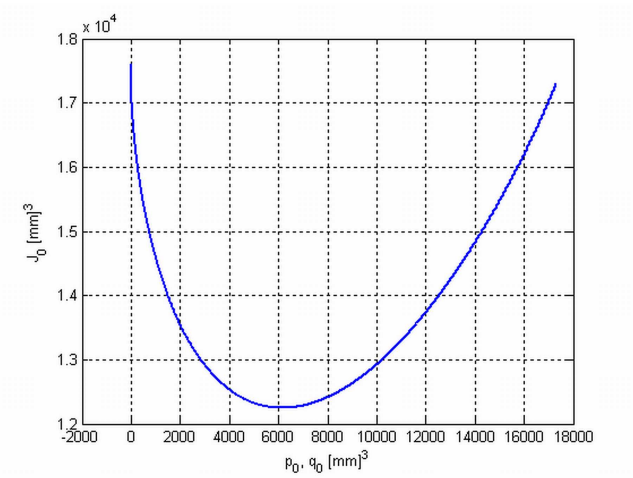

Figure 4.2 Steady-state performance index J_0 with respect to the steady-state values of the tumor volume p_0 and the carrying capacity of the endothelial cells q_0 ($q_0 = p_0$ at equilibrium).

of $p(t)$ and $q(t)$ as given in (4.8); thus, a set-point control for $q(t)$ can be designed to achieve

$$q(t) \to q^\star \text{ as } t \to \infty. \tag{4.9}$$

As stated earlier, $p(t) = q(t)$ at steady-state; thus, if $q(t)$ goes to $q^\star$ then $p(t) \to p^\star = q^\star$.

To facilitate the control developement, we define the tracking error $e_m(t) \in \mathbb{R}$ as follows

$$e_m \triangleq q - q^\star. \tag{4.10}$$

After taking the time derivative of (4.10), the following expression is obtained

$$\dot{e}_m = bq - dp^{2/3}q - Guq \tag{4.11}$$

where (4.2) was utilized. Based on the subsequent stability analysis, the following control law is proposed

$$u \triangleq \frac{1}{Gq}\left(bq - dp^{2/3}q + k_m e_m\right) \tag{4.12}$$

where $k_m \in \mathbb{R}$ is a positive control gain.

Remark 1 *From (4.1) and Assumption 6, it is clear that $\dot{p}(t) \leq 0$ when $p(t) \geq q(t)$; thus, $p(t)$ decreases. If $p(t) < q(t)$, $p(t)$ will increase until $p(t) = q(t)$, and will start to decrease again if $p(t) \geq q(t)$. Therefore, $p(t)$ is bounded as long as $q(t)$ is bounded.*

Stability Analysis

Theorem 5 *The control law given in (4.12) ensures that $e_m(t) \to 0$ exponentially.*

Proof. After substituting (4.12) into (4.11), we obtain the following error dynamics

$$\dot{e}_m = -k_m e_m. \tag{4.13}$$

After solving the differential equation given in (4.13), the following expression can be obtained

$$e_m(t) = e_m(t_0) \exp(-k_m t). \tag{4.14}$$

It is clear from (4.14) that $e_m(t) \to 0$ exponentially; thus, $q(t) \to q^\star$ exponentially fast.

From (4.14), we can infer $e_m(t) \in \mathcal{L}_\infty$; hence, from (4.10), it follows that $q(t) \in \mathcal{L}_\infty$. Since $q(t)$ is bounded, from Remark 1, it follows that $p(t) \in \mathcal{L}_\infty$. The control input $u(t)$ given in (4.12) is a function of bounded signals (*i.e.*, $p(t)$ and $q(t)$) and known constant parameters, therefore, $u(t) \in \mathcal{L}_\infty$.

Controller Development with Uncertain Model Knowledge

As mentioned previously in the Introduction, in practice, it is difficult to exactly determine the model parameters for a specific patient. To adderess this issue, we define an estimate of the performance index given in (4.6), denoted by $\hat{J}(t) \in \mathbb{R}$, as follows

$$\hat{J} \triangleq p + \left(\frac{\hat{G}u}{\hat{d}}\right)^{3/2} \tag{4.15}$$

where $\hat{G}(t), \hat{d}(t) \in \mathbb{R}$ are estimates of G and d, respectively. The control objective remains the same as outlined in previous section, *i.e.*, to minimize $\hat{J}(t)$ given in

(4.15) and drive $q(t)$ from a given initial condition to its optimum value $q^\star$ in order to drive $p(t)$ to its optimum value $p^\star$. However, we can no longer utilize a set-point control as previously described because of the lack of knowledge about the model parameters. To overcome this problem, we design an adaptive controller to track an optimum desired trajectory $q_d(t) \in \mathbb{R}$ such that $q(t) \to q_d(t)$ as $t \to \infty$. The desired optimum trajectory is dynamically generated online using a numerical-based optimization algorithm, described later, to minimize the performance index given in (4.15), such that $q_d(t) \to q^\star$ where $q^\star$ is the optimum value of $q(t)$ at steady-state. Thus, the overall control objective can be stated as follows

$$q(t) \to q_d(t) \to q^\star \text{ as } t \to \infty. \tag{4.16}$$

Parameter Estimation

In this subsection, we design an estimator based on the least-squares estimation technique to generate estimates of the unknown constant parameters b, d, and G. The estimates $\hat{G}(t)$ and $\hat{d}(t)$ are then utilized in (4.15). To facilitate the estimator development, we parameterize (4.2) as follows

$$Q = W_e \theta_e \tag{4.17}$$

where $Q(t)$ denotes $\dot{q}(t)$ and $W_e(t) \in \mathbb{R}^{1\times 3}$ represents a measurable regression vector which is defined as follows

$$W_e \triangleq \begin{bmatrix} q & -p^{2/3}q & -uq \end{bmatrix}. \tag{4.18}$$

In (4.17), $\theta_e \in \mathbb{R}^3$ is a vector of unknown constant parameters defined as follows

$$\theta_e \triangleq \begin{bmatrix} b & d & G \end{bmatrix}^T. \tag{4.19}$$

To further facilitate the estimator design, we define a prediction error $\varepsilon(t) \in \mathbb{R}$ as follows

$$\varepsilon \triangleq Q_f - \hat{Q}_f \tag{4.20}$$

where $Q_f(t) \in \mathbb{R}$ is a filtered signal defined as follows

$$\dot{Q}_f \triangleq -\beta Q_f + \beta Q \ ; \ Q_f(t_0) = 0 \tag{4.21}$$

where $\beta \in \mathbb{R}$ is a positive constant. Notice that (4.21) can not be implemented since $Q(t)$ is unmeasurable. The reader is referred to Appendix M for the implementable form of the filtered signal. In (4.20), $\hat{Q}_f(t) \in \mathbb{R}$ is the estimate of $Q_f(t)$, defined as follows

$$\hat{Q}_f \triangleq W_f \hat{\theta}_e \tag{4.22}$$

where $W_f(t) \in \mathbb{R}^{1\times 3}$ is a filtered regression vector, written as follows

$$\dot{W}_f \triangleq -\beta W_f + \beta W_e \ ; \ W_f(t_0) = 0_{1\times 3} \tag{4.23}$$

where $0_{1\times 3}$ denotes a 1-by-3 vector of zeros and β was introduced in (4.21). In (4.22), $\hat{\theta}_e(t) \triangleq \left[\begin{array}{ccc} \hat{b} & \hat{d} & \hat{G} \end{array} \right]^T \in \mathbb{R}^3$ is the estimate vector of the unknown parameters. After substituting (4.17) into (4.21), the following expression can be obtained

$$\dot{Q}_f + \beta Q_f = \beta W_e \theta_e. \tag{4.24}$$

The expression given in (4.24) can be rewritten as follows

$$\dot{Q}_f + \beta Q_f = \dot{W}_f \theta_e + \beta W_f \theta_e \tag{4.25}$$

where (4.23) was utilized. After taking the time derivative of (4.22), and then adding and subtracting the term $\dot{W}_f \hat{\theta}_e$ to the right-hand side of the resulting expression, the following expression can be obtained

$$\dot{\hat{Q}}_f + \beta \hat{Q}_f = \frac{d}{dt}\left(W_f \hat{\theta}_e\right) + \beta W_f \hat{\theta}_e \tag{4.26}$$

where (4.22) and (4.23) were utilized. After subtracting (4.26) from (4.25), and utilizing (4.20) and (4.23), the resulting expression can be written as follows

$$\dot{\varepsilon} + \beta \varepsilon = \frac{d}{dt}\left(W_f \tilde{\theta}_e\right) + \beta W_f \tilde{\theta}_e \tag{4.27}$$

where $\tilde{\theta}_e(t) \in \mathbb{R}^3$ is the estimation error signal defined as follows

$$\tilde{\theta}_e \triangleq \theta_e - \hat{\theta}_e. \tag{4.28}$$

From (4.27), it can be shown that a mathematically useful, but unrealizable, form of the prediction error $\varepsilon(t)$ given in (4.20) can be written as follows [90]

$$\varepsilon = W_f \tilde{\theta}_e. \tag{4.29}$$

Based on the subsequent stability analysis, the following continuous least-squares update law $\dot{\hat{\theta}}_e(t) \in \mathbb{R}^3$ is employed for estimating the unknown parameters

$$\dot{\hat{\theta}}_e \triangleq \Gamma W_f^T \varepsilon \tag{4.30}$$

where $\Gamma(t) \in \mathbb{R}^{3\times 3}$ is the least-squares estimation gain matrix which is designed as follows

$$\dot{\Gamma}^{-1} \triangleq W_f^T W_f. \tag{4.31}$$

Remark 2 *If $Q(t)$ is bounded, from (4.21), we can show that $Q_f(t), \dot{Q}_f(t) \in \mathcal{L}_\infty$. Similarly, if $W_e(t) \in \mathcal{L}_\infty$, from (4.23), we can show that $W_f(t), \dot{W}_f(t) \in \mathcal{L}_\infty$. The reader is referred to [90] for a detailed description.*

Remark 3 *It should be noted that if $\Gamma^{-1}(t_0)$ is selected to be positive definite and symmetric then $\Gamma(t_0)$ is also positive definite and symmetric. Therefore, it follows that both $\Gamma^{-1}(t)$ and $\Gamma(t)$ are positive definite and symmetric. The following expression can be obtained from (4.31)*

$$\dot{\Gamma} = -\Gamma W_f^T W_f \Gamma. \tag{4.32}$$

It can be easily seen from (4.32) that $\dot{\Gamma}(t)$ is negative semidefinite; therefore, $\Gamma(t)$ is always constant or decreasing; hence, it follows that $\Gamma(t)$ is bounded (for more details, the reader is referred to [31] and [32]).

Development of Adaptive Control Law

To proceed with the development of an adaptive control law to achieve the control objective stated in (4.16), we divide both sides of (4.2) by G to obtain the following expression

$$\frac{1}{G}\dot{q} = \frac{b}{G}q - \frac{d}{G}p^{2/3}q - uq. \tag{4.33}$$

The expression given in (4.33) is then parameterized as follows

$$A\dot{q} = W_0\theta_0 - uq \tag{4.34}$$

where $A \triangleq G^{-1} \in \mathbb{R}$ is a positive unknown constant, and $W_0(t) \in \mathbb{R}^{1\times 2}$ is a measurable regression vector defined as follows

$$W_0 \triangleq \begin{bmatrix} q & -p^{2/3}q \end{bmatrix}. \tag{4.35}$$

In (4.34), $\theta_0 \in \mathbb{R}^2$ is a vector of unknown constants, defined as follows

$$\theta_0 \triangleq \begin{bmatrix} bA & dA \end{bmatrix}^T. \tag{4.36}$$

To facilitate the development, we define a tracking error $e_a(t) \in \mathbb{R}$ as follows

$$e_a \triangleq q - q_d \tag{4.37}$$

where $q_d(t) \in \mathbb{R}$ is a subsequently designed optimum desired trajectory for $q(t)$. The desired trajectory $q_d(t)$ is designed such that $q_d(t), \dot{q}_d(t) \in \mathcal{L}_\infty$ as shown later in Section V-C. After taking the time derivative of (4.37), and then multiplying both the sides of the resulting expression by A, we can write the following expression

$$A\dot{e}_a = A\dot{q} - A\dot{q}_d. \tag{4.38}$$

After substituting (4.34) into (4.38), the following expression is obtained

$$A\dot{e}_a = W_0\theta_0 - uq - A\dot{q}_d \tag{4.39}$$

which can be rewritten in a parameterized form as follows

$$A\dot{e}_a = W_a\theta_a - uq. \tag{4.40}$$

In (4.40), $W_a(t) \in \mathbb{R}^{1\times 3}$ is a measurable regression vector and $\theta_a \in \mathbb{R}^3$ is a vector of unknown constants defined as follows

$$W_a \triangleq \begin{bmatrix} W_0 & -\dot{q}_d \end{bmatrix} \tag{4.41}$$

and

$$\theta_a \triangleq \begin{bmatrix} \theta_0^T & A \end{bmatrix}^T. \tag{4.42}$$

Based on the subsequent stability analysis, the control input $u(t)$ is designed as follows

$$u \triangleq \frac{1}{q}\left(W_a\hat{\theta}_a + k_a e_a\right) \tag{4.43}$$

where $\hat{\theta}_a(t) \in \mathbb{R}^3$ is an estimate vector of θ_a, and the adaptive update law $\dot{\hat{\theta}}_a(t) \in \mathbb{R}^3$ is designed as follows

$$\dot{\hat{\theta}}_a \triangleq \gamma_a W_a^T e_a. \tag{4.44}$$

In (4.43) and (4.44), $k_a, \gamma_a \in \mathbb{R}$ are positive constants.

Optimum Trajectory Generation

In this subsection, an optimum desired trajectory $q_d(t)$ is designed which is fed to the adaptive controller given in previous section. This continuous optimum trajectory $q_d(t)$ is designed to minimize the performance index given in (4.15) where the estimates for the parameters G and d, obtained as described previously, are utilized. For the minimization of the estimate of the performance index, $\hat{J}(t)$, a gradient descent algorithm is employed which guesses the optimum value $\bar{q}_d[n]$ at each time step of the optimization algorithm. The output of the algorithm, $\bar{q}_d[n]$, is passed through a set of second-order, stable and proper, low-pass filters to generate continuous and bounded signals for $q_d(t)$ and $\dot{q}_d(t)$. The following filters are utilized

$$q_d(t) = \frac{\varsigma_1}{\varsigma_2 s^2 + \varsigma_3 s + \varsigma_4}\bar{q}_d[n], \tag{4.45}$$

$$\dot{q}_d(t) = \frac{s\varsigma_1}{\varsigma_2 s^2 + \varsigma_3 s + \varsigma_4}\bar{q}_d[n] \tag{4.46}$$

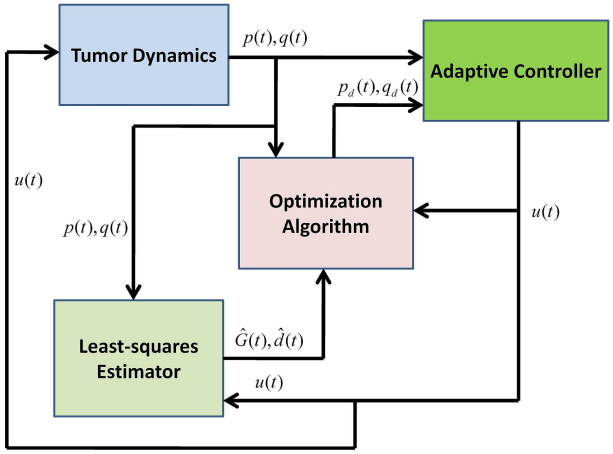

Figure 4.3 A block-diagram representation of the developed tumor minimization technique.

where $\varsigma_1, \varsigma_2, \varsigma_3, \varsigma_4 \in \mathbb{R}$ are positive filter constants, and $n \in \mathbb{Z}$ is a positive integer (*i.e.*, the iteration step of the algorithm). At step n, the optimum trajectory holds the output, $\bar{q}_d[n]$, constant until the response of the closed-loop system, $q(t)$, has reached a steady-state near $q_d(t)$. A new target optimum $\bar{q}_d[n+1]$ is then issued. In other words, the algorithm waits for certain thresholds to be satisfied before it proceeds to the next iteration. For instance, if $|q(t) - q_d(t)| \leq \bar{e}_1$, $|\bar{q}_d[n] - q_d(t)| \leq \bar{e}_2$, and $|q(t) - p(t)| \leq \bar{e}_3$ then $n = n+1$ where $\bar{e}_1, \bar{e}_2, \bar{e}_3 \in \mathbb{R}$ are threshold constants. Furthermore, the designed trajectory can be concluded to have converged when the gradient of $\hat{J}(t)$ with respect to $q(t)$ is within a certain threshold. Once the optimization algorithm satisfies the termination criteria, it stops updating $\bar{q}_d[n]$. As the performance index approaches its minimum value, the desired trajectory $q_d(t)$ and $u(t)$ approach $\hat{q}^\star$ and $\hat{u}^\star$, respectively. $\hat{q}^\star$, $\hat{u}^\star \in \mathbb{R}$ are the estimates of the optimum values of $q(t)$ and $u(t)$, respectively that are resulted from the optimum seeking algorithm.

As mentioned earlier, at steady-state $p(t) = q(t)$; therefore, $p(t) \to p_d(t) \to \hat{p}^\star$ as $q(t) \to q_d(t) \to \hat{q}^\star$ where $p_d(t) = q_d(t)$ and $\hat{p}^\star = \hat{q}^\star$. Then $\hat{p}^\star$ is the estimated optimum tumor volume that can be realized by applying the estimated optimum drug dose $\hat{u}^\star$.

Stability Analysis

Theorem 6 *The update law defined in (4.30) ensures that* $\|\tilde{\theta}_e(t)\| \to 0$ *as* $t \to \infty$ *provided that the following Persistency of Excitation (PE) condition [49] holds*

$$\kappa_1 I_3 \leq \int_{t_0}^{t_0+\delta} W_f^T(\tau) W_f(\tau) d\tau \leq \kappa_2 I_3 \tag{4.47}$$

where κ_1, κ_2, $\delta \in \mathbb{R}$ *are positive constants, and* I_3 *is a standard 3-by-3 identity matrix.*

Proof. See Appendix N.

Remark 4 *The PE condition given in (4.47) can be fulfilled by guaranteeing that the signals in the regression matrix vary in a sufficiently independent manner within a time-window. The reader is referred to [91] for a detailed explanation.*

Theorem 7 *The control law* $u(t)$ *given in (4.43) and the adaptive update law defined in (4.44) guarantee that* $e_a(t) \to 0$ *as* $t \to \infty$.

Proof. See Appendix O.

Simulation Results

A numerical simulation study was conducted to evaluate the developed tumor treatment optimization technique using Mathworks Simulink program. It should be noted that the least-squares estimator, the adaptive controller, and the optimization algorithm, were run simultaneously as shown in Fig. 4.3. All the parameter values for the simulation were taken from [82] and are given in (4.5). The initial conditions for $p(t)$ and $q(t)$ were selected as follows

$$p(t_0) = 10,000\ [\text{mm}]^3 \quad q(t_0) = 12,000\ [\text{mm}]^3. \tag{4.48}$$

It can be seen from (4.48) that $q(t_0) > p(t_0)$. In other words, the carrying capacity of the endothelial cells is greater than the tumor volume; thus, the tumor volume is susceptible to an increase in the absence of a proper therapy.

The least-squares estimator given in (4.30) was initialized as $\hat{\theta}_e(t_0) = 0.1\theta_e$, and the estimation gain matrix was initialized as $\Gamma^{-1}(t_0) = 10I_3$. The positive constant β, introduced in (4.21), was set to $\beta = 0.005$. The adaptive update law was initialized as $\hat{\theta}_a(t_0) = 0_3$ where 0_3 denotes a 3-by-1 vector of zeros. The positive gains were set as $k_a = 10$ and $\gamma_a = 1.3 \times 10^{-12}$. Additionally, the initial guess, $\bar{q}_d[0]$, was selected to be 9000 $[\text{mm}]^3$.

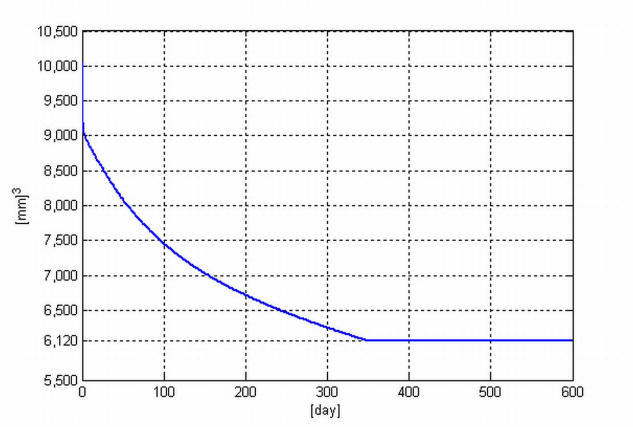

Figure 4.4 The time evolution of the tumor volume $p(t)$.

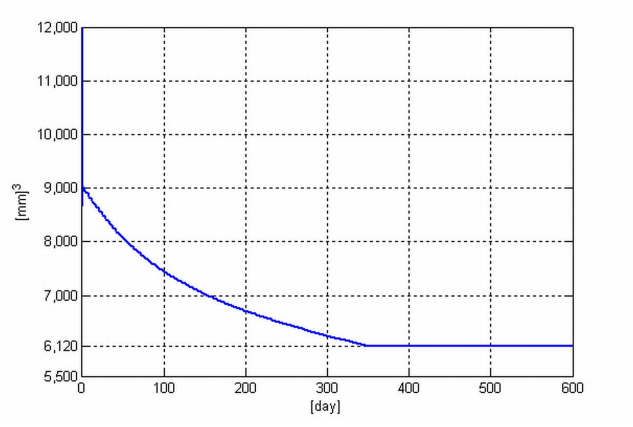

Figure 4.5 The time evolution of the carrying capacity of endothelial cells $q(t)$.

The time evolution of the tumor volume $p(t)$ and the carrying capacity of the endothelial cell volume $q(t)$ are shown in figures 4.4 and 4.5, respectively. It can be seen from these figures that $p(t)$ and $q(t)$ converge to their respective optimum

values $p^\star \pm 5$ [mm]^3 and $q^\star \pm 5$ [mm]^3 given in (4.8), respectively. Fig. 4.6 shows the time evolution of the drug dose $u(t)$. The inset plot in this figure shows $u(t)$ during day one of the therapy. It can be inferred from Fig. 4.6 that $u(t)$ starts from a high dose and then converges to its optimum value $u^\star \pm 0.0003$[conc.]. The time evolution of the estimate of the performance index, $\hat{J}(t)$, is shown in Fig. 4.7. It can be seen from Fig. 4.7 that $\hat{J}(t)$ converges to $J^\star \pm 3$ [mm]^3. It should be noted that if the initial conditions, $p(t_0)$ and $q(t_0)$, were chosen to be smaller values, then the convergence would have been faster. Furthermore, if the initial guess for the optimization algorithm was selected very close to $q(t_0)$, the drug dose during day one would have been lower than 2.5 [conc.] but the convergence would have been slower. Fig. 4.8 shows the least-squares estimate of the unknown vector θ_e. It can be seen from this figure that all the parameters are accurately identified. Fig. 4.9 shows the tracking error $e_a(t)$. The inset in this figure shows $e_a(t)$ during day one of the therapy period. It can be seen from Fig. 4.9 that the tracking error $e_a(t)$ is driven to zero. It can be concluded from the simulation study that the developed tumor minimization technique can efficiently reduce the tumor volume with an optimum drug dose.

Remark 5 *From Theorem 7 and the optimum seeking algorithm, it can be concluded that* $q(t) \to q_d(t)$ *as* $t \to \infty$ *and* $q_d(t) \to \hat{q}^\star$. *From the simulation results, it can be further seen that if* $\hat{q}^\star = q^\star$ *then* $\hat{u}^\star = u^\star$ *resulting in an optimal solution. However, if the optimization algorithm does not locate the exact optimal values, the solution results into one of a sub-optimal nature.*

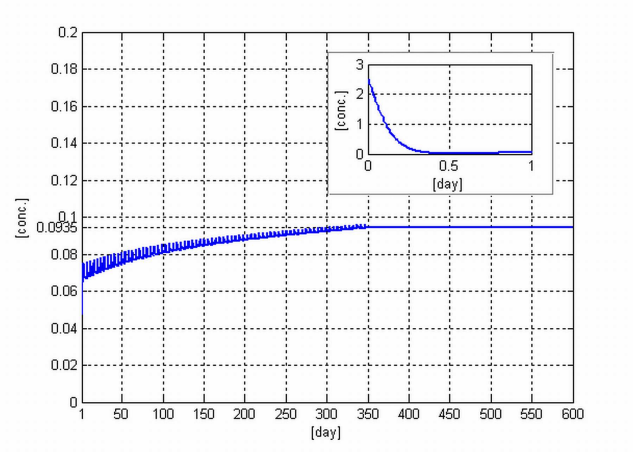

Figure 4.6 The time evolution of the drug dose $u(t)$.

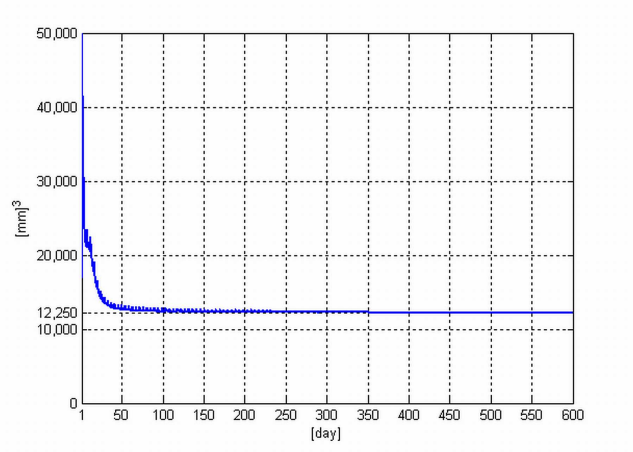

Figure 4.7 Time evolution of the estimate of the performance index, $\hat{J}(t)$.

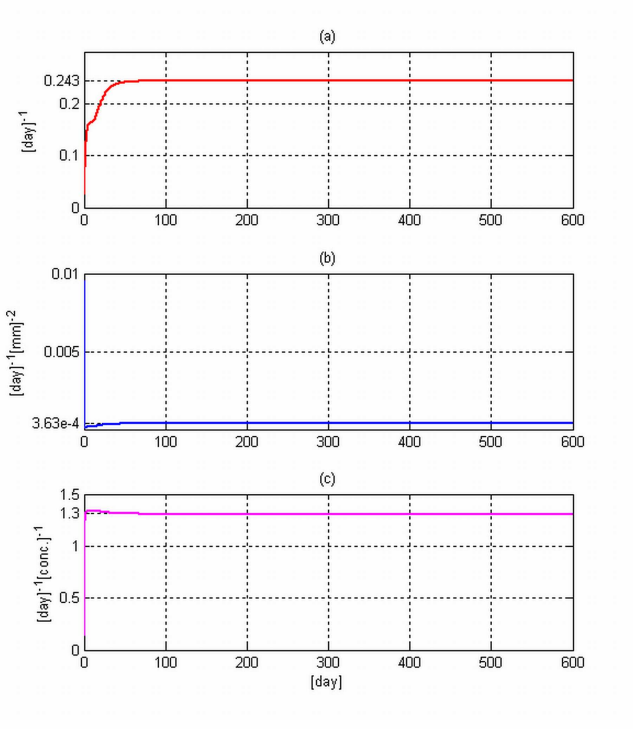

Figure 4.8 Least-squares estimation: (a) $\hat{b}(t)$, (b) $\hat{d}(t)$, and (c) $\hat{G}(t)$.

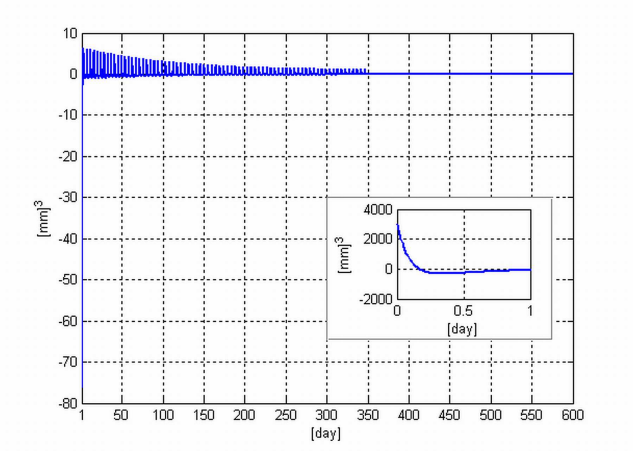

Figure 4.9 Tracking error $e_a(t)$.

CHAPTER 5
CONCLUSIONS

This dissertation presents contributions to two research areas: Nonlinear estimation techniques for range identification of vision-based systems and nonlinear control technique for optimization of tumor volume.

In Chapter 1, A novel estimation technique for range along with 3D Euclidean coordinates of features on a static object, with a moving calibrated camera whose position is measurable, was presented. An adaptive update law was designed by utilizing a unique prediction error formulation. It was proven that Euclidean distance estimation error signals are driven to zero, upon satisfaction of a persistent excitation condition. Detailed numerical simulation results and some comparative simulation results along with experimental results were presented demonstrating the robustness and accuracy of the estimator. The estimator accurately identifies the Euclidean distances between the features and thus, the range and the 3D Euclidean positions of the features without any information about the object's geometry. The results show that the proposed estimator can be used for range identification where position measurements are readily available.

In Chapter 2, A novel technique for estimation of 3D Euclidean coordinates of features on a static object with an uncalibrated camera mounted on a moving mechanical system was presented. The position information of the mechanical system was available and information of a second object was assumed to be known. Two adaptive update laws were presented utilizing formulations of a prediction error and an auxiliary prediction error, respectively, that facilitated the 3D Euclidean coordinates estimation and compensation for the unknown camera calibration parameters. It was proven that the Euclidean distance estimation error signals were driven to zero.

In Chapter 3, A novel technique for range identification and recovering the 3D Euclidean coordinates of a static object feature with a calibrated paracatadioptric system mounted on a moving platform with measurable position was presented. An

adaptive estimator for a nonlinearly parameterized function of projected pixel coordinates was presented which facilitated the range estimation along with the estimation of 3D Euclidean coordinates of an object feature. A Lyapunov-type stability analysis was presented to prove that the proposed estimator is stable, and ensures global boundedness of the error signals. Further, the parameter estimation error signals were shown to be bounded by a desired precision upon satisfaction of an NLPE condition. Numerical simulation results were presented to demonstrate the efficiency of the developed range identification technique and its robustness to noise. The results show that the developed estimator can be used for range identification for the applications with paracatadioptric systems where position measurements are readily avaliable.

In Chapter 4, A novel approach to optimize antiangiogenic therapy for tumor minimization was presented. We considered the mathematical problem to minimize the tumor volume and prevent it from growing using a continuous optimum drug dose. A performance index was formulated which was minimized in order to obtain the optimum value of the tumor volume. It was shown that given exact model knowledge, the tumor volume can be driven to its optimum value exponentially fast. In the absence of model knowledge, a least-squares estimation strategy was presented which facilitated the estimation of the performance index. An optimum trajectory generator was presented which seeks the unknown minimum of the performance index while ensuring that the desired trajectory remains bounded and sufficiently differentiable. An adaptive controller was then developed to track the desired trajectory in the presence of uncertainties in the model in order to minimize the tumor volume with an optimum dose of drug. It was proven that the least-squares estimation errors are driven to zero upon the satisfaction of a PE condition. Numerical simulation results were presented demonstrating the efficacy of the developed tumor minimization technique. The developed technique successfully minimized the tumor volume along with the carrying capacity of endothelial cells with an optimum drug dose despite the lack of knowledge about the sytem model. The proposed tumor minimization

technique was also shown to be applicable for the model with pharmacodynamics and pharmacokinetics. Further, an estimation technique was presented to identify the carrying capacity of endothelial cells.

APPENDICES

Appendix A

Proof of Theorem 1

To facilitate the proof, a nonnegative Lyapunov function $V(t) \in \mathbb{R}$ is defined as follows

$$V \triangleq \frac{1}{2}\tilde{\theta}^T \Gamma^{-1} \tilde{\theta} \tag{A.1}$$

where $\Gamma^{-1}(t) \in \mathbb{R}^{4\times 4}$ was defined in (1.27). The time derivative of (A.1) is given as follows

$$\dot{V} = \frac{1}{2}\dot{\tilde{\theta}}^T \Gamma^{-1}\tilde{\theta} + \frac{1}{2}\tilde{\theta}^T \dot{\Gamma}^{-1}\tilde{\theta} + \frac{1}{2}\tilde{\theta}^T \Gamma^{-1}\dot{\tilde{\theta}}\,. \tag{A.2}$$

The expression in (A.2) can be written as follows

$$\dot{V} = \tilde{\theta}^T \Gamma^{-1}\dot{\tilde{\theta}} + \frac{1}{2}\tilde{\theta}^T \dot{\Gamma}^{-1}\tilde{\theta}. \tag{A.3}$$

After utilizing the definition of $\tilde{\theta}(t)$ given in (1.21) and taking its derivative, (A.3) can be rewritten as follows

$$\dot{V} = -\tilde{\theta}^T \Gamma^{-1}\dot{\hat{\theta}} + \frac{1}{2}\tilde{\theta}^T \dot{\Gamma}^{-1}\tilde{\theta}. \tag{A.4}$$

After substituting (1.25) and (1.27) into (A.4), the following expression is obtained

$$\dot{V} = -\tilde{\theta}^T \Gamma^{-1}\text{Proj}\left\{\alpha \Gamma \bar{W}_p^T \tilde{p}\right\} + \tilde{\theta}^T \bar{W}_p^T \bar{W}_p \tilde{\theta}. \tag{A.5}$$

After utilizing the property of the projection (see (B.8) in Appendix B, $\dot{V}(t)$, can be upper bounded as follows

$$\dot{V} \leq -\alpha \tilde{\theta}^T \bar{W}_p^T \tilde{p} + \tilde{\theta}^T \bar{W}_p^T \bar{W}_p \tilde{\theta}. \tag{A.6}$$

It should be noted that, the expression (1.23) can be rearranged as follows

$$\bar{W}_p \tilde{\theta} = B^{-1}\tilde{p}. \tag{A.7}$$

From (1.11) and (1.24), we can write $B^{-1} = \Pi\theta = z$ and utilizing (1.13), it can be confirmed that B^{-1} exists. After utilizing (1.23), the expression in (A.6) can be rewritten as follows

$$\dot{V} \leq -\alpha \tilde{p}^T B^{-T}\tilde{p} + \tilde{p}^T B^{-T} B^{-1}\tilde{p}. \tag{A.8}$$

The right hand side of (A.8) can be upper bounded as follows

$$\dot{V} \leq -\alpha\varepsilon\tilde{p}^T\tilde{p} + \rho\tilde{p}^T\tilde{p} \tag{A.9}$$

where the definition of $B(t)$ in (1.24) is utilized along with (1.13). After substituting (1.26) into (A.9), the following inequality can be written

$$\dot{V} \leq -\varepsilon \left\|\tilde{p}\right\|^2. \tag{A.10}$$

After integrating (A.10), the following expression can be obtained

$$V(t_0) - V(\infty) > \varepsilon \int_{t_0}^{\infty} \left\|\tilde{p}\right\|^2 d\tau. \tag{A.11}$$

After utilizing (A.10) and the fact that $V(t)$ is nonnegative, it can be concluded that $V(\infty) \leq V(t_0)\ \forall\, t$; hence, $V(t)$ is bounded (i.e., $V(t) \in \mathcal{L}_\infty$) and from (A.11), it can be easily concluded that $\tilde{p}(t) \in \mathcal{L}_2$. The fact that the projected pixel coordinates $p(t) \in \mathcal{L}_\infty$, it follows that $\hat{p}(t) \in \mathcal{L}_\infty$. Since $z(t)$ is bounded and the fact that $\theta \in \mathcal{L}_\infty$, from (1.11) it follows that $\Pi(t) \in \mathcal{L}_\infty$; hence, from (1.17), it can be easily seen that $W(t) \in \mathcal{L}_\infty$. Since, $W(t)$, $\Pi(t)$ are bounded, it is clear from the definitions in (1.24) that $B(t)$, $\bar{W}_p(t) \in \mathcal{L}_\infty$. Since $\theta \in \mathcal{L}_\infty$, and $\hat{\theta}(t) \in \mathcal{L}_\infty$ because of the projection algorithm, therefore from (1.21), it follows that $\tilde{\theta}(t) \in \mathcal{L}_\infty$. Since, $B(t), \bar{W}_p(t) \in \mathcal{L}_\infty$ and $\tilde{p}(t) \in \mathcal{L}_2 \cap \mathcal{L}_\infty$, from (1.23) it can be concluded that $\bar{W}_p(t)\,\tilde{\theta}(t) \in \mathcal{L}_2 \cap \mathcal{L}_\infty$. From (1.27), it is clear that $\dot{\Gamma}^{-1}(t) \in \mathcal{L}_\infty$. Since, $\Gamma^{-1}(t)$ is always positive definite (see Remark 1) and $\bar{W}_p(t), \tilde{p}(t) \in \mathcal{L}_\infty$ and $\tilde{p}(t) \in \mathcal{L}_2$, from (1.25) it is easy to see that $\dot{\hat{\theta}}(t) \in \mathcal{L}_2 \cap \mathcal{L}_\infty$; hence, the time derivative of (1.21) can be used to show that $\dot{\tilde{\theta}}(t) \in \mathcal{L}_\infty$. From (1.11) and (1.12), we can also have $\dot{W}(t)$, $\dot{\Pi}(t)$; thus, from (1.18) $\dot{\hat{p}}(t) \in \mathcal{L}_\infty$. After utilizing the above boundedness statements along with the fact that it is a function of bounded signals, it is easy to see that $\frac{d}{dt}\bar{W}_p(t) \in \mathcal{L}_\infty$. Now, it follows that $\frac{d}{dt}\left(\bar{W}_p(t)\,\tilde{\theta}(t)\right) \in \mathcal{L}_\infty$. Since, $\bar{W}_p(t)\,\tilde{\theta}(t) \in \mathcal{L}_2 \cap \mathcal{L}_\infty$, it can be concluded from Barbalat's Lemma [92] that

$$\left\|\bar{W}_p(t)\,\tilde{\theta}(t)\right\| \to 0 \text{ as } t \to +\infty. \tag{A.12}$$

As shown in Appendix C, if the signal $\bar{W}_p(t)$ satisfies the persistent excitation (PE) condition given in (1.29), then from (A.12) it can further be concluded that

$$\left\|\tilde{\theta}(t)\right\| \to 0 \text{ as } t \to +\infty. \tag{A.13}$$

Appendix B

Projection Algorithm

The positiveness of the term $\Pi(t)\,\hat{\theta}(t)$ is ensured by a projection operator on $\dot{\hat{\theta}}(t)$ [31]. To facilitate the subsequent development, an auxiliary scalar function is defined as follows

$$\mathcal{P}\left(\hat{\theta}\right) \triangleq \bar{\varepsilon} - \Pi\hat{\theta} \tag{B.1}$$

where its gradient is computed as follows

$$\nabla_{\hat{\theta}}\mathcal{P}\left(\hat{\theta}\right) = \left[\begin{array}{cc} 0_{1\times 4} & -\Pi \end{array}\right] \tag{B.2}$$

where $\bar{\varepsilon}$ being an arbitrarily small positive constant and $0_{1\times 4} \in \mathbb{R}^{1\times 4}$ being a vector of zeros. Two convex sets based on the function $\mathcal{P}\left(\hat{\theta}\right)$ are defined as follows

$$\mathcal{R} \triangleq \left\{\hat{\theta} \in \mathbb{R}^4 : \mathcal{P}\left(\hat{\theta}\right) \leq 0\right\} \tag{B.3}$$

$$\mathcal{R}_\delta \triangleq \left\{\hat{\theta} \in \mathbb{R}^4 : \mathcal{P}\left(\hat{\theta}\right) \leq \delta\right\} \tag{B.4}$$

where $\delta \in \mathbb{R}$ is a positive constant that is very close to zero.

Let the boundary and the interior of set $\mathcal{R}$ be defined by $\partial\mathcal{R}$ and $\overset{\circ}{\mathcal{R}}$, respectively. Based on these definitions, the projection of $\tau(t)$ is defined as follows

$$\text{Proj}\{\tau\} \triangleq \begin{cases} \tau & \hat{\theta} \in \overset{\circ}{\mathcal{R}} \text{ or } \nabla_{\hat{\theta}}\mathcal{P}^T\tau \leq 0 \\ P_\tau & \hat{\theta} \in \mathcal{R}_\delta \backslash \overset{\circ}{\mathcal{R}} \text{ and } \nabla_{\hat{\theta}}\mathcal{P}^T\tau > 0 \end{cases} \tag{B.5}$$

where $P_\tau(t) \in \mathbb{R}^{nq}$ is defined as follows

$$P_\tau = \left(I - c\left(\hat{\theta}\right)\Gamma\frac{\nabla_{\hat{\theta}}\mathcal{P}\nabla_{\hat{\theta}}\mathcal{P}^T}{\nabla_{\hat{\theta}}\mathcal{P}^T\Gamma\nabla_{\hat{\theta}}\mathcal{P}}\right)\tau \tag{B.6}$$

where the auxiliary scalar function $c\left(\hat{\theta}\right)$ is defined as follows

$$c\left(\hat{\theta}\right) \triangleq \min\left\{1, \frac{\mathcal{P}\left(\hat{\theta}\right)}{\delta}\right\}. \tag{B.7}$$

It is helpful to note that $c(\partial\mathcal{R}) = 0$ and $c(\partial\mathcal{R}_\delta) = 1$. The suggested projection operator satisfies the following property (reader is referred to [31] for the proof)

$$-\tilde{\theta}^T\Gamma^{-1}\text{Proj}\{\tau\} \leq -\tilde{\theta}^T\Gamma^{-1}\tau,\ \forall\hat{\theta} \in \mathcal{R}_\delta,\ \theta \in \mathcal{R}. \tag{B.8}$$

Appendix C

PE Proof for $\bar{W}_p(t)$

An auxiliary function $\Omega(t_0, t) \in \mathbb{R}^{4\times 4}$ is defined as follows

$$\Omega \triangleq \int_{t_0}^{t} \bar{W}_p^T(\tau)\bar{W}_p(\tau)d\tau. \tag{C.1}$$

To facilitate the proof the following expression is considered

$$\frac{d}{d\tau}\left\{\tilde{\theta}^T(\tau)\,\Omega(t_0,\tau)\,\tilde{\theta}(\tau)\right\} = \dot{\tilde{\theta}}^T(\tau)\,\Omega(t_0,\tau)\,\tilde{\theta}(\tau) + \tilde{\theta}^T(\tau)\,\frac{d}{d\tau}\{\Omega(t_0,\tau)\}\,\tilde{\theta}(\tau) + \tilde{\theta}^T(\tau)\,\Omega(t_0,\tau)\,\dot{\tilde{\theta}}(\tau). \tag{C.2}$$

From (C.2), the following expression can be obtained after integrating from t_0 to t and rearranging the terms

$$\begin{aligned}\int_{t_0}^{t} \tilde{\theta}^T(\tau)\,\Omega(t_0,\tau)\,\dot{\tilde{\theta}}(\tau)\,d\tau &= \tilde{\theta}^T(t)\,\Omega(t_0,t)\,\tilde{\theta}(t) - \tilde{\theta}^T(t_0)\,\Omega(t_0,t_0)\,\tilde{\theta}(t_0) \\ &\quad - \int_{t_0}^{t} \dot{\tilde{\theta}}^T(\tau)\,\Omega(t_0,\tau)\,\tilde{\theta}(\tau)\,d\tau - \int_{t_0}^{t} \tilde{\theta}^T(\tau)\,\frac{d}{d\tau}\{\Omega(t_0,\tau)\}\,\tilde{\theta}(\tau)\,d\tau\end{aligned} \tag{C.3}$$

After utilizing the following facts

$$\begin{aligned}\Omega(t_0,t_0) &= 0_4 \\ \Omega^T(t_0,\tau) &= \Omega(t_0,\tau) \\ \frac{d}{d\tau}\{\Omega(t_0,\tau)\} &= \bar{W}_p^T(\tau)\bar{W}_p(\tau),\end{aligned} \tag{C.4}$$

the expression in (C.3) can be rearranged as follows

$$\tilde{\theta}^T(t)\,\Omega(t_0,t)\,\tilde{\theta}(t) = 2\int_{t_0}^{t} \tilde{\theta}^T(\tau)\,\Omega(t_0,\tau)\,\dot{\tilde{\theta}}(\tau)\,d\tau + \int_{t_0}^{t} \tilde{\theta}^T(\tau)\,\bar{W}_p^T(\tau)\bar{W}_p(\tau)\tilde{\theta}(\tau)\,d\tau \tag{C.5}$$

where $0_4 \in \mathbb{R}^{4\times 4}$ is a matrix of zeros. To further facilitate the proof, the following lemma is stated [93]:

Lemma 8 *Let $f(t)$ be a uniformly continuous function [92]. Then,*

$$\lim_{t\to+\infty} f(t) = 0 \Leftrightarrow \lim_{t\to+\infty} \int_{t}^{t+t'} f(\tau)\,d\tau = 0 \tag{C.6}$$

for any positive constant $t' \in \mathbb{R}$.

To utilize Lemma 8, a change of variables is applied to (C.5) by substituting t with $t_0 + T$. The following equation is obtained after applying a limit operation to the resulting equation

$$\begin{aligned}\lim_{t_0 \to +\infty} \tilde{\theta}^T (t_0 + T) \Omega (t_0, t_0 + T) \tilde{\theta} (t_0 + T) &= 2 \lim_{t_0 \to +\infty} \int_{t_0}^{t_0+T} \tilde{\theta}^T (\tau) \Omega (t_0, \tau) \dot{\tilde{\theta}} (\tau) d\tau \\ &+ \lim_{t_0 \to +\infty} \int_{t_0}^{t_0+T} \tilde{\theta}^T (\tau) \bar{W}_p^T (\tau) \bar{W}_p (\tau) \tilde{\theta} (\tau) d\tau\end{aligned} \tag{C.7}$$

Remark 1 *Utilizing the fact that* $\dot{\tilde{\theta}} (t) = - \dot{\hat{\theta}} (t)$*, the right-hand-side of (1.25) can be written as follows*

$$\dot{\tilde{\theta}} = -Proj \left\{ \alpha \Gamma \bar{W}_p^T B \bar{W}_p \tilde{\theta} \right\} \tag{C.8}$$

where (1.23) was utilized. From (A.12), it is clear that the term inside the bracket on the right-hand-side of (C.8) goes to zero. So, both $\dot{\hat{\theta}} (t)$ *and* $\dot{\tilde{\theta}} (t)$ *go to zero as* $t \to +\infty$*.*

After utilizing (1.29), (C.8), Lemma 8, and the fact that $\tilde{\theta} (t)$ is bounded, it is clear that the first term at the right-hand-side of (C.7) is equal to zero. After utilizing (A.12), Lemma 8, and the facts that $\bar{W}_p (\tau)$, $\tilde{\theta} (\tau)$ are bounded, it is clear that the second term at the right-hand-side of (C.7) is equal to zero. Thus the following expression can be obtained based on (C.7)

$$\lim_{t_0 \to +\infty} \tilde{\theta}^T (t_0 + T) \Omega (t_0, t_0 + T) \tilde{\theta} (t_0 + T) = 0. \tag{C.9}$$

After utilizing the fact that $\gamma_1 I_4 \leq \Omega (t_0, t_0 + T) \leq \gamma_2 I_4$ it is clear that

$$\left\| \tilde{\theta} (t) \right\| \to 0 \text{ as } t \to +\infty. \tag{C.10}$$

Appendix D

Proof of Theorem 2

To facilitate the proof, a nonnegative Lyapunov function $V(t) \in \mathbb{R}$ is defined as follows

$$V \triangleq \frac{1}{2}\tilde{\theta}_s^T \Gamma^{-1} \tilde{\theta}_s. \tag{D.1}$$

The time derivative of (D.1) is given as follows

$$\dot{V} = \frac{1}{2}\dot{\tilde{\theta}}_s^T \Gamma^{-1} \tilde{\theta}_s + \frac{1}{2}\tilde{\theta}_s^T \dot{\Gamma}^{-1} \tilde{\theta}_s + \frac{1}{2}\tilde{\theta}_s^T \Gamma^{-1} \dot{\tilde{\theta}}_s . \tag{D.2}$$

The expression in (D.2) can be written as follows

$$\dot{V} = \tilde{\theta}_s^T \Gamma^{-1} \dot{\tilde{\theta}}_s + \frac{1}{2}\tilde{\theta}_s^T \dot{\Gamma}^{-1} \tilde{\theta}_s. \tag{D.3}$$

After utilizing the time derivative of $\tilde{\theta}_s$ given in (2.25), (D.3) can be rewritten as follows

$$\dot{V} = -\tilde{\theta}_s^T \Gamma^{-1} \dot{\hat{\theta}}_s + \frac{1}{2}\tilde{\theta}_s^T \dot{\Gamma}^{-1} \tilde{\theta}_s. \tag{D.4}$$

After substituting (2.41) and (2.45) in (D.4), the following expression is obtained

$$\dot{V} = -\tilde{\theta}_s^T \Gamma^{-1} \text{Proj}\left\{\alpha \Gamma \bar{W}_s^T \tilde{p}_s\right\} + \tilde{\theta}_s^T \bar{W}_s^T \bar{W}_s \tilde{\theta}_s. \tag{D.5}$$

After utilizing the property of the projection given in (2.47), $\dot{V}(t)$ can be upper bounded as follows

$$\dot{V} \leq -\alpha \tilde{\theta}_s^T \bar{W}_s^T \tilde{p} + \tilde{\theta}_s^T \bar{W}_s^T \bar{W}_s \tilde{\theta}_s. \tag{D.6}$$

It should be noted that, the expression (2.26) can be rearranged as follows

$$\bar{W}_s \tilde{\theta}_s = B^{-1} \tilde{p}_s - S. \tag{D.7}$$

Based on (2.3), (2.7), (2.9), and the definition of $B(t)$ in (2.24), it is easy to see that the denominators of the entries of $B(t)$ are equal to $z_{si}(t) \, \forall i = 1, .., n$; thus, from

(2.13) we can conclude that $B^{-1}(t)$ exists. After utilizing (D.7), the expression in (D.6) can be rewritten as follows

$$\begin{aligned} \dot{V} \leq & - \alpha(\tilde{p}_s^T B^{-T} - S^T)\tilde{p}_s \\ & + (\tilde{p}_s^T B^{-T} - S^T)(B^{-1}\tilde{p}_s - S). \end{aligned} \tag{D.8}$$

The right hand side of (D.8) can be upper bounded as follows

$$\begin{aligned} \dot{V} \leq & - \alpha\bar{\varepsilon}_s\tilde{p}_s^T\tilde{p}_s + \bar{\rho}_s\tilde{p}_s^T\tilde{p}_s + \alpha S^T\tilde{p}_s \\ & - \tilde{p}_s^T B^{-T} S - S^T B^{-1}\tilde{p}_s + S^T S \end{aligned} \tag{D.9}$$

where the definition of $B\left(t\right)$ in (2.24) is utilized along with (1.13), (2.43) and (2.44). After substituting (2.42) in (D.9), the following inequality can be written

$$\dot{V} \leq -\bar{\varepsilon}_s \left\|\tilde{p}_s\right\|^2 + S^T(\alpha I_{3n} - 2B^{-1})\tilde{p}_s + \left\|S\right\|^2. \tag{D.10}$$

After utilizing (2.3)-(2.9), (2.24) and (2.42), the following expression is obtained

$$\dot{V} \leq -\bar{\varepsilon}_s \left\|\tilde{p}_s\right\|^2 + \delta_1 \left\|S\right\| \left\|\tilde{p}_s\right\| + \left\|S\right\|^2 ; \quad \delta_1 \in \mathbb{R}^+. \tag{D.11}$$

After utilizing Young's inequality, (D.11) can be further simplified as follows

$$\dot{V} \leq -\bar{\varepsilon}_s \left\|\tilde{p}_s\right\|^2 + \delta_1\delta_2 \left\|S\right\|^2 + \frac{\delta_1}{\delta_2}\left\|\tilde{p}_s\right\|^2 + \left\|S\right\|^2 \tag{D.12}$$

where $\delta_2 \in \mathbb{R}$ is a positive constant. After simplifying (D.12), the following inequality is obtained

$$\dot{V} \leq -\beta_1 \left\|\tilde{p}_s\right\|^2 + \beta_2 \left\|S\right\|^2 ; \quad \beta_1, \beta_2 \in \mathbb{R}^+. \tag{D.13}$$

After integrating (D.13), the following expression can be obtained

$$\beta_1 \int_{t_0}^{\infty} \left\|\tilde{p}_s\right\|^2 d\tau \leq V\left(t_0\right) - V(\infty) + \beta_2 \int_{t_0}^{\infty} \left\|S\right\|^2 d\tau. \tag{D.14}$$

Since, $S(t) \in \mathcal{L}_2$ (see Appendix E), the following inequality can be written

$$\int_{t_0}^{\infty} \left\|S\right\|^2 d\tau \leq \sigma_1 ; \qquad \sigma_1 \in \mathbb{R}^+. \tag{D.15}$$

After utilizing (D.15), the inequality given in (D.14) can be rewritten as follows

$$\beta_1 \int_{t_0}^{\infty} \|\tilde{p}_s\|^2 \, d\tau < V(t_0) - V(\infty) + \beta_2 \sigma_1. \tag{D.16}$$

From (D.1) and (D.13), it can be concluded that $V(t)$ is bounded. From (D.16), it is clear that $\tilde{p}_s(t) \in \mathcal{L}_2 \cap \mathcal{L}_\infty$. Since $z_{si}(t)$ is bounded, from (2.7), (2.9), and the fact that θ_{si} is constant $\forall i$, it follows that $\Pi(\cdot) \in \mathcal{L}_\infty$. Therefore, from (2.8), it can easily be seen that $W(\cdot) \in \mathcal{L}_\infty$. Since the projection strategy utilized in (2.37) and (2.41) ensures that $\hat{\theta}_c(t), \hat{\theta}_s(t) \in \mathcal{L}_\infty$; therefore, it follows that $\tilde{\theta}_c(t), \tilde{\theta}_s(t) \in \mathcal{L}_\infty$. Thus, from the definitions given in (2.22)-(2.24), and (2.26), it is clear that $B(t)$ is bounded and $\bar{W}_s(t)$, $W_s(\cdot) \in \mathcal{L}_\infty$. Since $\Gamma(t)$ is bounded (see Remark 2), $\bar{W}_s(t)$, $\tilde{p}_s(t) \in \mathcal{L}_\infty$ and $\tilde{p}_s(t) \in \mathcal{L}_2$, from (2.41), it is clear that $\dot{\hat{\theta}}_s(t) \in \mathcal{L}_2 \cap \mathcal{L}_\infty$; hence, the time derivative of (2.25) can be used to show that $\dot{\tilde{\theta}}_s(t) \in \mathcal{L}_\infty$. Since $\bar{W}_s(t) \in \mathcal{L}_\infty$, it can be concluded that upon the satisfaction of the PE condition given in (2.49), $\left\|\tilde{\theta}_s(t)\right\| \to 0$ as $t \to \infty$ [49].

Appendix E

Proof for $S(t) \in \mathcal{L}_2$

Proof. To facilitate the proof, a nonnegative Lyapunov function, denoted by $V_c(t) \in \mathbb{R}$, is defined as follows

$$V_c \triangleq \frac{1}{2}\tilde{\theta}_c^T \Gamma_c^{-1} \tilde{\theta}_c. \tag{E.1}$$

Using a similar analysis as in Appendix D, the time derivative of (E.1) can be shown to be upper-bounded as follows

$$\dot{V}_c \leq -\bar{\varepsilon}_c \left\| \tilde{p}_c \right\|^2. \tag{E.2}$$

At the points of discontinuity of $\Gamma_c(t)$ the following expression can be written

$$V_c(t_m^+) - V_c(t_m) = \frac{1}{2}\tilde{\theta}_c^T \left[\Gamma_c^{-1}(t_m^+) - \Gamma_c^{-1}(t_m) \right] \tilde{\theta}_c \tag{E.3}$$

Since $\Gamma_c^{-1}(t_m^+) = \eta_0^{-1} I_{16}$ and $\Gamma_c^{-1}(t_m) \geq \eta_0^{-1} I_{16}$, it follows that

$$V_c(t_m^+) - V_c(t_m) \leq 0. \tag{E.4}$$

It can be easily inferred from (E.1) that $V_c(t) \geq 0 \quad \forall t \geq 0$; thus, the time integral of (E.2) can be used to show that $\tilde{p}_c(t) \in \mathcal{L}_2 \cap \mathcal{L}_\infty$. The derivative of the estimation error signal $\tilde{\theta}_c(t)$ can be written as follows

$$\dot{\tilde{\theta}}_c = -\alpha_c \Gamma_c W_c^T \tilde{p}_c \tag{E.5}$$

where (2.37) was utilized. It should be noted that the adaptive law with the projection algorithm retains all the properties of the adaptive law without the projection algorithm [49]. After substituting (2.35) into (E.5), the following expression is obtained

$$\dot{\tilde{\theta}}_c = -\alpha_c \Gamma_c W_c^T F W_c \tilde{\theta}_c. \tag{E.6}$$

The parameter error equation given in (E.6) and (2.35) can be written as follows [49]

$$\dot{\tilde{\theta}}_c = A\tilde{\theta}_c \tag{E.7}$$

$$\tilde{p}_c = C^T \tilde{\theta}_c \tag{E.8}$$

where $A(t) \in \mathbb{R}^{16\times 16}$, and $C(t) \in \mathbb{R}^{16\times 3m}$ are defined as follows

$$A = -\alpha_c \Gamma_c W_c^T F W_c \tag{E.9}$$

$$C^T = F W_c. \tag{E.10}$$

The time derivative of (E.1) can now be written as follows

$$\dot{V}_c = \frac{1}{2}\dot{\tilde{\theta}}_c^T G\tilde{\theta}_c + \frac{1}{2}\tilde{\theta}_c^T \dot{G}\tilde{\theta}_c + \frac{1}{2}\tilde{\theta}_c^T G\,\dot{\tilde{\theta}}_c \tag{E.11}$$

where $G(t) = \Gamma_c^{-1}(t)$. After utilizing (E.7), the expression given in (E.11) can be rewritten as follows

$$\dot{V}_c = \frac{1}{2}\tilde{\theta}_c^T \left[GA + A^T G + \dot{G}\right]\tilde{\theta}_c. \tag{E.12}$$

The inequality given in (E.2), can be rewritten as

$$\dot{V}_c \leq -\bar{\varepsilon}_c \tilde{\theta}_c^T C C^T \tilde{\theta}_c \tag{E.13}$$

where (E.8) was utilized. After utilizing (E.12) and (E.13) the following expression is obtained

$$\dot{G} + GA + A^T G + 2\bar{\varepsilon}_c C C^T \leq 0_{16} \tag{E.14}$$

where $0_{16} \in \mathbb{R}^{16\times 16}$ is a zero matrix. Since $\tilde{p}_c(t) \in \mathcal{L}_2 \cap \mathcal{L}_\infty$, similar boundedness statements as given in Appendix Dcan be used to show $F(t)$, $\hat{\theta}_c(t)$, $\tilde{\theta}_c(t) \in \mathcal{L}_\infty$ and $\dot{\hat{\theta}}_c(t) \in \mathcal{L}_2 \cap \mathcal{L}_\infty$. The pair (C, A) is *uniform complete observable (UCO)* (see Appendix F); hence, from (E.14) it can be shown that $\tilde{\theta}_c(t) \in \mathcal{L}_2$ [49]. After utilizing the previous boundedness statements, the expression given in (2.35) can be used to show $W_c(t)$ is bounded. From (2.36) it follows that $W_x(\cdot)$ is bounded; thus, $W_{xi}(\cdot)$ is bounded $\forall i$. The fact that $W_{xi}(\cdot)$ and $\Pi_{xi}(\cdot)$ are the functions of the same bounded signals, it follows that $\Pi_{xi}(\cdot) \in \mathcal{L}_\infty \forall i$. Since $\tilde{\theta}_c(t) \in \mathcal{L}_2$, $W_{xi}(\cdot)$, $\Pi_{xi}(\cdot)$, and $\hat{p}_{si}(t)$ are bounded $\forall i$ (see Remark 3), it can be concluded from (2.27) and (2.28) that $S_i(t) \in \mathcal{L}_2$ $\forall i$; hence, $S(t) \in \mathcal{L}_2$.

Appendix F

Proof for (C, A) is a UCO pair

To facilitate the proof, the following lemma is stated [49]:

Lemma 9 *Assume that there exists constants $\upsilon > 0$, $k_\upsilon \geq 0$ such that for all $t_0 \geq 0$, $K(t) \in \mathbb{R}^{n\times l}$ satisfies the inequality*

$$\int_{t_0}^{t_0+\upsilon} \|K(\tau)\|^2 \, d\tau \leq k_\upsilon \qquad \forall t \geq 0$$

Then (C, A), where $C(t) \in \mathbb{R}^{n\times l}$, $A(t) \in \mathbb{R}^{n\times n}$, is a UCO pair if and only if $(C, A + KC^T)$ is a UCO pair.

To utilize Lemma 9, $K(t) \in \mathbb{R}^{16\times 3m}$ is chosen as follows

$$K = \alpha_c \Gamma_c W_c^T. \tag{F.1}$$

After post-multiplying (F.1) by $C^T(t)$, the following expression is obtained

$$KC^T = \alpha_c \Gamma_c W_c^T F W_c \tag{F.2}$$

where (E.10) was utilized. Adding (E.9) and (F.2) results in the following expression

$$A + KC^T = 0. \tag{F.3}$$

The system that corresponds to the pair $(C, A + KC^T)$ is considered as follows [49]

$$\begin{aligned} \dot{Y} &= 0 \\ \tilde{p}_c &= C^T Y = F W_c Y \end{aligned} \tag{F.4}$$

where $Y(t) \in \mathbb{R}^{16}$. The observability grammian of (F.4) is given as follows

$$\Upsilon(t, t+T) = \int_t^{t+T} W_c^T F^T F W_c d\tau. \tag{F.5}$$

Since, from (2.34), $F(t)$ is symmetric and bounded (see Appendix E), it follows that upon the satisfaction of the following PE condition

$$\gamma_3 I_{16} \leq \int_{t_0}^{t_0+T} W_c^T(\tau) W_c(\tau) d\tau \leq \gamma_4 I_{16} \tag{F.6}$$

where $\gamma_3,\ \gamma_4 \in \mathbb{R}^+$, the grammian matrix $\Upsilon(t, t+T)$ is positive definite for $T \in \mathbb{R}^+\ \forall t \geq 0$ [49]; thus, it can be inferred that (F.4) is UCO which implies (C, A) is UCO.

Appendix G

Proof of Theorem 3

To facilitate the proof[11], a nonnegative Lyapunov function $V(t) \in \mathbb{R}$ is defined as follows

$$V = \frac{1}{2}\tilde{q}_{f\varepsilon}^2 + \frac{1}{2}\tilde{\theta}^T\tilde{\theta}. \tag{G.1}$$

The time derivative of (G.1) can be obtained as follows

$$\dot{V} = \tilde{q}_{f\varepsilon}\ \dot{\tilde{q}}_{f\varepsilon} + \tilde{\theta}^T\ \dot{\tilde{\theta}}\ . \tag{G.2}$$

After utilizing the time derivative of (3.36), the expression given in (G.2) can be written as follows

$$\dot{V} = \tilde{q}_{f\varepsilon}\ \dot{\tilde{q}}_{f\varepsilon} + \tilde{\theta}^T\ \dot{\hat{\theta}}\ . \tag{G.3}$$

After substituting (3.31) into (G.3), the following expression is obtained

$$\dot{V} = \tilde{q}_{f\varepsilon}\ \dot{\tilde{q}}_{f\varepsilon} + \tilde{\theta}^T \text{Proj}\{-\tilde{q}_{f\varepsilon}\phi^*\}. \tag{G.4}$$

It should be noted that an adaptive law with the projection algorithm defined on a convex set retains all the properties of the adaptive law without the projection algorithm [49]. The projection strategy given in (3.32) is on the cube Θ (*i.e.*, a convex set); hence, the expression given in (G.4) can be written as follows

$$\dot{V} = \tilde{q}_{f\varepsilon}\ \dot{\tilde{q}}_{f\varepsilon} - \tilde{\theta}^T\tilde{q}_{f\varepsilon}\phi^*. \tag{G.5}$$

The expression given in (G.5) is rearranged as follows

$$\dot{V} = \tilde{q}_{f\varepsilon}\left[\dot{\tilde{q}}_{f\varepsilon} - \tilde{\theta}^T\phi^*\right]. \tag{G.6}$$

Two different cases are considered, Case I when $|\tilde{q}_f| \leq \varepsilon$, and Case II when $\forall\, |\tilde{q}_f| > \varepsilon$.
Case I) From Remark 7 it follows that

$$\dot{V} = 0 \qquad \forall\, |\tilde{q}_f| \leq \varepsilon. \tag{G.7}$$

[11]The proof follows the concept outlined in [55]. We include it in a detailed manner for the sake of completeness.

Case II) Also, from Remark 7 and (G.6), the following expression can be obtained

$$\dot{V} = \tilde{q}_{f\varepsilon}\left[\dot{\tilde{q}}_f - \tilde{\theta}^T\phi^*\right] \qquad \forall\, |\tilde{q}_f| > \varepsilon. \tag{G.8}$$

After substituting (3.30) into (G.8), the following expression is obtained

$$\dot{V} = \tilde{q}_{f\varepsilon}\left[-\alpha\tilde{q}_{f\varepsilon} + \hat{q} - q - a^*\text{sat}(r) - \tilde{\theta}^T\phi^*\right]. \tag{G.9}$$

The inequality given in (G.9) can be rearranged as follows

$$\dot{V} = -\alpha\tilde{q}_{f\varepsilon}^2 + \tilde{q}_{f\varepsilon}\left[\hat{q} - q - \tilde{\theta}^T\phi^* - a^*\text{sat}(r)\right]. \tag{G.10}$$

Now two distinct sub-cases of Case II are considered: (a) when $\tilde{q}_f > \varepsilon$, and (b) when $\tilde{q}_f < -\varepsilon$.

(a) When $\tilde{q}_f > \varepsilon$, from (3.28) and (3.29) it follows that $\tilde{q}_{f\varepsilon} > 0$ and $\text{sat}(r) = \text{sgn}(\tilde{q}_f) = 1$. After utilizing (G.10), $\dot{V}(t)$ can be written as follows

$$\dot{V} = -\alpha\tilde{q}_{f\varepsilon}^2 + \tilde{q}_{f\varepsilon}\left[\hat{q} - q - \tilde{\theta}^T\phi^* - a^*\right]. \tag{G.11}$$

It follows from (G.11) that $\dot{V}(t) \leq 0$ if the following inequality holds

$$a^* \geq \hat{q} - q - \tilde{\theta}^T\phi^* \qquad \forall\theta \in \Theta_s. \tag{G.12}$$

Therefore, we choose to maximize $a^*(t)$ as follows

$$a^* = \max_{\theta\in\Theta_s}[\hat{q} - q - \tilde{\theta}^T\phi^*] \qquad \text{for any } \phi^*. \tag{G.13}$$

Since, $a^*(t)$ is like a gain in (3.30), we seek to find $\phi^*(t)$ so that $a^*(t)$ is minimized; thus, $a^*(t)$ is chosen as follows

$$a^* = \min_{\phi\in\mathbb{R}^3}\max_{\theta\in\Theta_s}[\hat{q} - q - \tilde{\theta}^T\phi^*]. \tag{G.14}$$

(b) When $\tilde{q}_f < -\varepsilon$, from (3.28) and (3.29) it follows that $\tilde{q}_{f\varepsilon} < 0$ and $\text{sat}(r) = \text{sgn}(\tilde{q}_f) = -1$. After utilizing (G.10), $\dot{V}(t)$ can be written as follows

$$\dot{V} = -\alpha\tilde{q}_{f\varepsilon}^2 + \tilde{q}_{f\varepsilon}\left[\hat{q} - q - \tilde{\theta}^T\phi^* + a^*\right]. \tag{G.15}$$

From (G.15) it follows that $\dot{V}(t) \leq 0$ if the following inequality holds

$$a^* \geq q - \hat{q} + \tilde{\theta}^T \phi^* \qquad \forall \theta \in \Theta_s. \tag{G.16}$$

Following along the same lines as in (a), the following expression can be written

$$a^* = \min_{\phi \in \mathbb{R}^3} \max_{\theta \in \Theta_s} [q - \hat{q} + \tilde{\theta}^T \phi^*]. \tag{G.17}$$

After combining (G.14) and (G.17), the following expression is obtained

$$a^* = \min_{\phi \in \mathbb{R}^3} \max_{\theta \in \Theta_s} \text{sat}(r) \left[\hat{q} - q - \tilde{\theta}^T \phi^* \right]. \tag{G.18}$$

After utilizing (G.12) and (G.16) the following inequality can be obtained

$$\text{sat}(r) \left[\hat{q} - q - \tilde{\theta}^T \phi^* \right] - a^* \leq 0. \tag{G.19}$$

The expression given in (G.11) can be rewritten as follows

$$\dot{V} = -\alpha \tilde{q}_{f\varepsilon}^2 + \tilde{q}_{f\varepsilon} \text{sat}(r) \{ \text{sat}(r) [\hat{q} - q - \tilde{\theta}^T \phi^*] - a^* \} \tag{G.20}$$

Thus, after utilizing (G.19), and the fact that $\tilde{q}_{f\varepsilon} \text{sat}(r) \geq 0$ when $|\tilde{q}_f| > \varepsilon$, $\dot{V}(t)$ can be upper bounded as follows

$$\dot{V} \leq -\alpha \tilde{q}_{f\varepsilon}^2 \qquad \forall \, |\tilde{q}_f| > \varepsilon. \tag{G.21}$$

After integrating (G.21), the following inequality can be obtained

$$\alpha \int_{t_0}^{\infty} \tilde{q}_{f\varepsilon}^2 \, d\tau < V(t_0) - V(\infty). \tag{G.22}$$

From (G.1), (G.7), and (G.21), it can be concluded that $V(t) \in \mathcal{L}_\infty$. From (G.22), it is clear that $\tilde{q}_{f\varepsilon}(t) \in \mathcal{L}_2 \cap \mathcal{L}_\infty$; thus, from (3.29), it can be concluded that $\tilde{q}_f(t) \in \mathcal{L}_\infty$. Since the projection strategy given in (3.32) ensures $\hat{\theta}(t) \in \Theta_s$; thus, it follows that $\hat{\theta}(t) \in \mathcal{L}_\infty$. Hence, from (3.22), it follows that $\hat{q}(\cdot) \in \mathcal{L}_\infty$. Since $a^*(t)$ is a function of the bounded signals, and $q(\cdot)$ is a measurable bounded signal, from (3.30), it follows that $\dot{\tilde{q}}_f \, (t) \in \mathcal{L}_\infty$. It is clear from the projection strategy that $\dot{\hat{\theta}} \, (t) \in \mathcal{L}_\infty$; thus, from (3.36), $\dot{\tilde{\theta}} \, (t) \in \mathcal{L}_\infty$.

Appendix H

Proof of Theorem 4

To facilitate the proof[12], without loss of generality, we assume $\beta\left(\Pi\left(t_2\right)\right) = 1$ *i.e.*, $q\left(\theta, \Pi\left(t_2\right)\right)$ is convex on Θ_s[13]. Thus, the expression given in (3.47) can be rewritten as follows

$$q(\hat{\theta}\left(t_1\right), \Pi\left(t_2\right)) - q\left(\theta, \Pi\left(t_2\right)\right) \geq \bar{\varepsilon} \tag{H.1}$$

where $\bar{\varepsilon} = \varepsilon_u \left\| \hat{\theta}(t_1) - \theta \right\|$. To further facilitate the proof, we define a region of convergence as follows

$$\Omega_\varepsilon = \{d : V\left(d\right) \leq \gamma\} \tag{H.2}$$

where

$$d = [\tilde{q}_{f\varepsilon} \quad \tilde{\theta}^T]^T \tag{H.3}$$

and $V(\cdot)$ is the Lyapunov function defined in (G.1).

From the region of convergence, we know that if $d\left(t_1\right) \in \Omega_\varepsilon$ then $d\left(t\right)$ for all $t \geq t_1$ stays in Ω_ε. Also, $V(\cdot)$ is a Lyapunov function and its time derivative is always non-positive (see Appendix G); hence, we assume that $d(t_1) \notin \Omega_\varepsilon$. The proof of this theorem follows by showing that $V(\cdot)$ decreases by a finite amount over every interval of time until the trajectories reach Ω_ε.

If $d(t_1) \notin \Omega_\varepsilon$, from (H.2), it is clear that $V(\cdot) > \gamma$. Hence, after utilizing (G.1), (H.2), and (H.3), $V(\cdot)$ can be expressed as follows

$$V = \frac{1}{2}\tilde{q}_{f\varepsilon}^2 + \frac{1}{2}\tilde{\theta}^T\tilde{\theta} > \gamma. \tag{H.4}$$

From (H.4), it is clear that the following inequalities are not satisfied simultaneously

$$\left|\tilde{q}_{f\varepsilon}\left(t_1\right)\right| < \sqrt{\gamma} \tag{H.5}$$

$$\left\|\tilde{\theta}\left(t_1\right)\right\| < \sqrt{\gamma}. \tag{H.6}$$

[12]The proof follows the concept outlined in [64]. We include it in a detailed manner for the sake of completeness.

[13]A similar proof can be given if $\beta\left(\Pi\left(t_2\right)\right) = -1$, *i.e.*, $q(\cdot)$ is concave on Θ_s.

It can be seen that if the inequalities given in (H.5) and (H.6) are satisfied simultaneously, then $V(\cdot) \leq \gamma$ which is not true; thus, we have three possible cases as follows

$$\begin{aligned}
&1.\ |\tilde{q}_{f\varepsilon}(t_1)| > \sqrt{\gamma} \text{ or} \\
&2.\ \left\|\tilde{\theta}(t_1)\right\| > \sqrt{\gamma} \text{ or} \\
&3.\ |\tilde{q}_{f\varepsilon}(t_1)| > \sqrt{\gamma} \text{ and } \left\|\tilde{\theta}(t_1)\right\| > \sqrt{\gamma}.
\end{aligned}$$

If case 1 or case 3 holds, since $|\tilde{q}_{f\varepsilon}(t_1)| > \sqrt{\gamma}$, from Property 1 (see Appendix I) , it is clear that $V(\cdot)$ decreases. If case 2 holds, then we show in the following analysis that $|\tilde{q}_{f\varepsilon}(t)|$ becomes large for some $t > t_1$ and $V(\cdot)$ decreases.

After taking the square of the right-hand side of (H.1), the following inequality can be obtained

$$\bar{\varepsilon}^2 \geq \varepsilon_u^2 \gamma. \tag{H.7}$$

Substituting (3.48) into (H.7) results the following inequality

$$\bar{\varepsilon}^2 \geq 8\varepsilon c_1 \tag{H.8}$$

We show that if (H.8) holds, then there exists a time $t_3 \in [t_2, t_2 + T_1]$ such that

$$|\tilde{q}_{f\varepsilon}(t_3)| > \min\left\{1, \bar{\delta}\right\} \tag{H.9}$$

where

$$\bar{\delta} = \min\left\{\frac{\bar{\varepsilon}}{2c_2}, \frac{\bar{\varepsilon}^2 - 4\varepsilon c_1}{2\bar{\varepsilon}c_2 + 4c_1}\right\} \tag{H.10}$$

where

$$c_2 = L_2 B_\phi T_0 + \alpha \quad ; \qquad T_1 = \frac{\bar{\varepsilon} - \bar{\delta} c_2}{c_1}. \tag{H.11}$$

We prove by contradiction that (H.9) holds. To facilitate the proof, we consider the following inequality

$$|\tilde{q}_{f\varepsilon}(t_2 + \tau)| < \min\left\{1, \bar{\delta}\right\} \ \forall \tau \in [0, T_1]. \tag{H.12}$$

The expression given in (3.30) can be rewritten as follows

$$\begin{aligned}\dot{\tilde{q}}_f(t_2+\tau) &\geq -\alpha \min\left\{1,\bar{\delta}\right\} + q(\hat{\theta},\Pi\left(t_2+\tau\right)) \\ &\quad -q(\theta,\Pi\left(t_2+\tau\right)) - a^{*}\text{sat}(r). \end{aligned} \tag{H.13}$$

where (H.12) was utilized. We seek to establish lower bounds for $[q(\hat{\theta},\Pi\left(t_2+\tau\right)) - q(\theta,\Pi\left(t_2+\tau\right))]$ and $-a^{*}\text{sat}(r)$ in (H.13) in order to prove that $\tilde{q}_{f\varepsilon}(t)$ becomes large over $[t_2, t_2+T_1]$. From Assumption 5, it follows that

$$\left|q\left(\theta+\Delta\theta,\Pi\left(t_2\right)\right) - q\left(\theta,\Pi\left(t_2\right)\right)\right| \leq L_2\left\|\Delta\theta\right\|. \tag{H.14}$$

After integrating (3.31) from t_1 to t_2, the following expression is obtained

$$\hat{\theta}\left(t_2\right) - \hat{\theta}\left(t_1\right) = \int_{t_1}^{t_2} -\tilde{q}_{f\varepsilon}\left(\sigma\right)\phi^{*}\left(\sigma\right)d\sigma. \tag{H.15}$$

After taking the norm on both the sides of (H.15), the following inequality can be obtained

$$\left\|\hat{\theta}\left(t_2\right) - \hat{\theta}\left(t_1\right)\right\| \leq \int_{t_1}^{t_2} \left\|\tilde{q}_{f\varepsilon}\left(\sigma\right)\right\|\left\|\phi^{*}\left(\sigma\right)\right\|d\sigma. \tag{H.16}$$

The left-hand side of (H.16) can be upper bounded as follows

$$\left\|\hat{\theta}\left(t_2\right) - \hat{\theta}\left(t_1\right)\right\| \leq \min\left\{1,\bar{\delta}\right\}L_{\phi}T_0 \tag{H.17}$$

where (H.12), Remark 9, and the fact that $T_0 \geq t_2 - t_1$ were utilized. After utilizing (H.14) and (H.17), the following inequality can be obtained

$$\left|q(\hat{\theta}\left(t_2\right),\Pi\left(t_2\right)) - q(\hat{\theta}\left(t_1\right),\Pi\left(t_2\right))\right| \leq L_2 \min\left\{1,\bar{\delta}\right\}L_{\phi}T_0. \tag{H.18}$$

From (H.18), it follows that

$$-L_2 \min\left\{1,\bar{\delta}\right\}L_{\phi}T_0 \leq q(\hat{\theta}\left(t_2\right),\Pi\left(t_2\right)) - q(\hat{\theta}\left(t_1\right),\Pi\left(t_2\right)). \tag{H.19}$$

After adding (H.1) and (H.19), the following expression is obtained

$$\bar{\varepsilon} - L_2 \min\left\{1,\bar{\delta}\right\}L_{\phi}T_0 \leq q(\hat{\theta}\left(t_2\right),\Pi\left(t_2\right)) - q\left(\theta,\Pi\left(t_2\right)\right). \tag{H.20}$$

From Assumption 4, it follows that

$$\|\Pi(t_2+\tau)-\Pi(t_2)\| \leq L_1\tau \qquad \forall \tau \in [0, T_1]. \tag{H.21}$$

Thus, the following inequalities can be obtained

$$\begin{aligned} &|q(\theta, \Pi(t_2+\tau)) - q(\theta, \Pi(t_2))| \\ &\leq L_2(\|\Pi(t_2+\tau)-\Pi(t_2)\|) \qquad \text{(H.22)} \\ &\leq L_2 L_1 \tau. \qquad \text{(H.23)} \end{aligned}$$

From (H.22) and (H.23), the following expression is obtained

$$q(\theta, \Pi(t_2+\tau)) - q(\theta, \Pi(t_2)) \leq L_2 L_1 \tau \tag{H.24}$$

which can be rewritten as follows

$$q(\theta, \Pi(t_2)) - q(\theta, \Pi(t_2+\tau)) \geq -L_2 L_1 \tau. \tag{H.25}$$

After combining (H.17), (H.21), and Assumption 5, the following expression can be obtained

$$\begin{aligned} &\left| q(\hat{\theta}(t_2+\tau), \Pi(t_2+\tau)) - q(\hat{\theta}(t_2), \Pi(t_2)) \right| \\ &\leq L_2 L_1 \tau + L_2 L_\phi \tau \end{aligned} \tag{H.26}$$

where the fact that $\min(a,b) \leq a$ and $\min(a,b) \leq b$ was utilized. From (H.26), it follows that

$$\begin{aligned} -L_2 L_1 \tau - L_2 L_\phi \tau \;\leq\; & q(\hat{\theta}(t_2+\tau), \Pi(t_2+\tau)) \\ & -q(\hat{\theta}(t_2), \Pi(t_2)). \end{aligned} \tag{H.27}$$

After adding (H.25) and (H.27), the following expression is obtained

$$\begin{aligned} -L_2(2L_1+L_\phi)\tau \;\leq\; & q(\hat{\theta}(t_2+\tau), \Pi(t_2+\tau)) \\ & -q(\theta, \Pi(t_2+\tau)) + q(\theta, \Pi(t_2)) \\ & -q(\hat{\theta}(t_2), \Pi(t_2)). \end{aligned} \tag{H.28}$$

After rearranging (H.28), the following expression can be obtained

$$-L_2\left(2L_1+L_\phi\right)\tau+q(\hat{\theta}\left(t_2\right),\Pi\left(t_2\right))-q(\theta,\Pi\left(t_2\right))$$
$$\leq q(\hat{\theta}\left(t_2+\tau\right),\Pi\left(t_2+\tau\right))-q\left(\theta,\Pi\left(t_2+\tau\right)\right). \tag{H.29}$$

Utilizing (H.20) and (H.29) results in the following expression

$$\bar{\varepsilon}-L_2\min\left\{1,\bar{\delta}\right\}L_\phi T_0-L_2\left(2L_1+L_\phi\right)\tau$$
$$\leq q(\hat{\theta}\left(t_2+\tau\right),\Pi\left(t_2+\tau\right))-q(\theta,\Pi\left(t_2+\tau\right)). \tag{H.30}$$

Thus, a lower bound on the term $[q(\hat{\theta},\Pi\left(t_2+\tau\right))-q(\theta,\Pi\left(t_2+\tau\right))]$ in (H.13) is established. Now, we seek to find a lower bound on the term $-a^*\mathrm{sat}(r)$ in (H.13). After changing the variable t_2 to $t_2+\tau$ and t_1 to t_2, the expression given in (H.17) can be rewritten as follows

$$\left\|\hat{\theta}\left(t_2+\tau\right)-\hat{\theta}\left(t_2\right)\right\|\leq\min\left\{1,\bar{\delta}\right\}L_\phi\tau. \tag{H.31}$$

After multiplying (H.31) by $\phi^*(t_2)$ and utilizing Remark 9, the following expression is obtained

$$\left|\phi^*\left(t_2\right)\left(\hat{\theta}\left(t_2+\tau\right)-\hat{\theta}\left(t_2\right)\right)\right|\leq\min\left\{1,\bar{\delta}\right\}L_\phi^2\tau. \tag{H.32}$$

From Property 3 (see Appendix K), it follows that

$$a_+^*(\hat{\theta}\left(t_2\right),\Pi\left(t_2\right))=0 \tag{H.33}$$

when $\beta(\Pi\left(t_2\right))=1$ where $a_+^*(\cdot)$ denotes $a^*(t)$ when $\tilde{q}_{f\varepsilon}>0$ (see Appendix D). From (3.33), the following expression is obtained

$$a_+^*(\hat{\theta}(t_2),\Pi(t_2))=\max\{\hat{q}_2-\phi^*(t_2)(\hat{\theta}(t_2)-\theta)\} \tag{H.34}$$

where

$$\hat{q}_2=q(\hat{\theta}(t_2),\Pi(t_2))-q(\theta,\Pi(t_2)). \tag{H.35}$$

At time instant $t_2+\tau$, the expression given in (H.34) can be written as follows

$$a_+^*(\hat{\theta}(t_2+\tau),\Pi(t_2+\tau))=\max\{\hat{q}_{2\tau}-\phi^*(t_2+\tau)(\hat{\theta}(t_2+\tau)-\theta)\} \tag{H.36}$$

where

$$\hat{q}_{2\tau} = q(\hat{\theta}(t_2+\tau), \Pi(t_2+\tau)) - q(\theta, \Pi(t_2+\tau)). \tag{H.37}$$

Since $\phi^*(t_2+\tau)$ results in the minimum value of $a_+^*(\hat{\theta}(t_2+\tau), \Pi(t_2+\tau))$, the left-hand side of (H.36) can be upper bounded as follows

$$a_+^*(\hat{\theta}(t_2+\tau), \Pi(t_2+\tau)) \leq \max\{\hat{q}_{2\tau} - \phi^*(t_2)(\hat{\theta}(t_2+\tau) - \theta)\} \tag{H.38}$$

After adding and subtracting the terms $\hat{q}_2$ and $\phi^*(t_2)\hat{\theta}(t_2)$ to the right-hand side of (H.38), and then simplifying it results in the following expression

$$\begin{aligned} a_+^*(\hat{\theta}(t_2+\tau), \Pi(t_2+\tau)) \quad \leq \quad & \max\{\hat{q}_{2\tau} - \hat{q}_2 \\ & -\phi^*(t_2)(\hat{\theta}(t_2+\tau) - \hat{\theta}(t_2))\} \\ & + \max\{\hat{q}_2 \\ & -\phi^*(t_2)(\hat{\theta}(t_2) - \theta)\} \end{aligned} \tag{H.39}$$

where the fact that $\max(a+b) \leq \max(a) + \max(b)$ was utilized. After utilizing (H.34), the expression given in (H.39) can be written as follows

$$\begin{aligned} a_+^*(\hat{\theta}(t_2+\tau), \Pi(t_2+\tau)) \quad \leq \quad & \max\{\hat{q}_{2\tau} - \hat{q}_2 \\ & -\phi^*(t_2)(\hat{\theta}(t_2+\tau) - \hat{\theta}(t_2))\} \\ & + a_+^*(\hat{\theta}(t_2), \Pi(t_2)). \end{aligned} \tag{H.40}$$

The expression given in (H.40) can be upper bounded as follows

$$\begin{aligned} a_+^*(\hat{\theta}(t_2+\tau), \Pi(t_2+\tau)) \quad \leq \quad & \max\{\hat{q}_{2\tau} - \hat{q}_2\} \\ & + \max\{-\phi^*(t_2) \\ & \times(\hat{\theta}(t_2+\tau) - \hat{\theta}(t_2))\} \\ & + a_+^*(\hat{\theta}(t_2), \Pi(t_2)). \end{aligned} \tag{H.41}$$

The expression given in (H.41) can be rewritten as follows

$$a_+^*(\hat{\theta}(t_2+\tau), \Pi(t_2+\tau)) \leq L_2\left(2L_1 + L_\phi\right)\tau + \min\left\{1, \bar{\delta}\right\} L_\phi^2 \tau \tag{H.42}$$

where (H.28), (H.32), (H.33), (H.35), and (H.37) were utilized. Since $\min\left\{1, \bar{\delta}\right\} \leq 1$, (H.42) can be rewritten as follows

$$\begin{aligned} a_{+}^{*}(\hat{\theta}(t_2+\tau), \Pi(t_2+\tau)) &\leq L_2\left(2L_1 + L_\phi\right)\tau + L_\phi^2\tau \\ &\leq \left(2L_2L_1 + L_2L_\phi + L_\phi^2\right)\tau. \end{aligned} \tag{H.43}$$

The inequality given in (H.43) is rewritten as follows

$$a_{+}^{*}(\hat{\theta}\left(t_2+\tau\right), \Pi\left(t_2+\tau\right))\text{sat}(r) \leq \left(2L_2L_1 + L_2L_\phi + L_\phi^2\right)\tau \tag{H.44}$$

where the fact that $\text{sat}(r) \leq 1$ was utilized. After multiplying both the sides of (H.44) by -1, and utilizing Property 2 (see Appendix J), the lower bound on the term $-a^*\text{sat}(r)$ in (3.30) is obtained as follows

$$\begin{aligned} &-a^*(\hat{\theta}\left(t_2+\tau\right), \Pi\left(t_2+\tau\right))\,\text{sat}(r) \\ &\quad \geq -(2L_2L_1 + L_2L_\phi + L_\phi^2)\tau. \end{aligned} \tag{H.45}$$

Now, the expression given in (H.13) can be rewritten as follows

$$\begin{aligned} \dot{\tilde{q}}_f(t_2+\tau) \;\geq\; & -\alpha \min\left\{1, \bar{\delta}\right\} + \bar{\varepsilon} - L_2 \min\left\{1, \bar{\delta}\right\} L_\phi T_0 \\ & -L_2\left(2L_1 + L_\phi\right)\tau \\ & -(2L_2L_1 + L_2L_\phi + L_\phi^2)\tau \end{aligned} \tag{H.46}$$

where (H.30) and (H.45) were utilized. After substituting (3.48) and (H.11) into (H.46), the following expression can be obtained

$$\dot{\tilde{q}}_f(t_2+\tau) \geq \bar{\varepsilon} - c_2 \min\left\{1, \bar{\delta}\right\} - c_1\tau. \tag{H.47}$$

Since $\min\left\{1, \bar{\delta}\right\} \leq \bar{\delta}$, $\dot{\tilde{q}}_f(t)$ can be lower bounded as follows

$$\dot{\tilde{q}}_f(t_2+\tau) \geq c_3 - c_1\tau \tag{H.48}$$

where

$$c_3 = \bar{\varepsilon} - c_2\bar{\delta}. \tag{H.49}$$

Integrating both the sides of (H.48) over $[0,\, T_1]$ where T_1 is defined in (H.11) results in the following expression

$$\int_0^{T_1} \dot{\tilde{q}}_f\left(t_2+\tau\right) d\tau \geq \left(c_3\tau - \frac{1}{2}c_1\tau^2\right)\Big|_0^{T_1}. \tag{H.50}$$

Simplifying the right-hand side of (H.50) results in the following expression

$$\left(c_3\tau - \frac{1}{2}c_1\tau^2\right)\Big|_0^{T_1} = \frac{1}{2}\frac{c_3^2}{c_1} \tag{H.51}$$

where (H.11) was utilized. After performing a change of variable $\rho = t_2 + \tau$ on the left-hand side of (H.50), the following expressions can be obtained

$$\begin{aligned}
\int_0^{T_1} \dot{\tilde{q}}_f\left(t_2+\tau\right) d\tau &= \int_{t_2}^{t_2+T_1} \dot{\tilde{q}}_f\left(\rho\right) d\rho && \text{(H.52)}\\
&= \tilde{q}_f\left(\rho\right)\big|_{t_2}^{t_2+T_1} && \text{(H.53)}\\
&= \tilde{q}_f\left(t_2+T_1\right) - \tilde{q}_f\left(t_2\right). && \text{(H.54)}
\end{aligned}$$

After combining (H.51) and (H.54), the expression given in (H.51) can be rewritten as follows

$$\tilde{q}_f\left(t_2+T_1\right) - \tilde{q}_f\left(t_2\right) \geq \frac{1}{2}\frac{c_3^2}{c_1}. \tag{H.55}$$

Taking $\tau = 0$ in (H.12) results in the following expression

$$-\min\left\{1, \bar{\delta}\right\} < \tilde{q}_{f\varepsilon}\left(t_2\right) < \min\left\{1, \bar{\delta}\right\} \tag{H.56}$$

The inequality given in (H.56) can be rewritten as follows

$$-\varepsilon - \min\left\{1, \bar{\delta}\right\} < \tilde{q}_f\left(t_2\right) < \varepsilon + \min\left\{1, \bar{\delta}\right\} \tag{H.57}$$

where (3.29) was utilized. After substituting (H.57) into (H.55), the following inequality can be written

$$\tilde{q}_f\left(t_2+T_1\right) \geq \frac{c_3^2}{2c_1} - \varepsilon - \min\left\{1, \bar{\delta}\right\}. \tag{H.58}$$

Since $\min(a,\, b) \leq a$ and $\min(a,\, b) \leq b$, from the definition of $\bar{\delta}$ given in (H.10), the following inequality can be obtained

$$\bar{\delta} \leq \frac{\bar{\varepsilon}^2 - 4\varepsilon c_1}{2\bar{\varepsilon} c_2 + 4c_1}. \tag{H.59}$$

After multiplying both the sides of (H.59) by the term $(2\bar{\varepsilon} c_2 + 4c_1)$, the following inequalities can be obtained

$$\begin{aligned} 2\bar{\delta}\bar{\varepsilon} c_2 + 4\bar{\delta} c_1 &\leq \bar{\varepsilon}^2 - 4\varepsilon c_1 \\ 4c_1 \left(\bar{\delta} + \varepsilon\right) &\leq \bar{\varepsilon}^2 - 2\bar{\delta}\bar{\varepsilon} c_2 \\ 2\left(\bar{\delta} + \varepsilon\right) &\leq \frac{\bar{\varepsilon}^2 - 2\bar{\delta}\bar{\varepsilon} c_2}{2c_1}. \end{aligned} \tag{H.60}$$

After adding and subtracting the term $\left(\bar{\delta} c_2\right)^2$ to the right-hand side of (H.60) results in the following expressions

$$\begin{aligned} \frac{\bar{\varepsilon}^2 - 2\bar{\delta}\bar{\varepsilon} c_2}{2c_1} &= \frac{\bar{\varepsilon}^2 - 2\bar{\delta}\bar{\varepsilon} c_2 + \left(\bar{\delta} c_2\right)^2 - \left(\bar{\delta} c_2\right)^2}{2c_1} \\ &= \frac{\left(\bar{\varepsilon} - \bar{\delta} c_2\right)^2 - \left(\bar{\delta} c_2\right)^2}{2c_1} \\ &= \frac{c_3^2 - \left(\bar{\delta} c_2\right)^2}{2c_1}. \end{aligned} \tag{H.61}$$

After utilizing (H.60) and (H.61), the following inequality can be obtained

$$\frac{\left(\bar{\delta} c_2\right)^2}{2c_1} + 2\left(\bar{\delta} + \varepsilon\right) \leq \frac{c_3^2}{2c_1}. \tag{H.62}$$

After utilizing (H.62), the inequality given in (H.58) can be written as follows

$$\begin{aligned} \tilde{q}_f\left(t_2 + T_1\right) &\geq \frac{\left(\bar{\delta} c_2\right)^2}{2c_1} + 2\left(\bar{\delta} + \varepsilon\right) - \varepsilon - \min\left\{1, \bar{\delta}\right\} \\ &\geq \frac{\left(\bar{\delta} c_2\right)^2}{2c_1} + \bar{\delta} + \varepsilon + \bar{\delta} - \min\left\{1, \bar{\delta}\right\} \\ &\geq \frac{\left(\bar{\delta} c_2\right)^2}{2c_1} + \bar{\delta} + \varepsilon \\ &\geq \bar{\delta} + \varepsilon. \end{aligned} \tag{H.63}$$

From (3.29), it can be seen that the expression given in (H.63) implies that $\tilde{q}_{f\varepsilon} \geq \bar{\delta}$ which contradicts (H.12); thus, it can be easily concluded that (H.9) must hold.

Thus, it was shown that if $V(t_1) > \gamma$, then one of the following inequalities hold

$$|\tilde{q}_{f\varepsilon}(t_3)| \geq \delta \min\left\{1, \bar{\delta}\right\} \quad \forall t_3 \in [t_1,\, t_1 + T_0 + T_1] \tag{H.64}$$

$$|\tilde{q}_{f\varepsilon}(t_1)| > \sqrt{\gamma}. \tag{H.65}$$

From Property 1 (see Appendix I), it follows that if (H.64) holds, then

$$V(t_3 + T_1') \leq V(t_3) - \frac{\alpha\delta^3}{3(M + \alpha\delta)} \tag{H.66}$$

where $T_1' = \delta/(M + \alpha\delta)$. Similarly, if (H.65) holds, from Property 1 (see Appendix I), it follows that

$$V(t_1 + T_2') \leq V(t_1) - \frac{\alpha\sqrt{\gamma}^3}{3(M + \alpha\sqrt{\gamma})} \tag{H.67}$$

where $T_2' = \sqrt{\gamma}/(M + \alpha\delta)$. Since $V(t)$ is a nonincreasing function, the following expression can be concluded from (H.66) and (H.67)

$$V(t_1 + T_3') \leq V(t_1) - \Delta V \qquad \forall V(t_1) > \gamma \tag{H.68}$$

where

$$\begin{aligned} T_3' &= \max\left\{T_0 + T_1 + T_1', T_0 + T_1 + T_2'\right\} \\ \Delta V &= \min\left\{\frac{\alpha\delta^3}{3(M + \alpha\delta)}, \frac{\alpha\sqrt{\gamma}^3}{3(M + \alpha\sqrt{\gamma})}\right\}. \end{aligned}$$

Thus, it is clear from (H.68) that $V(t)$ decreases by a finite amount over every interval T_3' until trajectories reach Ω_ε; hence, from (G.1), (H.2), and (H.3), it follows that $\|\tilde{\theta}(t)\| \leq \sqrt{\gamma}$ as $t \to \infty$.

Appendix I

Property 1

Property 1 *The property of the proposed min-max estimtor [64] states that if*

$$|\tilde{q}_{f\varepsilon}| \geq \bar{\gamma} \quad ; \qquad \bar{\gamma} \in \mathbb{R}^{+}. \tag{I.1}$$

then

$$V(t_1 + T') \leq V(t_1) - \frac{\alpha \bar{\gamma}^3}{3(M + \alpha\bar{\gamma})} \tag{I.2}$$

where $V(\cdot)$ is the Lyapunov function defined in (G.1) and

$$T' = \bar{\gamma}/(M + \alpha\bar{\gamma}) \tag{I.3}$$

$$M = \max\{|\psi(t)|\} \tag{I.4}$$

$$\psi = \hat{q} - q - a^* sat(r). \tag{I.5}$$

Proof. To facilitate the proof[14], the following lemma is stated [64]

Lemma 10 *For a given system of the following form*

$$\dot{p} = -k(t)p + s(t) \tag{I.6}$$

$$\dot{p}_m = -k_m p_m + s_m \tag{I.7}$$

where $k(t), k_m > 0$ and $|s(t)| \leq s_m \ \forall t \geq t_0$, if $p(t_0) \leq p_m(t_0) < 0$, $k(t) \leq k_m$, then $p(t) \leq p_m(t), \ \forall t \geq t_0$ where $p_m(t) \leq 0$.

Without loss of generality, (I.1) is rewritten as follows[15]

$$\tilde{q}_{f\varepsilon}(t_1) \leq -\bar{\gamma}. \tag{I.8}$$

From (3.30) and Remark 7, the following expression can be obtained

$$\dot{\tilde{q}}_{f\varepsilon} = -\alpha \tilde{q}_{f\varepsilon} + \psi(t) \tag{I.9}$$

[14]The proof of the property follows the concept outlined in [64]. We include it in a detailed manner for the sake of completeness.

[15]A similar proof can be shown for $\tilde{q}_{f\varepsilon}(t_1) \geq \bar{\gamma}$.

Since $\hat{q}(\cdot), q(\cdot) \in \mathcal{L}_\infty$ (see Appendix G)and $a^*(t)$ is a function of bounded signals, it follows that $\psi(t)$ is bounded as $|\psi(t)| \leq M$. To facilitate the proof, the following differential equation is considered

$$\dot{q}_m = -\alpha q_m + M \quad ; \qquad q_m(t_1) = -\bar{\gamma}. \tag{I.10}$$

From (I.8)-(I.10), and Lemma 10, the following inequality can be obtained

$$\tilde{q}_{f\varepsilon}(t_1 + \tau) \leq q_m(t_1 + \tau) \qquad \forall \tau \geq 0 \text{ and } q_m(t_1 + \tau) \leq 0. \tag{I.11}$$

After solving the differential equation given in (I.10), the solution $q_m(t)$ $\forall t \geq t_1$ can be obtained as follows

$$q_m(t_1 + \tau) = \left(-\frac{M}{\alpha} - \bar{\gamma} \right) e^{-\alpha \tau} + \frac{M}{\alpha}. \tag{I.12}$$

It should be noted that $\ddot{q}_m\ (t_1 + \tau) \leq 0\ \forall \tau \geq 0$; therefore, $q_m(t_1 + \tau)$ is a concave function of $\tau\ \forall \tau \geq 0$. After utilizing the gradient property of a concave function [55], the following inequality can be written

$$q_m(t_1 + \tau) \leq q_m(t_1) + \nabla q_{m_\tau}(t_1 + \tau - t_1) \tag{I.13}$$

where $\nabla q_{m_\tau} = (\partial q_m(t_1 + \tau)/\partial \tau)|_{\tau=0}$. The expression given in (I.13) can be rewritten as follows

$$q_m(t_1 + \tau) \leq -\bar{\gamma} + (M + \alpha \bar{\gamma})\tau. \tag{I.14}$$

After utilizing (I.11) and (I.14), $\tilde{q}_{f\varepsilon}(t_1 + \tau)$ can be upper bounded as follows

$$\tilde{q}_{f\varepsilon}(t_1 + \tau) \leq -\bar{\gamma} + (M + \alpha \bar{\gamma})\tau \qquad \forall \tau \geq 0. \tag{I.15}$$

Substituting $\tau = T' = \bar{\gamma}/(M + \alpha \bar{\gamma})$ in (I.15) results in the following inequality

$$\tilde{q}_{f\varepsilon}(t) \leq 0 \qquad \forall t \in [t_1, t_1 + T']. \tag{I.16}$$

After squaring, and then integrating both the sides of (I.15) over $[t_1 = 0, T']$, the following inequality is obtained

$$\int_{t_1}^{t_1 + T'} |\tilde{q}_{f\varepsilon}(\tau)|^2 \, d\tau \geq \frac{\bar{\gamma}^3}{3(M + \alpha \bar{\gamma})}. \tag{I.17}$$

After integrating (G.21) over $[t_1, t_1 + T']$, the following inequality can be obtained

$$V(t_1 + T') \leq V(t_1) - \frac{\bar{\gamma}^3}{3(M + \alpha\bar{\gamma})} \tag{I.18}$$

where (I.17) was utilized. Thus, Property 1 is established.

Appendix J

Property 2

Property 2 *The property states the following inequality [64]*

$$-a_{-}^{*}(\hat{\theta},\Pi) \leq a^{*} sat\left(\frac{\tilde{q}_f}{\varepsilon}\right) \leq a_{+}^{*}(\hat{\theta},\Pi) \tag{J.1}$$

where $a_{-}^{*}(\hat{\theta},\Pi)$ *denotes* $a^{*}(t)$ *when* $\tilde{q}_{f\varepsilon} < 0$*, and* $a_{+}^{*}(\hat{\theta},\Pi)$ *denotes* $a^{*}(t)$ *when* $\tilde{q}_{f\varepsilon} > 0$*.*

Proof. To facilitate the proof[16], first we prove the following left-hand side of the inequality given in (J.1)

$$-a_{-}^{*}(\hat{\theta},\Pi) \leq a^{*}\text{sat}\left(\frac{\tilde{q}_f}{\varepsilon}\right). \tag{J.2}$$

The solutions of the min-max optimization problem of the form given in (3.33)-(3.35) results in the following inequality [55]

$$a^{*} \geq 0 \qquad \forall\theta \in \Theta_s. \tag{J.3}$$

From (3.28), it follows that $\text{sat}\left(\frac{\tilde{q}_f}{\varepsilon}\right) \geq 0$ when $\tilde{q}_f \geq 0$; thus, the following inequalities are obtained

$$a^{*}\text{sat}\left(\frac{\tilde{q}_f}{\varepsilon}\right) \geq 0 \tag{J.4}$$

$$a^{*}\text{sat}\left(\frac{\tilde{q}_f}{\varepsilon}\right) \geq -a_{-}^{*}(\hat{\theta},\Pi) \tag{J.5}$$

where (J.3) was utilized. Thus, it can be concluded from (J.5) that if $\tilde{q}_f \geq 0$, then (J.2) holds.

If $\tilde{q}_f < 0$, from (3.29), it follows that $\tilde{q}_{f\varepsilon} < 0$. Also, from (3.28), it follows that $-1 \leq \text{sat}\left(\frac{\tilde{q}_f}{\varepsilon}\right) < 0$. Therefore, the following inequality can be obtained

$$a_{-}^{*}(\hat{\theta},\Pi)\text{sat}\left(\frac{\tilde{q}_f}{\varepsilon}\right) \geq -a_{-}^{*}(\hat{\theta},\Pi). \tag{J.6}$$

Hence, from (J.6), it can be concluded that (J.2) holds when $\tilde{q}_f < 0$. This proves (J.2) for any $\tilde{q}_f(t)$. Similar analysis can be utilized to prove the right-hand side inequality of (J.1). Thus, Property 2 is established.

[16]The proof of the property follows the concept outlined in [64]. We include it in a detailed manner for the sake of completeness.

Appendix K

Property 3

Property 3 *The property states the following [64]*

$$a_{-}^{*} = 0 \text{ if } \beta = -1 \tag{K.1}$$

$$a_{+}^{*} = 0 \text{ if } \beta = 1 \tag{K.2}$$

$$\beta a^{*} \tilde{q}_f \leq 0 \qquad \forall \beta. \tag{K.3}$$

Proof. The proof of the property follows the concept outlined in [64]. We include it in a detailed manner for the sake of completeness. From (3.44), it follows that $\beta = -1$ if q is concave; thus, the following expression can be obtained from the solutions of the min-max optimization problem given in (3.37)-(3.43)

$$a^{*} = 0 \qquad \forall \tilde{q}_f < 0 \tag{K.4}$$

which proves (K.1). Further, when $\tilde{q}_f > 0$, the following expression can be obtained

$$\beta a^{*} \tilde{q}_f \leq 0 \qquad \forall \tilde{q}_f > 0 \tag{K.5}$$

where (J.3) was utilized.

Similary, when $\beta = 1$, it follows that

$$a^{*} = 0 \qquad \forall \tilde{q}_f > 0 \tag{K.6}$$

which proves (K.2). After utilizing (J.3), the following expression can be obtained

$$\beta a^{*} \tilde{q}_f \leq 0 \qquad \forall \tilde{q}_f < 0. \tag{K.7}$$

Thus, from (K.5) and (K.7), it can be concluded that (K.3) holds. Hence, Property 3 is established.

Appendix L

Validity of Assumptions 4 and 5

The assumptions 4 and 5 are technical assumptions that are used for the proof of convergence as given in [64]. In general, it is not possible to ascertain whether these assumptions are realistic for the problem attacked in this paper; however, in this appendix we give an argument which gives confidence that the assumptions have some validity with regard to the estimation problem.

To facilitate the validity argument, we add and subtract $q(\theta_0 + \Delta\theta_0, \Pi)$ to the left-hand side of (3.16) to obtain the following expression

$$\begin{aligned} |q(\theta_0 + \Delta\theta_0, \Pi + \Delta\Pi) - q(\theta_0, \Pi)| &= |q(\theta_0 + \Delta\theta_0, \Pi + \Delta\Pi) \\ &\quad -q(\theta_0 + \Delta\theta_0, \Pi) \\ &\quad +q(\theta_0 + \Delta\theta_0, \Pi) \\ &\quad -q(\theta_0, \Pi)|. \end{aligned} \tag{L.1}$$

The left-hand side of (L.1) can be upper bounded as follows

$$\begin{aligned} |q(\theta_0 + \Delta\theta_0, \Pi + \Delta\Pi) - q(\theta_0, \Pi)| &\leq |q(\theta_0 + \Delta\theta_0, \Pi + \Delta\Pi) \\ &\quad -q(\theta_0 + \Delta\theta_0, \Pi)| \\ &\quad +|q(\theta_0 + \Delta\theta_0, \Pi) \\ &\quad -q(\theta_0, \Pi)| \end{aligned} \tag{L.2}$$

where triangle inequality was utilized. After utilizing the mean value theorem [93], the terms on the right-hand side of (L.2) can be written as follows

$$\begin{aligned} & q(\theta_0 + \Delta\theta_0, \Pi + \Delta\Pi) - q(\theta_0 + \Delta\theta_0, \Pi) \\ = \; & \frac{\partial q(\theta_0 + \Delta\theta_0, \upsilon_1)}{\partial \upsilon_1}|_{\upsilon_1 = \psi_1}(\Pi + \Delta\Pi - \Pi) \end{aligned} \tag{L.3}$$

where $\psi_1 \in [\Pi, \Pi + \Delta\Pi]$ and can be chosen as $\psi_1 = \Pi + \Delta\Pi - \rho_1(\Pi + \Delta\Pi - \Pi)$ with

$\rho_1 \in [0,1]$ and

$$\begin{aligned} & q(\theta_0 + \Delta\theta_0, \Pi) - q(\theta_0, \Pi) \\ = \; & \frac{\partial q(\upsilon_2, \Pi)}{\partial \upsilon_2}|_{\upsilon_2 = \psi_2}(\theta_0 + \Delta\theta_0 - \theta_0) \end{aligned} \tag{L.4}$$

where $\psi_2 \in [\theta_0, \theta_0 + \Delta\theta_0]$ and can be chosen as $\psi_2 = \theta_0 + \Delta\theta_0 - \rho_2(\theta_0 + \Delta\theta_0 - \theta_0)$ with $\rho_2 \in [0,1]$. From (3.11)-(3.14), it can be seen that $q(\cdot)$ is differentiable with respect to its arguments. Also, since the measurable position signals are assumed to be bounded (see Remark 2), we can utilize (L.2)-(L.4) to obtain the following expression can be obtained

$$|q(\theta_0 + \Delta\theta_0, \Pi + \Delta\Pi) - q(\theta_0, \Pi)| \leq L_2(\|\Delta\Pi\| + \|\Delta\theta_0\|) \tag{L.5}$$

where $L_2 \in \mathbb{R}$ is a positive constant. The expression given in (L.5) is same as the expression given in (3.16) in Assumption 5.

Similar argument can be given to show the validity of Assumption 4. To facilitate the argument, we define $t_\Delta \in \mathbb{R}$ as $t_1 \leq t_\Delta \leq t_2$. After utilizing the mean value theorem, the following expression can be obtained

$$\Pi(t_2) - \Pi(t_1) = \dot{\Pi}(t_\Delta)\,(t_2 - t_1)\,. \tag{L.6}$$

The left-hand side of (L.6) can be upper bounded as follows

$$\|\Pi(t_2) - \Pi(t_1)\| \leq \|\dot{\Pi}(t_\Delta)\|\,|\,(t_2 - t_1)\,|. \tag{L.7}$$

Since the position and velocity of the moving platform are assumed to be bounded then $\dot{\Pi}(t_\Delta)$ is bounded; hence, (L.7) can be written as follows

$$\|\Pi(t_1) - \Pi(t_2)\| \leq L_1|t_1 - t_2| \tag{L.8}$$

where $L_1 \in \mathbb{R}$ is a positive constant. It can be seen that (L.8) is the same expression as given in (3.15) in Assumption 4.

Appendix M

Implementable Form of the Filtered Signal $Q_f(t)$

In order to obtain the implementable form of (4.21), an auxiliary filter signal $\zeta(t) \in \mathbb{R}$ is designed as follows

$$\dot{\zeta} \triangleq -\beta\zeta - \beta^2 q \ ; \ \zeta(t_0) = -\beta q(t_0). \tag{M.1}$$

Furthermore, the filter signal $Q_f(t)$ is defined as follows

$$Q_f \triangleq \zeta + \beta q. \tag{M.2}$$

After taking the time derivative of (M.2), the following expression is obtained

$$\dot{Q}_f = -\beta(\zeta + \beta q) + \beta\dot{q} \tag{M.3}$$

where (M.1) was utilized. After substituting (M.2) into (M.3), the following expression can be obtained

$$\dot{Q}_f \triangleq -\beta Q_f + \beta Q \tag{M.4}$$

which is same as (4.21). Thus, it is clear that (M.1) and (M.2) can be implemented to obtain $Q_f(t)$ without measuring $\dot{q}(t)$.

Appendix N

Proof of Theorem 6

Proof. To facilitate the proof, a nonnegative Lyapunov function $V_e(t) \in \mathbb{R}$ is defined as follows

$$V_e \triangleq \frac{1}{2}\tilde{\theta}_e^T \Gamma^{-1} \tilde{\theta}_e. \tag{N.1}$$

Taking the time derivative of (N.1) results in the following expression

$$\dot{V}_e = -\tilde{\theta}_e^T \Gamma^{-1} \dot{\hat{\theta}}_e + \frac{1}{2}\tilde{\theta}_e^T \dot{\Gamma}^{-1} \tilde{\theta}_e \tag{N.2}$$

where the time derivative of (4.28) was utilized. After substituting (4.30) and (4.31) into (N.2), the following expression is obtained

$$\dot{V}_e = -\varepsilon^2 + \frac{1}{2}\varepsilon^2 \tag{N.3}$$

where (4.29) was utilized. The expression given in (N.3) can be further simplied as follows

$$\dot{V}_e = -\frac{1}{2}\varepsilon^2. \tag{N.4}$$

After integrating (N.4), the following expression can be obtained

$$\frac{1}{2}\int_{t_0}^{\infty} \varepsilon^2(\tau) d\tau = V_e(t_0) - V_e(\infty). \tag{N.5}$$

From (N.1) and (N.4), it can be concluded that $V_e(t) \in \mathcal{L}_\infty$; thus, $\tilde{\theta}_e(t) \in \mathcal{L}_\infty$. From (N.5), it is clear that $\varepsilon(t) \in \mathcal{L}_2 \cap \mathcal{L}_\infty$. Since $\tilde{\theta}_e(t) \in \mathcal{L}_\infty$, from (4.28), it follows that $\hat{\theta}_e(t) \in \mathcal{L}_\infty$. Since $q(t), p(t), u(t) \in \mathcal{L}_\infty$ (see Appendix O, from (4.18), it follows that $W_e(t) \in \mathcal{L}_\infty$, and from (4.17), it follows that $Q(t) \in \mathcal{L}_\infty$. Since $Q(t), W_e(t) \in \mathcal{L}_\infty$, from Remark 2, it follows that $Q_f(t), \dot{Q}_f(t), W_f(t), \dot{W}_f(t) \in \mathcal{L}_\infty$. Since $W_f(t), \varepsilon(t) \in \mathcal{L}_\infty$, and from Remark 3, $\Gamma(t) \in \mathcal{L}_\infty$, therefore from (4.30), it can be concluded that $\dot{\hat{\theta}}_e(t) \in \mathcal{L}_\infty$; thus, the time derivative of (4.28) can be utilized to show that $\dot{\tilde{\theta}}_e(t) \in \mathcal{L}_\infty$. Since $\dot{W}_f(t), \dot{\tilde{\theta}}_e(t) \in \mathcal{L}_\infty$, the time derivative of (4.29) can be used to show that $\dot{\varepsilon}(t) \in \mathcal{L}_\infty$. Since $\varepsilon(t) \in \mathcal{L}_2 \cap \mathcal{L}_\infty$ and $\dot{\varepsilon}(t) \in \mathcal{L}_\infty$, from Barbalat's

Lemma [49], it can be concluded that $\varepsilon(t) \to 0$ as $t \to \infty$; thus, $\|W_f(t)\tilde{\theta}_e(t)\| \to 0$ as $t \to \infty$. Upon the satisfaction of the PE condition [49] given in (4.47), it can be further concluded that $\|\tilde{\theta}_e(t)\| \to 0$ as $t \to \infty$.

Appendix O

Proof of Theorem 7

Proof. To facilitate the proof, a nonnegative Lyapunov function $V_a(t) \in \mathbb{R}$ is defined as follows

$$V_a \triangleq \frac{1}{2} A e_a^2 + \frac{1}{2} \gamma_a^{-1} \tilde{\theta}_a^T \tilde{\theta}_a \tag{O.1}$$

where $\tilde{\theta}_a(t) \in \mathbb{R}^3$ is defined as follows

$$\tilde{\theta}_a \triangleq \theta - \hat{\theta}_a. \tag{O.2}$$

After taking the time derivative of (O.1), the following expression is obtained

$$\dot{V}_a = A \dot{e}_a e_a + \gamma_a^{-1} \tilde{\theta}_a^T \dot{\tilde{\theta}}_a \ . \tag{O.3}$$

Substituting (4.40) into (O.3) results in the following expression

$$\dot{V}_a = (W_a \theta_a - uq) e_a - \gamma_a^{-1} \tilde{\theta}_a^T \dot{\hat{\theta}}_a \tag{O.4}$$

where the time derivative of (O.2) was utilized. After substituting (4.43) and (4.44) into (O.4), the following expression can be obtained

$$\dot{V}_a = (W_a \tilde{\theta}_a - k_a e_a) e_a - \gamma_a^{-1} \tilde{\theta}_a^T \left(\gamma_a W_a^T e_a \right) \tag{O.5}$$

where (O.2) was utilized. The expression given in (O.5) can be further simplified as follows

$$\dot{V}_a = -k_a e_a^2. \tag{O.6}$$

After integrating (O.6), the following expression can be obtained

$$k_a \int_{t_0}^{\infty} e_a^2(\tau) d\tau = V_a(t_0) - V_a(\infty). \tag{O.7}$$

From (O.1) and (O.6), it can be concluded that $V_a(t) \in \mathcal{L}_\infty$; hence, $e_a(t), \tilde{\theta}_a(t) \in \mathcal{L}_\infty$. From (O.7), it is clear that $e_a(t) \in \mathcal{L}_2$. Since $q_d(t)$ is designed to be bounded, from (4.37), $q(t) \in \mathcal{L}_\infty$; thus, from Remark 1, $p(t) \in \mathcal{L}_\infty$. The fact that θ_a is a

constant vector and $\tilde{\theta}_a(t) \in \mathcal{L}_\infty$, from (O.2), it follows that $\hat{\theta}_a(t) \in \mathcal{L}_\infty$. Since $p(t), q(t), \dot{q}_d(t) \in \mathcal{L}_\infty$, it is clear from (4.35) and (4.41) that $W_a(t) \in \mathcal{L}_\infty$; thus, from (4.43), it can be concluded that $u(t) \in \mathcal{L}_\infty$. Further, from (4.44), it is clear that $\dot{\hat{\theta}}_a\ (t) \in \mathcal{L}_\infty$. From (4.40), it follows that $\dot{e}_a(t) \in \mathcal{L}_\infty$. Since $e_a(t) \in \mathcal{L}_2 \cap \mathcal{L}_\infty$, and from (4.40), $\dot{e}_a(t) \in \mathcal{L}_\infty$, from Barbalat's Lemma [49], it can be concluded that $e_a(t) \to 0$ as $t \to \infty$.

Appendix P

Extension of the Tumor Model with Pharmacokinetics and Pharmacodynamics

Pharmacokinetic (PK) equations describe the drug concentration in the body plasma and pharmacodynamic (PD) equations model the effectiveness of the drugs [69].

System Model

Similar to [69], the modified system model can be given as follows

$$\dot{p} = \alpha p\left(1-\frac{p}{q}\right) \tag{P.1}$$

$$\dot{q} = bq - dp^{2/3}q - Gscq \tag{P.2}$$

$$\dot{c} = -mc + hu \; ; \; c(t_0) = 0. \tag{P.3}$$

The drug dose $u(t)$ and concentration $c(t) \in \mathbb{R}$ of the inhibitors are linked by a first-order, linear, ordinary differential equation given in (P.3) where $m, h \in \mathbb{R}$ are constant parameters. The effect of the drug is proportional to the concentration of the inhibitors, given as effect $= sc$ where $s \in [0, 1]$.

In order to minimize the tumor volume $p(t)$ with an optimum drug dose $u(t)$, we modify the estimate of the performance index given in (4.15) as follows

$$\hat{J} \triangleq p + \left(\frac{\hat{S}c}{\hat{d}}\right)^{3/2} \tag{P.4}$$

where $\hat{S}(t) \in \mathbb{R}$ is the estimate of the combined term Gs. The control objective remains the same as described in Chapter 4 and given in (4.16).

Parameter Estimation

Similar to Chapter 4, we design an estimator based on least-squares estimation technique to identify the unknown parameters b, d, and S. To this end, the expression given in (P.2) is parameterized as follows

$$Q_b = W_b\theta_b \tag{P.5}$$

where $Q_b(t)$ denotes $\dot{q}(t)$, $W_b(t) \triangleq \begin{bmatrix} q & -p^{2/3}q & -cq \end{bmatrix} \in \mathbb{R}^{1\times 3}$ is a measurable regression vector, and $\theta_b \triangleq \begin{bmatrix} b & d & S \end{bmatrix}^T \in \mathbb{R}^3$ is a vector of unknown parameters. An analysis similar to that given in Chapter 4 can be followed to obtain a similar least-squares update law to identify θ_b. The update law is given as follows

$$\dot{\hat{\theta}}_b = \Gamma_b W_{bf}^T \varepsilon_b \tag{P.6}$$

where $\Gamma_b(t) \in \mathbb{R}^{3\times 3}$ is the least-squares estimation gain matrix, $W_{bf}(t) \in \mathbb{R}^{1\times 3}$ is the filtered regression vector, and $\varepsilon_b(t)$ is the prediction error.

Development of Adaptive Backstepping Control Law

The control input $u(t)$ appears only in the last equation of the system model described by (P.1)-(P.3); therefore, an additional level of control is added using an adaptive backstepping technique to make $q(t)$ track an optimum desired trajectory $q_d(t)$ (and thus, $p(t)$ to track an optimum desired trajectory) without any knowledge about the model parameters.

To facilitate the development, we consider $c(t)$ as the virtual control input, and define two error signals $e_1(t), e_2(t) \in \mathbb{R}$ as follows

$$e_1 \triangleq q - q_d \tag{P.7}$$

$$e_2 \triangleq c - c_d \tag{P.8}$$

where $c_d(t) \in \mathbb{R}$ is a subsequently designed desired trajectory for $c(t)$. After dividing both sides of (P.2) by Gs, the parameterized form of the resulting expression can be written as follows

$$A_1 \dot{q} = W_1 \theta_1 - cq \tag{P.9}$$

where $A_1 \triangleq (Gs)^{-1}$, $W_1 \triangleq \begin{bmatrix} q & -p^{2/3}q \end{bmatrix} \in \mathbb{R}^{1\times 2}$ is a measurable regression vector, and $\theta_1 \triangleq \begin{bmatrix} bA_1 & dA_1 \end{bmatrix}^T \in \mathbb{R}^2$ is an unknown vector. After substituting (P.8) into (P.9), the following expression can be obtained

$$A_1 \dot{q} = W_1 \theta_1 - e_2 q - c_d q. \tag{P.10}$$

After taking the time derivative of (P.7), and multiplying both the sides of the resulting expression by A_1, the following expression can be written

$$A_1 \dot{e}_1 = W_2 \theta_2 - e_2 q - c_d q \tag{P.11}$$

where (P.10) was utilized. In (P.11), $W_2(t) \in \mathbb{R}^{1\times 3}$ is a measurable regression vector, and $\theta_2 \in \mathbb{R}^3$ is a vector of unknown parameters, defined as follows

$$W_2 \triangleq \begin{bmatrix} W_1 & -\dot{q}_d \end{bmatrix} \tag{P.12}$$

and

$$\theta_2 \triangleq \begin{bmatrix} \theta_1^T & A_1 \end{bmatrix}^T. \tag{P.13}$$

Based on the subsequent stability analysis, $c_d(t)$ is designed as follows

$$c_d \triangleq \frac{1}{q}\left(W_2 \hat{\theta}_2 + k_1 e_1\right) \tag{P.14}$$

where $\hat{\theta}_2(t) \in \mathbb{R}^3$ is an estimate vector of θ_2, and $k_1 \in \mathbb{R}$ is a positive constant. Following the same procedure, *i.e.*, dividing both the sides of (P.3) by h and then substituting the results into the time derivative of (P.8), the following expression can be written

$$A_2 \dot{e}_2 = W_3 \theta_3 + u \tag{P.15}$$

where $A_2 \triangleq h^{-1} \in \mathbb{R}$, $W_3(t) \in \mathbb{R}^{1\times 2}$ is a measurable regression vector, and $\theta_3 \in \mathbb{R}^2$ is a vector of unknown parameters, defined as follows

$$W_3 \triangleq \begin{bmatrix} -c & -\dot{c}_d \end{bmatrix} \tag{P.16}$$

and

$$\theta_3 \triangleq \begin{bmatrix} mA_2 & A_2 \end{bmatrix}^T. \tag{P.17}$$

Based on the subsequent stability analysis, the control law $u(t)$ is designed as follows

$$u \triangleq -W_3 \hat{\theta}_3 - k_2 e_2 + e_1 q, \tag{P.18}$$

where $\hat{\theta}_3(t) \in \mathbb{R}^2$ is an estimate vector of θ_3, and $k_2 \in \mathbb{R}$ is a positive constant. The update laws $\dot{\hat{\theta}}_2(t) \in \mathbb{R}^3$ and $\dot{\hat{\theta}}_3 \in \mathbb{R}^2$ are designed as follows

$$\dot{\hat{\theta}}_2 \triangleq \gamma_2 W_2^T e_1 \ , \ \dot{\hat{\theta}}_3 \triangleq \gamma_3 W_3^T e_2 \tag{P.19}$$

where $\gamma_2, \gamma_3 \in \mathbb{R}$ are positive constants.

Stability Analysis

Theorem 11 *The control laws given in (P.14) and (P.18) along with the update laws given in (P.19) ensure that* $e_1(t), e_2(t) \to 0$ *as* $t \to \infty$.

Proof. To facilitate the proof, a nonnegative Lyapunov function $V_b(t) \in \mathbb{R}$ is defined as follows

$$V_b \triangleq \frac{1}{2} A_1 e_1^2 + \frac{1}{2} A_2 e_2^2 + \frac{1}{2} \gamma_2^{-1} \tilde{\theta}_2^T \tilde{\theta}_2 + \frac{1}{2} \gamma_3^{-1} \tilde{\theta}_3^T \tilde{\theta}_3. \tag{P.20}$$

In (P.20), $\tilde{\theta}_2(t) \in \mathbb{R}^3, \tilde{\theta}_3(t) \in \mathbb{R}^2$ are defined as follows

$$\tilde{\theta}_2 \triangleq \theta_2 - \hat{\theta}_2, \ \tilde{\theta}_3 \triangleq \theta_3 - \hat{\theta}_3. \tag{P.21}$$

Taking the time derivative of (P.20), yields the following expression

$$\dot{V}_b = A_1 \dot{e}_1 e_1 + A_2 \dot{e}_2 e_2 - \gamma_2^{-1} \tilde{\theta}_2^T \ \dot{\hat{\theta}}_2 - \gamma_3^{-1} \tilde{\theta}_3^T \ \dot{\hat{\theta}}_3 \tag{P.22}$$

where the time derivatives of $\tilde{\theta}_2(t)$ and $\tilde{\theta}_3(t)$ given in (P.21) were utilized. After substituting (P.11), (P.15), and (P.19) into (P.22), the following expression is obtained

$$\begin{aligned} \dot{V}_b &= (W_2 \theta_2 - e_2 q - c_d q) e_1 + (W_3 \theta_3 + u) e_2 \\ &\quad - \gamma_2^{-1} \tilde{\theta}_2^T \left(\gamma_2 W_2^T e_1 \right) - \gamma_3^{-1} \tilde{\theta}_3^T \left(\gamma_3 W_3^T e_2 \right). \end{aligned} \tag{P.23}$$

Substituting (P.14) and (P.18) into (P.23) results in the following expression

$$\begin{aligned} \dot{V}_b &= (W_2 \tilde{\theta}_2 - e_2 q - k_1 e_1) e_1 - \tilde{\theta}_2^T W_2^T e_1 \\ &\quad + (W_3 \tilde{\theta}_3 + e_1 q - k_2 e_2) e_2 - \tilde{\theta}_3^T W_3^T e_2 \end{aligned} \tag{P.24}$$

where (P.21) was utilized. The expression given in (P.24) can be further simplified to obtain

$$\dot{V}_b = -k_1 e_1^2 - k_2 e_2^2. \tag{P.25}$$

From (P.25), the following inequalities can be written

$$\dot{V}_b \leq -k_1 e_1^2, \tag{P.26}$$

$$\dot{V}_b \leq -k_2 e_2^2. \tag{P.27}$$

After integrating (P.26) and (P.27), the following inequalities can be obtained

$$k_1 \int_{t_0}^{\infty} e_1^2(\tau) d\tau \leq V_b(t_0) - V_b(\infty), \tag{P.28}$$

$$k_2 \int_{t_0}^{\infty} e_2^2(\tau) d\tau \leq V_b(t_0) - V_b(\infty). \tag{P.29}$$

From (P.20) and (P.25), it can be concluded that $V_b(t) \in \mathcal{L}_\infty$; hence, $e_1(t), e_2(t), \tilde{\theta}_2(t)$, $\tilde{\theta}_3(t) \in \mathcal{L}_\infty$. From (P.28) and (P.29), it is clear that $e_1(t), e_2(t) \in \mathcal{L}_2$. Since $q_d(t)$ is designed to be bounded, from (P.7), $q(t) \in \mathcal{L}_\infty$; thus, from Remark 1, $p(t) \in \mathcal{L}_\infty$. The fact that θ_2 and θ_3 are constant vectors and $\tilde{\theta}_2(t), \tilde{\theta}_3(t) \in \mathcal{L}_\infty$, from (P.21), it follows that $\hat{\theta}_2(t), \hat{\theta}_3(t) \in \mathcal{L}_\infty$. Since $p(t), q(t), \dot{q}_d(t) \in \mathcal{L}_\infty$, it is clear from (P.12) that $W_2(t) \in \mathcal{L}_\infty$. Further, since $\hat{\theta}_2(t) \in \mathcal{L}_\infty$, therefore from (P.14), $c_d(t) \in \mathcal{L}_\infty$; thus, from (P.8), $c(t) \in \mathcal{L}_\infty$. From (P.19), it follows that $\dot{\hat{\theta}}_2(t) \in \mathcal{L}_\infty$. Since $c_d(t)$ is a function of bounded and continuous signals, after taking its time derivative, it follows that $\dot{c}_d(t) \in \mathcal{L}_\infty$; therefore, from (P.16), $W_3(t) \in \mathcal{L}_\infty$. Now it follows from (P.19) that $\dot{\hat{\theta}}_3(t) \in \mathcal{L}_\infty$. From (P.18), it follows that $u(t) \in \mathcal{L}_\infty$. Since $e_1(t), e_1(t) \in \mathcal{L}_2 \cap \mathcal{L}_\infty$, and from (P.11) and (P.15) $\dot{e}_1(t), \dot{e}_2(t) \in \mathcal{L}_\infty$, from Barbalat's Lemma [49], it can be concluded that $e_1(t), e_2(t) \to 0$ as $t \to \infty$.

Appendix Q

Estimation of $q(t)$ in the Tumor Dynamic Model

It may be difficult to measure the carrying capacity of the endothelial cells $q(t)$ directly; therefore, an estimate of $q(t)$ may be desired. In order to estimate $q(t)$, we assume $p(t)$ is measurable and the constant parameter α given in (4.1) is known.

To facilitate the development, the expression given in (4.1) is rewritten as follows

$$\dot{p} = \alpha p + f(p, q) \tag{Q.1}$$

where $f(\cdot) \triangleq -\alpha p^2/q \in \mathbb{R}$ represents a function of the unmeasurable function of $p(t)$ and $q(t)$. The estimate of (Q.1) is defined as follows

$$\dot{\hat{p}} \triangleq \alpha p + \hat{f}(\cdot) \tag{Q.2}$$

where $\hat{f}(\cdot) \in \mathbb{R}$ is the subsequently designed estimate of $f(\cdot)$. An estimation error $\tilde{p}(t) \in \mathbb{R}$ is defined as follows

$$\tilde{p} \triangleq p - \hat{p}. \tag{Q.3}$$

After taking the time derivative of (Q.3), and then substituting (Q.1) and (Q.2) into the resulting expression, the following expression can be obtained

$$\dot{\tilde{p}}\,(t) = f(\cdot) - \hat{f}(\cdot). \tag{Q.4}$$

A proportional-integral-like nonlinear observer $\hat{f}(\cdot)$ can be designed as follows

$$\begin{aligned} \hat{f} \;\triangleq\; & (k_s + 1)\left(\tilde{p}(t) - \tilde{p}(t_0) + \int_{t_0}^{t} \tilde{p}(\tau)d\tau\right) \\ & + \beta \int_{t_0}^{t} \operatorname{sgn}(\tilde{p}(\tau))d\tau \end{aligned} \tag{Q.5}$$

where $k_s, \beta \in \mathbb{R}$ are positive constants and $\operatorname{sgn}(\cdot)$ denotes the standard signum function. The estimator given in (Q.5) ensures that $\hat{f}(\cdot) \to f(\cdot)$ as $t \to \infty$. The reader is referred to [94] for a detailed analysis of the estimator. From the estimate $\hat{f}(\cdot)$, the estimate of $q(t)$ can be easily obtained as $\hat{q} = -\alpha p^2/\hat{f}(\cdot)$.

BIBLIOGRAPHY

[1] X. Chen and H. Kano, "A new state observer for perspective systems," *IEEE Trans. Automat. Contr.*, vol. 47, no. 4, pp. 658–663, Apr. 2002.

[2] A. D. Luca, G. Oriolo, and P. R. Giordano, "Feature depth observation for image-based visual servoing: Theory and experiments," *Int. Journal of Robotics Research*, vol. 27, no. 10, p. 10931116, 2008.

[3] T. Fukao, K. Fujitani, and T. Kanade, "An autonomous blimp for a surveillance system," in *Proc. IEEE/RSJ Int. Conf. Intell. Robots Syst.*, Las Vegas, NV, 2003, pp. 1820–1825.

[4] T. Kanade, O. Amidi, and Q. Ke, "Real-time and 3d vision for autonomous small and micro air vehicles," in *Proc. IEEE Int. Conf. Decision and Control*, Dec. 2004, pp. 1655–1662.

[5] J. D. Redding, T. W. McLain, R. W. Beard, and C. N. Taylor, "Vision-based target localization from a fixed-wing miniature air vehicle," in *Proc. American Control Conf.*, Minneapolis, MN, Jun. 2006, pp. 2862–2867.

[6] V. N. Dobrokhodov, I. I. Kaminer, K. D. Jones, and R. Ghabcheloo, "Vision based tracking and motion estimation for moving targets using small uavs," in *Proc. American Control Conf.*, Minneapolis, MN, Jul. 2006, pp. 1428–1433.

[7] J. H. Kim and S. Sukkarieh, "Airborne simultaneous localisation and map building," in *Proc. IEEE Int. Conf. Robot. Autom.*, Taipei, Taiwan, 2003, pp. 406–411.

[8] I. K. Jung and S. Lacroix, "High resolution terrain mapping using low altitude aerial stereo imagery," in *Proc. IEEE Int. Conf. Computer Vision*, Nice, France, 2003, pp. 1820–1825.

[9] I. Miyagawa and K. Arakawa, "Motion and shape recovery based on iterative stabilization for modest deviation from planar motion," *IEEE Trans. Pattern Anal. Machine Intell.*, vol. 28, no. 7, pp. 1176–1181, Jul. 2006.

[10] L. Matthies, T. Kanade, and R. Szeliski, "Kalman filter-based algorithms for estimating depth from image sequences," *Int. J. of Computer Vision*, vol. 3, no. 3, pp. 209–238, 1989.

[11] B. Sridhar, R. Soursa, and B. Hussein, "Passive range estimation fro rotorcraft low-attitude flight," *Int. Journal of Machine Vision Application*, vol. 6, pp. 10–24, 1993.

[12] A. Chiuso, P. Favaro, H. Jin, and S. Soatto, "Structure from motion casually integrated over time," *IEEE Trans. Pattern Anal. Machine Intell.*, vol. 24, no. 4, pp. 523–535, Apr. 2002.

[13] H. Durrant-Whyte and T. Bailey, "Simultaneous localization and mapping (slam): Part ii," *IEEE Robot. and Automat. Mag.*, vol. 13, no. 3, pp. 108–117, Sep. 2006.

[14] A. J. Davison, I. D. Reid, N. D. Molton, and O. Stasse, "Monoslam: Real-time single camera slam," *IEEE Trans. Pattern Anal. Machine Intell.*, vol. 29, no. 6, pp. 1052–1067, Jun. 2007.

[15] S. J. Julier and J. K. Uhlmann, "A counter example to the theory of simultaneous localization and map building," in *Proc. IEEE Int. Conf. Robot. Autom.*, Seoul, Korea, 2001, pp. 4238–4243.

[16] K. Reif, F. Sonnemann, and R. Unbehauen, "An EKF-based nonlinear observer with a prescribed degree of stability," *Automatica*, vol. 34, no. 9, pp. 1119–1123, Sep. 1998.

[17] M. Jankovic and B. K. Ghosh, "Visually guided ranging from observations of points, lines and curves via an identifier based nonlinear observer," *Systems and Control Letters*, vol. 25, pp. 63–73, 1995.

[18] X. Chen and H. Kano, "State observer for a class of nonlinear systems and its application to machine vision," *IEEE Trans. Automat. Contr.*, vol. 49, no. 11, pp. 2085–2091, 2004.

[19] W. E. Dixon, Y. Fang, D. M. Dawson, and T. J. Flynn, "Range identification for perspective vision systems," *IEEE Trans. Automat. Contr.*, vol. 48, no. 12, pp. 2232–2238, 2003.

[20] L. Ma, Y. Chen, and K. L. Moore, "Range identification for perspective dynamic system with single homogeneous observation," in *Proc. IEEE Int. Conf. Robot. Autom.*, New Orleans, LA, Apr. 2004, pp. 5207–5211.

[21] X. Hu and T. Ersson, "Active state estimation of nonlinear systems," *Automatica*, vol. 40, pp. 2075–2082, 2004.

[22] R. Abdursal, H. Inaba, and B. Ghosh, "Nonlinear observers for perspective time-invariant linear systems," *Automatica*, vol. 40, no. 3, pp. 481–490, 2004.

[23] D. Karagiannis and A. Astolfi, "A new solution to the problem of range identification in perspective vision systems," *IEEE Trans. Automat. Contr.*, vol. 50, no. 12, pp. 2074–2077, 2005.

[24] R. Y. Tsai and T. S. Huang, "Estimating three-dimensional motion parameters of a rigid planar patch," *IEEE Trans. on Acoustic, Speech, and Signal Processing*, vol. ASSP-29, no. 6, pp. 1147–1152, 1981.

[25] S. Gupta, D. Aiken, G. Hu, and W. E. Dixon, "Lyapunov-based range and motion identification for a nonaffine perspective dynamic system," in *Proc. American Control Conf.*, Minneapolis, MN, Jun. 2006, pp. 4471–4476.

[26] O. Dahl, F. Nyberg, and A. Heyden, "Nonlinear and adaptive observers for perspective dynamic systems," in *Proc. American Control Conf.*, New York, NY, Jul. 2007, pp. 1966–971.

[27] D. Braganza, D. M. Dawson, and T. Hughes, "Euclidean position estimation of static features using a moving camera with known velocities," in *Proc. IEEE Int. Conf. Decision and Control*, New Orleans, LA, Dec. 2007.

[28] ——, "Euclidean position estimation of static features using a moving camera with known velocities," Clemson University CRB, Tech. Rep. CU/CRB/3/9/07/2, Mar. 2007. [Online]. Available: http://www.ces.clemson.edu/ece/crb/publictn/tr.htm

[29] O. Faugeras, *Three-Dimensional Computer Vision*. Cambridge, MA: MIT Press, 1993.

[30] E. Malis and F. Chaumette, "2 1/2 D visual servoing with respect to unknown objects through a new estimation scheme of camera displacement," *Int. Journal of Computer Vision*, vol. 37, no. 1, pp. 79–97, 2000.

[31] M. Krstic, I. Kanellakopoulos, and P. Kokotovic, *Nonlinear and Adaptive Control Design*. New York, NY: John Wiley and Sons, 1995.

[32] M. de Queiroz, D. Dawson, S. Nagarkatti, and F. Zhang, *Lyapunov-Based Control of Mechanical Systems*. Boston, MA: Birkhauser, 1999.

[33] J. J. E. Slotine and W. Li, *Applied Nonlinear Control*. Englewood Cliffs, NJ: Prentice Hall, 1991.

[34] C. E. Smith and N. P. Papanikolopoulos, "Computation of shape through controlled active exploration," in *Proc. IEEE Int. Conf. Robot. Autom.*, San Diego, CA, May 1994, pp. 2516–2521.

[35] B. D. Lucas and T. Kanade, "An iterative image registration technique with an application to stereo vision," in *Proc. Int. Joint Conf. Artificial Intell.*, Apr. 1981, pp. 674–679.

[36] S. Birchfield, "KLT: an implementation of the Kanade-Lucas-Tomasi feature tracker," Tech. Rep. [Online]. Available: http://www.ces.clemson.edu/~stb/klt

[37] J. Shi and C. Tomasi, "Good features to track," in *Proc. IEEE Conf. Computer Vision and Pattern Recognition*, Seattle, Jun. 1994, pp. 593–600.

[38] J. Bouguet, "Camera calibration toolbox for matlab," Tech. Rep. [Online]. Available: http://www.vision.caltech.edu/bouguetj

[39] D. Karagiannis and A. Astolfi, "A new solution to the problem of range identification in perspective vision systems," *IEEE Trans. Automat. Contr.*, vol. 50, no. 12, pp. 2074–2077, 2005.

[40] A. De Luca, G. Oriolo, and P. R. Giordano, "On-line estimation of feature depth for image-based visual servoing schemes," in *Proc. IEEE Int. Conf. Robot. Autom.*, Roma, Italy, Apr. 2007, pp. 2823–2828.

[41] N. Nath, D. Braganza, and D. M. Dawson, "Position based structure from motion using a moving calibrated camera," in *Proc. American Control Conf.*, Seattle, WA, Jun. 2008, pp. 1764–1769.

[42] N. Nath, D. Braganza, D. M. Dawson, and T. Burg, "Range identification for perspective vision systems: a position based approach," Clemson University CRB, Tech. Rep. CU/CRB/05/22/09/1, May 2009. [Online]. Available: http://www.ces.clemson.edu/ece/crb/publictn/tr.htm

[43] R. I. Hartley and A. Zisserman, *Multiple View Geometry in Computer Vision*. Cambridge, U.K.: Cambridge University Press, 2000.

[44] R. I. Hartley, *Euclidean reconstruction from uncalibrated views, Applications of Invariance in Computer Vision - Lecture Notes in Computer Science*. Berlin, Germany: Springer, 1994, vol. 825, pp. 235-256.

[45] Y. F. Li and R. S. Lu, "Uncalibrated Euclidean 3-D reconstruction using an active vision system," *IEEE Trans. Robot. Autom.*, vol. 20, no. 1, pp. 15–25, 2004.

[46] A. Kapadia, D. Braganza, D. M. Dawson, and M. L. McIntyre, "Adaptive camera calibration with measurable position of fixed features," in *Proc. American Control Conf.*, Seattle, WA, Jun. 2008, pp. 3869–3874.

[47] S. Nicosia and P. Tomei, "Robot control by using only joint position measurements," *Trans. Automat. Contr.*, vol. 35, no. 9, pp. 1058–1061, 1990.

[48] E. Tatlicioglu, D. M. Dawson, and B. Xian, "Adaptive visual servo regulation control for camera-in-hand configuration with a fixed-camera extension," Clemson University CRB, Tech. Rep. CU/CRB/3/9/07/1, Mar. 2007. [Online]. Available: http://www.ces.clemson.edu/ece/crb/publictn/tr.htm

[49] P. A. Ioannou and J. Sun, *Robust Adaptive Control*. Upper Saddle River, NJ: Prentice Hall, 1996.

[50] S. Baker and S. Nayar, "A theory of single-viewpoint catadioptric image formation," *Int. J. of Computer Vision*, vol. 35, no. 2, pp. 175–196, 1999.

[51] G. Hu, D. Aiken, S. Gupta, and W. Dixon, "Lyapunov-based range identification for paracatadioptric systems," *IEEE Trans. Automat. Contr.*, vol. 53, no. 7, pp. 1775–1781, 2008.

[52] R. Orghidan, E. M. Mouaddib, and J. Salvi, "Omnidirectional depth computation from a single image," in *Proc. IEEE Int. Conf. Robot. Autom.*, Barcelona, Spain, Apr. 2005, pp. 1222–1227.

[53] H. Kano, B. K. Ghosh, and H. Kanai, "Single camera based motion and shape estimation using extended Kalman filtering," *Math. Comput. Model*, vol. 34, no. 5, pp. 511–525, 2001.

[54] L. Ma, Y. Chen, and K. L. Moore, "Range identification for perspective dynamic systems with 3D imaging surfaces," in *Proc. American Control Conf.*, Portland, OR, Jun. 2005, pp. 3671–3675.

[55] A. M. Annaswamy, F. P. Skantze, and A. P. Loh, "Adaptive control of continuous time systems with convex/concave parameterization," *Automatica*, vol. 34, no. 1, pp. 33–49, 1998.

[56] C. Geyer and K. Daniilidis, "A unifying theory for central panoramic systems and practical implementations," in *Proc. European Conf. Computer Vision*, Dublin, Ireland, Jun. 2000, pp. 445–461.

[57] ——, "Paracatadioptric camera calibration," *IEEE Trans. Pattern Anal. Machine Intell.*, vol. 24, no. 5, pp. 687–695, 2002.

[58] J. P. Barreto and H. Araujo, "Geometric properties of central catadioptric line images and their application in calibration," *IEEE Trans. Pattern Anal. Machine Intell.*, vol. 27, no. 8, pp. 1327–1333, 2005.

[59] S. Boyd and L. Vandenberghe, *Convex Optimization*. Cambridge, UK: Cambridge University Press, 2004.

[60] D. M. Y. Sommerville, *An introduction to the Geometry of n-dimensions*. New York, U.S.A.: Dover, 1958.

[61] J. D. Boskovic, "Some remarks on adaptive neuro-fuzzy systems," *Int. J. Adaptive Control Signal Processing*, vol. 10, pp. 79–83, 1996.

[62] V. Fomin, A. Fradkov, and V. Yakubovich, *Adaptive Control of Dynamical Systems*. Moscow, Russia: Nauka, 1981.

[63] R. Ortega, "Adaptive control of a class of nonlinearly parameterized plants," *IEEE Trans. Automat. Contr.*, vol. 43, no. 7, pp. 930–934, 1998.

[64] C. Cao, A. M. Annaswamy, and A. Kojic, "Parameter convergence in nonlinearly parameterized systems," *IEEE Trans. Automat. Contr.*, vol. 48, no. 3, pp. 397–412, 2003.

[65] U. Ledzewicz and H. Schättler, "Anti-angiogenic therapy in cancer treatment as an optimal control problem," *SIAM J. Contr. Optim.*, vol. 46, no. 3, pp. 1052–1079, 2007.

[66] M. Klagsburn and S. Soker, "VEGF/VPF: the angiogenesis factor found?" *Curr. Bio.*, vol. 3, no. 10, pp. 699–702, 1993.

[67] J. Folkman, "Angiogenesis inhibitors generated by tumors," *Mol. Med.*, vol. 1, no. 2, pp. 120–122, 1995.

[68] ——, "Antiangiogenesis: new concept for therapy of solid tumors," *Ann. Surg.*, vol. 175, no. 3, pp. 409–416, 1972.

[69] U. Ledzewicz, Y. Liu, and H. Schättler, "The effect of pharmacokinetics on optimal protocols for a mathematical model of tumor anti-angiogenic therapy," in *Proc. American Control Conf.*, St. Louis, MO, Jun. 2009, pp. 1060–1065.

[70] S. Davis and G. D. Yancopoulos, "The angiopoietins: Yin and Yang in angiogenesis," *Curr. Top. Microbiol. Immunol.*, vol. 237, pp. 173 – 185, 1999.

[71] T. Boehm, J. Folkman, T. Browder, and M. O'Reilly, "Antiangiogenic therapy of experimental cancer does not induce acquired drug resistance," *Nature*, vol. 390, pp. 404–407, 1997.

[72] G. Fürstenberger, R. von Moos, R. Lucas, B. Thürlimann, H-J. Senn, J. Hamacher, and E-M. Boneberg, "Circulating endothelial cells and angiogenic serum factors during neoadjuvant chemotherapy of primary breast cancer," *Br. J. Cancer*, vol. 94, no. 4, pp. 524–531, 2006.

[73] R. S. Kerbel, "A cancer therapy resistant to resistance," *Nature*, vol. 390, pp. 335–336, 1997.

[74] A. Anderson and M. Chaplain, "Continuous and discrete mathematical models of tumor induced angiogenesis," *Bull. Math. Bio.*, vol. 60, no. 5, pp. 857–859, 1998.

[75] L. Arakelyan, V. Vainstain, and Z. Agur, "A computer algorithm describing the process of vessel formation and maturation and its use for predicting the effects of anti-angiogenic and anti- maturation therapy on vascular tumor growth," *Angiogenesis*, vol. 5, no. 3, pp. 203–214, 2002.

[76] S. Ramanujan, G. C. Koenig, T. P. Padera, B. R. Stoll, and R. K. Jain, "Local imbalance of prangiogenic and antiangiogenic factors: a potential mechanism of focal necrosis and dormancy in tumors," *Can. Res.*, vol. 60, pp. 1442–1448, 2000.

[77] E. De Angelis and L. Preziosi, "Advection-diffusion models for solid tumour evolution in vivo and related free boundary problem," *Mathematical Models and Methods in Applied Sciences*, vol. 10, no. 3, pp. 379–407, 2000.

[78] J. L. Jackson, "Vascular tumor growth and treatment: consequences of polyclonality, competition and dynamic vascular support," *J. Math. Bio.*, vol. 44, no. 3, pp. 201–226, 2002.

[79] C. J. W. Breward, H. M. Byrne, and C. E. Lewis, "A multiphase model describing vascular tumour growth," *Bull. Math. Bio.*, vol. 65, no. 4, pp. 609–640, 2003.

[80] U. Ledzewicz, H. Schättler, and A. d'Onofrio, "Optimal control for combination therapy in cancer," in *Proc. IEEE Int. Conf. Decision and Control*, Cancun, Mexico, Dec. 2008, pp. 1442–1448.

[81] P. Hahnfeldt, D. Panigrahy, J. Folkman, and L. Hlatky, "Tumor development under angiogenic signaling: a dynamical theory of tumor growth, treatment response, and postvascular dormancy," *Cancer Res.*, vol. 59, no. 19, pp. 4770–4775, 1999.

[82] A. d'Onofrio and A. Gandolfi, "Tumor eradication by antiangiogenic therapy: analysis and extensions of the model by Hahnfeldt et al. (1999)," *Math. Biosci.*, vol. 191, no. 2, pp. 159–184, 2004.

[83] A. Ergun, K. Camphausen, and L. M. Wein, "Optimal scheduling of radiotherapy and angiogenic inhibitors," *Bull. Math. Bio.*, vol. 65, no. 3, pp. 407–424, 2003.

[84] U. Ledzewicz and H. Schättler, "Optimal control for a system modelling tumor anti-angiogenesis," *ICGST Int. J. Automatic Control and Systems Engineering*, vol. 6, pp. 33–39, 2006.

[85] ——, "Minimization of the tumor volume and endothelial support for a system describing tumor anti-angiogenesis," *WSEAS Tran. Bio. Biomed.*, vol. 5, no. 2, pp. 23–33, 2008.

[86] A. Swierniak, A. d'Onofrio, and A. Gandolfi, "Control problems related to tumor angiogenesis," in *Proc. IEEE Ind. Electronics, IECON*, Paris, France, Nov. 2006, pp. 677–681.

[87] A. d'Onofrio and A. Gandolfi, "A family of models of angiogenesis and anti-angiogenesis anti-cancer treatment," *Math. Med. Bio.*, vol. 26, pp. 63–95, 2009.

[88] R. Kerbel and J. Folkman, "Clinical translation of angiogenesis inhibitors," *Nat. Rev. Can.*, vol. 2, no. 10, pp. 727–739, 2002.

[89] Y. Cao, "Tumor angiogenesis and therapy," *Biomedicine and Pharmacotherapy*, vol. 59, no. Supplement 2, pp. S340–S343, 2005.

[90] D. M. Dawson, J. Hu, and T. C. Burg, *Nonlinear Control of Electric Machinery*. New York, NY: Marcel Dekker, Inc., 1998.

[91] H. F. Grip, L. Imsland, T. A. Johansen, T. I. Fossen, J. C. Kalkkuhl, and A. Suissa, "Nonlinear vehicle side-slip estimation with friction adaptation," *Automatica*, vol. 44, no. 3, pp. 611–622, 2008.

[92] W. E. Dixon, A. Behal, D. M. Dawson, and S. Nagarkatti, *Nonlinear Control of Engineering Systems: A Lyapunov-Based Approach*. Boston, MA: Birkhauser, 2003.

[93] H. K. Khalil, *Nonlinear Systems, 3rd Edition*. New York, NY: Prentice Hall, 2002.

[94] E. Tatlicioglu, M. McIntyre, D. M. Dawson, and T. Burg, "Coordination control for haptic and teleoperator systems," Clemson University CRB, Tech. Rep. CU/CRB/2/28/06/1, Feb. 2006. [Online]. Available: http://www.ces.clemson.edu/ece/crb/publictn/tr.htm